

~~CONFIDENTIAL~~

UNCLASSIFIED

2260-1-T = RL-2045

Studies in Radar
Cross - Sections - XV
Radar Cross - Sections of
B - 47 and B - 52 Aircraft

by C. E. Schensted, J. W. Crispin,
and K. M. Siegel

Contract AF 33 - (616) - 2531
August 1954
2260-1 - T

University of Michigan
Engineering Research Institute
Willow Run Research Center
Willow Run Airport
Ypsilanti, Michigan

UNCLASSIFIED

~~CONFIDENTIAL~~

STUDIES IN RADAR CROSS-SECTIONS

- I Scattering by a Prolate Spheroid, F. V. Schultz (UMM-42, March 1950) W-33(038)-ac-14222. UNCLASSIFIED
- II The Zeros of the Associated Legendre Functions $P_n^m(\mu')$ of Non-Integral Degree, K. M. Siegel, D. M. Brown, H. E. Hunter, H. A. Alperin, and C. W. Quillen (UMM-82, April 1951) W-33(038)-ac-14222. UNCLASSIFIED
- III Scattering by a Cone, K. M. Siegel and H. A. Alperin (UMM-87, January 1952) AF-30(602)-9. UNCLASSIFIED
- IV Comparison Between Theory and Experiment of the Cross-Section of a Cone, K. M. Siegel, H. A. Alperin, J. W. Crispin, H. E. Hunter, R. E. Kleinman, W. C. Orthwein, and C. E. Schensted (UMM-92, February 1953) AF-30(602)-9. UNCLASSIFIED
- V An Examination of Bistatic Early Warning Radars, K. M. Siegel, (UMM-98, August 1952) W-33(038)-ac-14222. SECRET
- VI Cross-Sections of Corner Reflectors and Other Multiple Scatterers at Microwave Frequencies, R. R. Bonkowski, C. R. Lubitz, and C. E. Schensted (UMM-106, October 1953) AF-30(602)-9. SECRET (UNCLASSIFIED when Appendix is removed)
- VII Summary of Radar Cross-Section Studies Under Project Wizard, K. M. Siegel, J. W. Crispin, and R. E. Kleinman (UMM-108, November 1952) W-33(038)-ac-14222. SECRET
- VIII Theoretical Cross-Sections as a Function of Separation Angle Between Transmitter and Receiver at Small Wavelengths, K. M. Siegel, H. A. Alperin, R. R. Bonkowski, J. W. Crispin, A. L. Maffett, C. E. Schensted, and I. V. Schensted (UMM-115, October 1953) W-33(038)-ac-14222. UNCLASSIFIED
- IX Electromagnetic Scattering by an Oblate Spheroid, L. M. Rauch (UMM-116, October 1953) AF-30(602)-9. UNCLASSIFIED
- X The Radar Cross-Section of a Sphere, H. Weil (2144-6-T, to be published) DA-36(039)SC-52654. UNCLASSIFIED
- XI The Numerical Determination of the Radar Cross-Section of a Prolate Spheroid, K. M. Siegel, B. H. Gere, I. Marx, and F. B. Sleator (UMM-126, December 1953) W-33(038)-ac-14222. UNCLASSIFIED
- XII Summary of Radar Cross-Section Studies Under Project MIRO, K. M. Siegel, M. E. Anderson, R. R. Bonkowski, and W. C. Orthwein (UMM-127, December 1953) AF-30(602)-9. SECRET
- XIII Description of a Dynamic Measurement Program, K. M. Siegel and J. M. Wolf (UMM-128, May 1954) W-33(038)-ac-14222. CONFIDENTIAL
- XIV Cross-Sections of Ballistic Missiles, (UMM-134, to be published) AF-33(038)-ac-14222. SECRET
- XV Radar Cross-Sections of B-47 and B-52 Aircraft, C. E. Schensted, J. W. Crispin, and K. M. Siegel (2260-1-T, August 1954) AF-33(616)-2531. CONFIDENTIAL

TABLE OF CONTENTS

<u>Section</u>	<u>Title</u>	<u>Page</u>
	Preface	ii
I	Introduction	1
II	Theoretical Cross-Sections of B-47 Aircraft	3
	2.1 Method (one figure)	3
	2.2 X-Band and S-Band Cross-Sections (four figures)	6
	2.3 L-Band Cross-Sections (four figures)	11
	2.4 Cross-Sections for $\lambda = 91.4$ cm and $\lambda = 4.57$ m (eight figures)	11
III	Theoretical Cross-Sections of B-52 Aircraft	25
	3.1 Method	25
	3.2 X-Band and S-Band Cross-Sections (five figures)	25
	3.3 L-Band Cross-Sections (five figures)	31
	3.4 Cross-Sections for $\lambda = 91.4$ cm and $\lambda = 4.57$ m (twelve figures)	31
IV	Comparison Between Theory and Experiment (fifteen figures)	50
	References: Text	67
Appendix A ¹	Radar Cross-Section Computation Procedures	69
Appendix B	Replacement of B-47 and B-52 Parts by Simple Shapes	137
	References: Appendices	145
	Distribution	146

¹ When detached from the body of this report, Appendix A is UNCLASSIFIED.

PREFACE

This paper is the fifteenth in a series of reports growing out of studies of radar cross-sections at the Willow Run Research Center of the University of Michigan. The primary aims of this program are:

1. To show that radar cross-sections can be determined analytically.
2. To elaborate means for computing cross-sections of various objects of military interest.
3. To demonstrate that these theoretical cross-sections are in agreement with experimentally determined values.

Intermediate objectives are:

1. To compute the exact theoretical cross-sections of various simple bodies by solution of the appropriate boundary-value problems arising from the electromagnetic vector wave equation.
2. To examine the various approximations possible in this problem, and determine the limits of their validity and utility.
3. To find means of combining the simple-body solutions in order to determine the cross-sections of composite bodies.
4. To tabulate various formulas and functions necessary to enable such computations to be done quickly for arbitrary objects.
5. To collect, summarize, and evaluate existing experimental data.

Titles of the papers already published or presently in process of publication are listed on the back of the title page.

K. M. Siegel

UNIVERSITY OF MICHIGAN

2260-1-T

I

INTRODUCTION

The radar cross-section (σ) of aircraft has always been a difficult parameter to ascertain with any great precision. Even the first significant figure has always been subject to considerable doubt. Such information is important enough to warrant a good deal of experimental and theoretical effort. Kerr (Ref. 1) states: "Because of the need for some means of describing complex targets certain desperate artifices have been evolved to preserve the concept of cross-section for such targets."

Kerr also points out that: "For longer radar wavelengths, greater than about 1 meter, a large amount of work has been done to calculate σ by treating sections of the aircraft as cylinders, ellipsoids, or various combinations of curved surfaces. Some of these methods have achieved a moderate degree of success." This report employs the method referred to above; the method is used, at wavelengths both smaller and larger than 1 meter, to compute the cross-sections of B-47 and B-52 aircraft for many aspects.

This study was carried out during May, June, and part of July 1954 at the Willow Run Research Center. More than thirty members of the technical staff participated in the work, including members of the Theory and Analysis Department under K. M. Siegel, members of the Data Reduction and Computation Department under D. M. Brown, and members of the Digital Computation Department under J. W. Carr III. The computations involved use of slide rules, desk calculating machines, IBM computing equipment, and the MIDAC (Michigan Digital Automatic Computer).

The theoretical data obtained for the B-47 aircraft are presented in Section II. The B-52 data are presented in Section III. The theoretical data for the B-47 are compared with experimental data in Section IV. Similar comparisons were not possible for the B-52 because of the lack of availability of such data.

Appendix A contains the notes, prepared by one of the authors

~~CONFIDENTIAL~~

UNIVERSITY OF MICHIGAN

2260-1-T

(C. E. Schensted), which were used as the basis for the computations. These notes show the method by which the computations were obtained, and may serve as reference material for other workers in the field. Appendix B contains drawings of the two aircraft and describes the breakdowns into simple shapes which were used for computational purposes.

It is hoped that this report will serve three major purposes:

1. That it will provide better values of B-47 and B-52 radar cross-sections than had been available heretofore.
2. That it will provide sufficient background information for the computation of the radar cross-sections of complex configurations.
3. That it will serve as a stepping stone for further research in the computation of the radar cross-section of complex configurations.

~~CONFIDENTIAL~~

II

THEORETICAL CROSS-SECTIONS OF
B-47 AIRCRAFT

2.1 METHOD

The theoretically computed radar cross-sections of the B-47 are summarized in this section in graphical form. The cross-sections were computed at seven different wavelengths as a function of the two aspect angles, β and γ , shown in Figure 2.1-1.

The seven wavelengths are:

$$\lambda = 0.1 \text{ ft} = 3.05 \text{ cm} \approx 3 \text{ cm}$$

$$\lambda = 0.3 \text{ ft} = 9.14 \text{ cm} \approx 9 \text{ cm}$$

$$\lambda = 0.4 \text{ ft} = 12.2 \text{ cm} \approx 12 \text{ cm}$$

$$\lambda = 0.6 \text{ ft} = 18.3 \text{ cm} \approx 18 \text{ cm}$$

$$\lambda = 1.0 \text{ ft} = 30.5 \text{ cm} \approx 30 \text{ cm}$$

$$\lambda = 3.0 \text{ ft} = 91.4 \text{ cm} \approx 91 \text{ cm}$$

$$\lambda = 15.0 \text{ ft} = 4.57 \text{ m} \approx 4.5 \text{ m}$$

Computations were made for each of these seven wavelengths and each of eight different values of β (-4° , 0° , 4° , 8° , 12° , 30° , 60° , and 90°) for many values of γ in the region $0^\circ \leq \gamma \leq 180^\circ$. Computations in γ were made at 5° intervals and for each λ and β the peak points in γ were computed as were the one-half (and in some cases the one-tenth) peak points.

As exact computational methods are not available at present, the aircraft was broken up into parts which were fitted by relatively simple shapes whose cross-sections can be computed approximately. Then the approximate cross-sections of these components were combined appropriately to obtain the cross-section of the aircraft itself¹.

¹ A general discussion of this breakdown procedure is given in Appendix A, and the specific breakdown used for the B-47 is discussed in Appendix B.

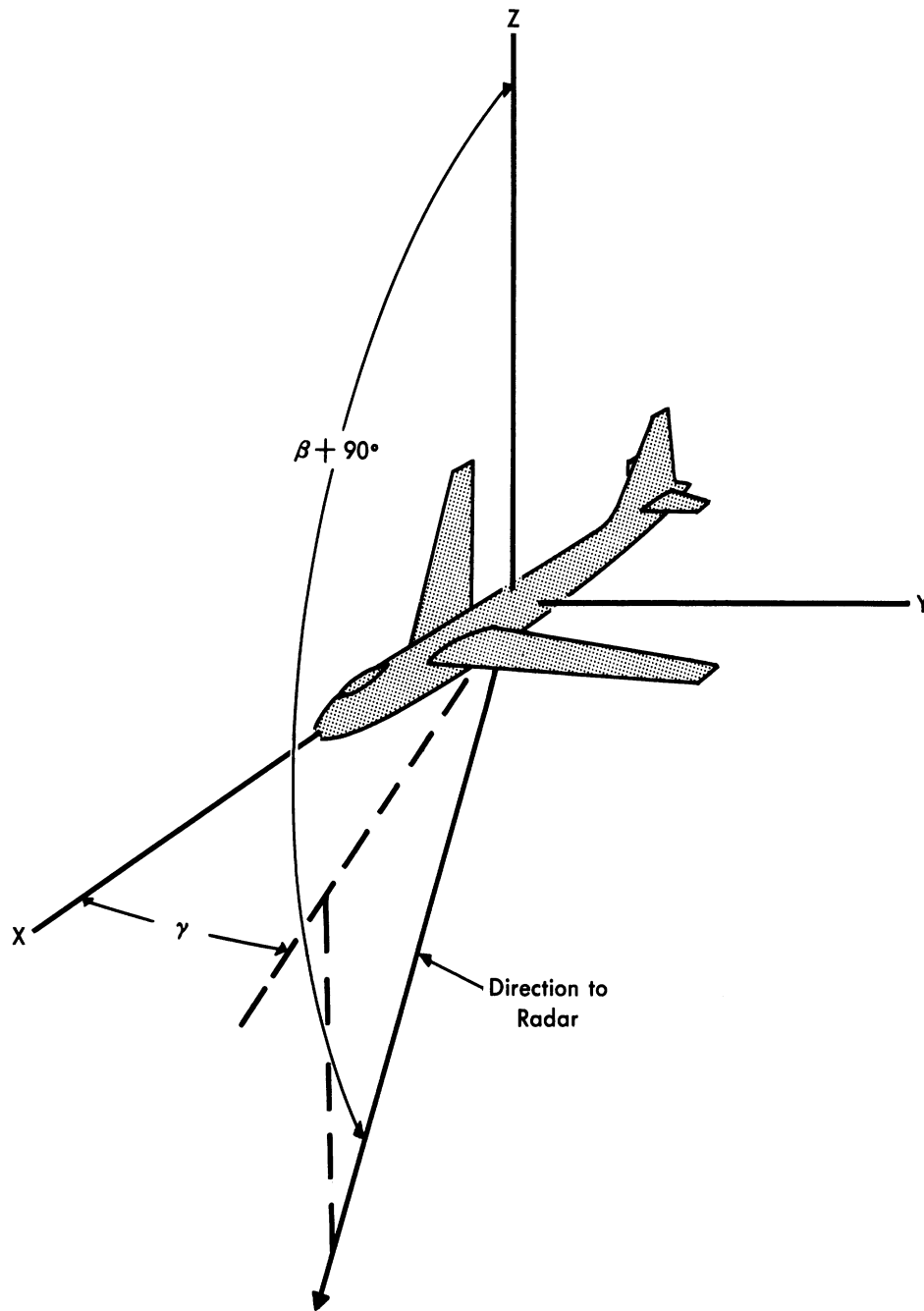


FIG. 2.1-1 BASIC COORDINATE SYSTEM USED IN DETERMINING THE CROSS-SECTIONS

~~CONFIDENTIAL~~
~~CONFIDENTIAL~~

UNIVERSITY OF MICHIGAN

2260-1-T

In performing the breakdown, the judgment of the physicist or mathematician setting up the computations comes into play; his judgment is influenced not only by familiarity with theoretical material (such as that in Appendix A), but also by the accuracy required in the results, by the amount of detail shown on the available drawings of the aircraft, and by the time and computing facilities which are available. To allow for this relative arbitrariness in procedure and consequent uncertainty in the results, the cross-section of the B-47 was computed independently by two methods.

In Method I, the numerical computations were done by slide-rule. In Method II, the computations were done primarily on IBM machines and on MIDAC. The two methods also differed in that the B-47 was broken down into a larger number of components in Method II than in Method I. The different breakdowns used in the two methods result in different sized components. These differences can result in marked discrepancies arising at aspects at which a particular component, having a different size in the two methods, dominates the computed cross-section.

Since only small drawings of the B-47 were available, many of the angles involved had to be measured with a protractor. Some of the approximation formulas used are very sensitive to changes in the angle parameters. Thus, a slight difference in the measurement of an angle on an aircraft drawing can result in marked differences in the computed value of σ for a particular choice of β , γ , and λ .

It should be kept in mind that discrepancies are not physically significant if they are too small to be measured in the field. Some comparatively large discrepancies which arise from the two methods, and which are due to differences of opinion as to what the B-47 looks like (in regions where the results are sensitive to shape) could be resolved, at least partially, by recomputing the cross-section using more accurate data concerning the aircraft. However, such a procedure hardly seems worthwhile since later versions of the B-47 might have slightly different shapes. It is important to observe that the results of the two methods are in general agreement (to within a factor of 2 to 5) for almost all of the wavelengths and aspects considered. More precise comparisons between the results of the two methods are made in the Sections 2.2, 2.3, and 2.4.

The graphs appearing in this section show the envelopes of the computed data. The cross-section varies rapidly with aspect and the computed values represent averages. In making these graphs, the largest and smallest computed value of σ , for a particular set of λ and β values were plotted as a function of γ . (For example, on Figure 2.2-1 all of the values of cross-section computed for $\gamma = 20^\circ$, for $\beta = -4^\circ, 0^\circ$, and 4° and $\lambda = 3.05$ cm, 9.14 cm, and 12.2 cm were between 1.1 and 2.7 square meters.) The envelopes drawn with solid curves are for horizontal polarization and the envelopes for vertical polarization are shown with broken lines. In those regions of γ for which the envelopes of the vertical polarization data are not shown, they coincide with the envelopes for the horizontal polarization data. The method of presentation employed occasionally results in a large number of peaks due to a shift of the peak position with a change of β and due to the somewhat different positions obtained for the peaks in the two methods of computation. These "extra" peaks are shown on the graphs.

2.2 X- AND S-BAND CROSS-SECTIONS

All the X-band and S-band cross-section computations for the B-47 are summarized in Figures 2.2-1, 2.2-2, 2.2-3, and 2.2-4, as a function of γ , with the exception of the values of cross-section corresponding to $\beta = 90^\circ$ for which γ is indeterminate. At this aspect, the results obtained were:

$$\begin{aligned}\sigma &\approx 1 \times 10^4 \text{ square meters } (\lambda = 3.05 \text{ cm}), \\ \sigma &\approx 5 \times 10^3 \text{ square meters } (\lambda = 9.14 \text{ cm}), \\ \text{and } \sigma &\approx 5 \times 10^3 \text{ square meters } (\lambda = 12.2 \text{ cm}).\end{aligned}$$

The data for $\beta = -4^\circ, 0^\circ$, and 4° are summarized in Figure 2.2-1; the $\beta = 8^\circ$ and 12° data in Figure 2.2-2; the $\beta = 30^\circ$ data in Figure 2.2-3; and the $\beta = 60^\circ$ data in Figure 2.2-4.

Examination of these graphs shows that the results obtained by the two methods are in very good agreement with one another (within a factor of from 2 to 5) for all values of γ except, in some cases, in the neighborhood of sharp peaks in σ and in the region $100^\circ < \gamma < 140^\circ$.

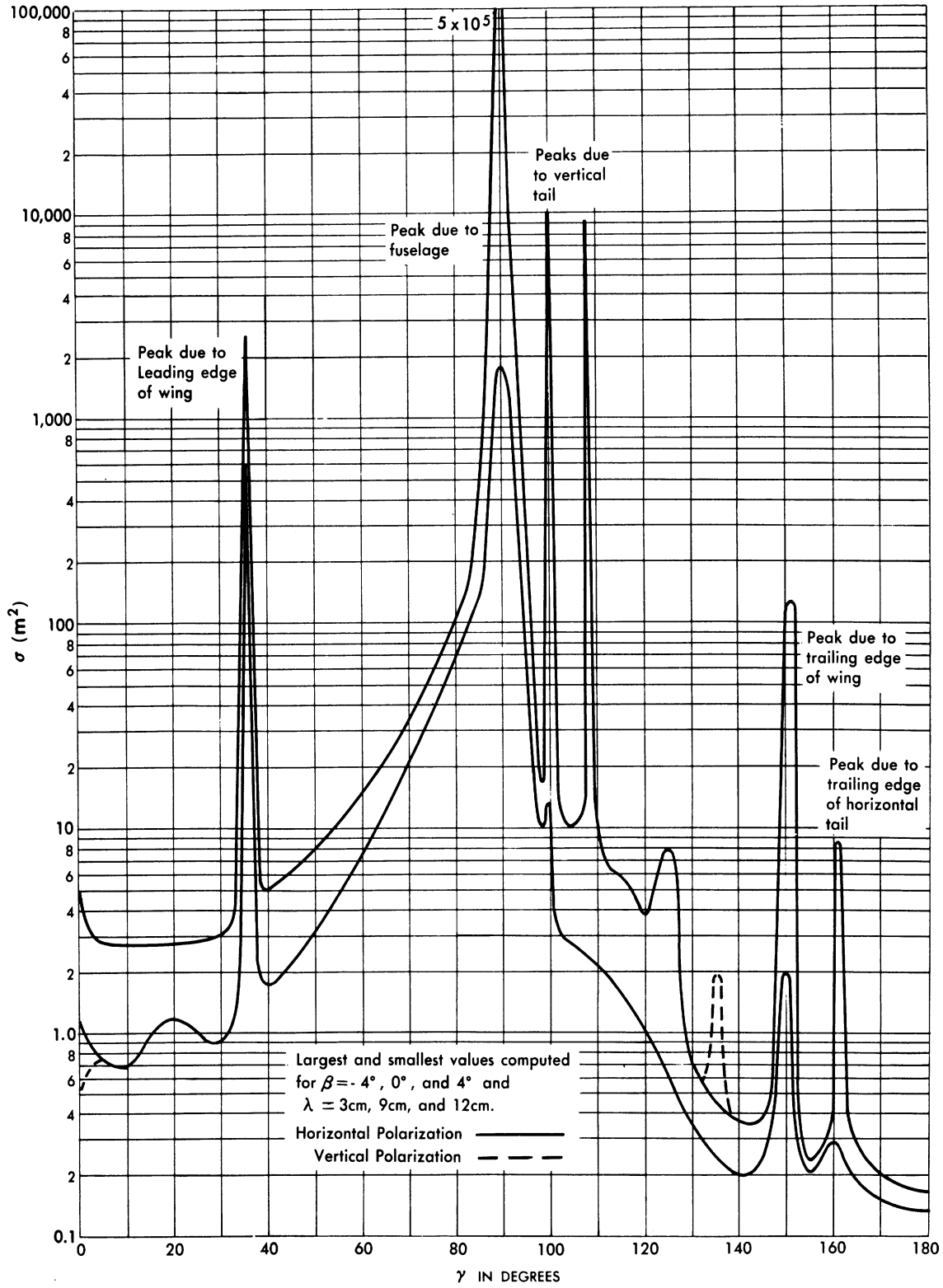


FIG. 2.2-1 CROSS-SECTION OF A B-47 AT X- AND S-BAND FREQUENCIES FOR $-4^\circ \leq \beta \leq 4^\circ$

2260-1-T

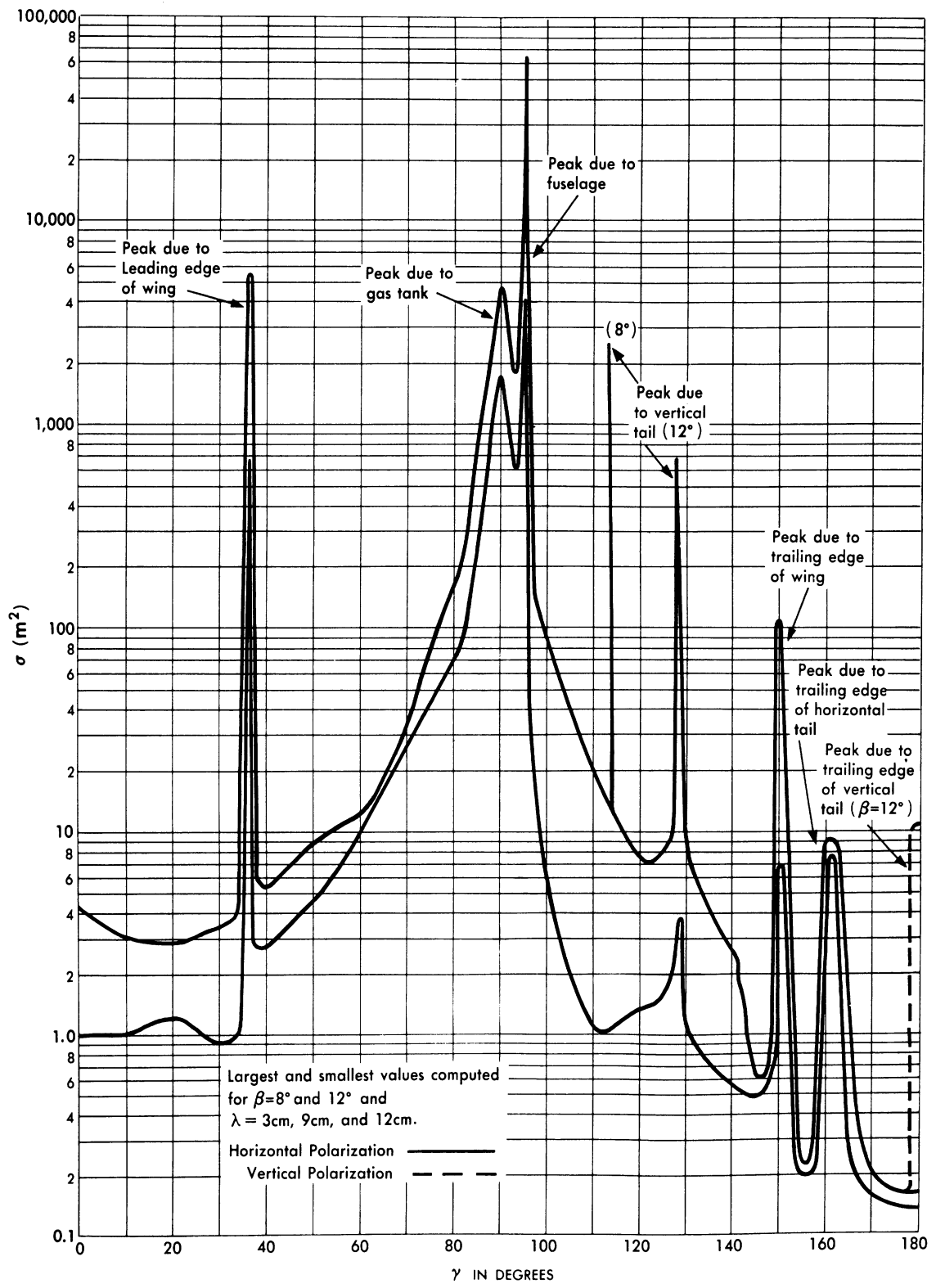


FIG. 2.2 - 2 CROSS - SECTION OF A B - 47 AT X - AND S - BAND FREQUENCIES FOR $8^\circ \leq \beta \leq 12^\circ$.

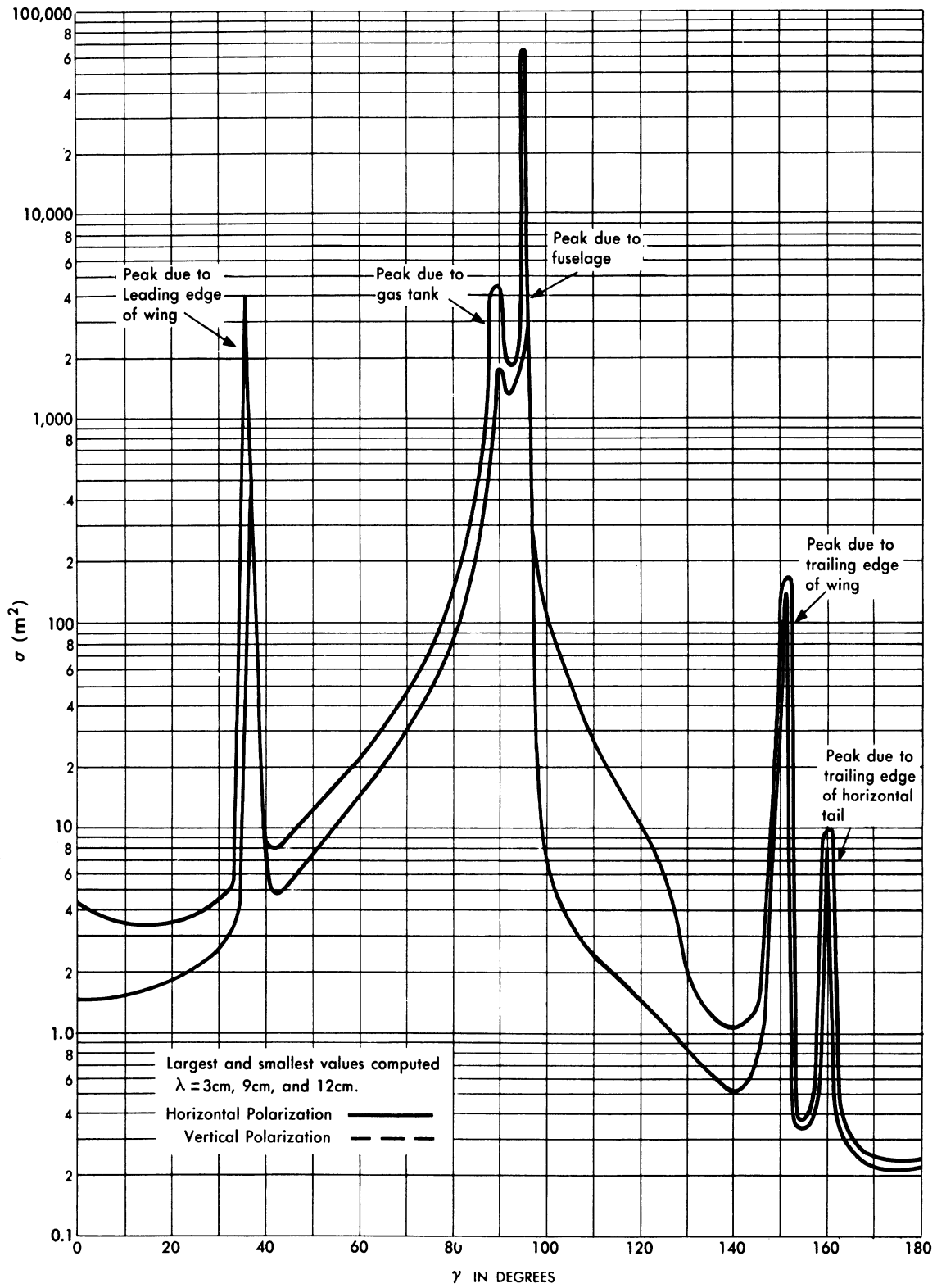


FIG. 2.2-3 CROSS-SECTION OF A B-47 AT X- AND S-BAND
FREQUENCIES $\beta = 30^\circ$

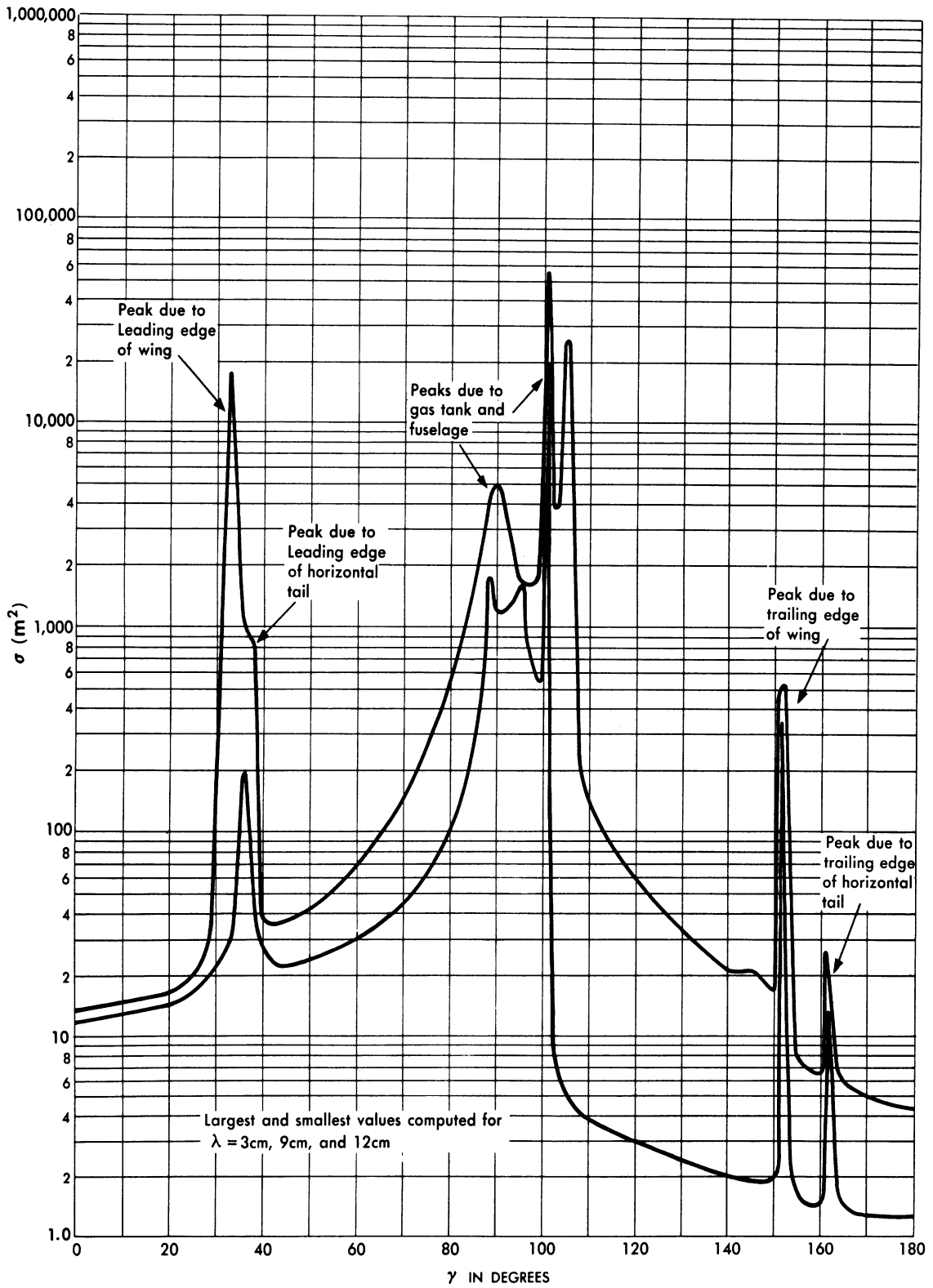


FIG. 2.2-4 CROSS-SECTION OF A B-47 AT X- AND S-BAND FREQUENCIES FOR $\beta=60^\circ$

Larger differences are to be expected at the peaks than elsewhere due to the differences between the two methods; the differences in the $100^{\circ} < \gamma < 140^{\circ}$ region are due to variations in the interpretation of the appearance of the B-47 and to slight differences in the manner in which the angles on the B-47 drawings were measured in the two methods.

2.3 L-BAND CROSS-SECTIONS

The cross-sections of a B-47 computed at the L-band wavelengths of $\lambda = 18.3$ cm and $\lambda = 30.5$ cm are summarized in Figures 2.3-1 through 2.3-4 in the same manner as the X- and S-band data in Section 2.2. The comments made in Section 2.2 concerning the differences resulting from the two methods also apply to the L-band data.

As in Section 2.2, the $\beta = 90^{\circ}$ results are not displayed graphically; the results obtained for $\beta = 90^{\circ}$ at these wavelengths are

$$\begin{aligned} \sigma &\approx 5 \times 10^3 \text{ square meters } (\lambda = 18.3 \text{ cm}) \\ \text{and } \sigma &\approx 6 \times 10^3 \text{ square meters } (\lambda = 30.5 \text{ cm}) . \end{aligned}$$

2.4 CROSS-SECTIONS FOR $\lambda = 91.4$ cm and $\lambda = 4.57$ m

The computations of the cross-section of a B-47 for the wavelengths $\lambda = 91.4$ cm and $\lambda = 4.57$ m are summarized in Figures 2.4-1 through 2.4-8. The data obtained from the two methods are presented in the same manner as in the two preceding sections except that only one frequency is shown per graph. The data shown on each of the eight figures are:

- Figure 2.4-1: $\beta = -4^{\circ}, 0^{\circ}, \text{ and } 4^{\circ}$; $\lambda = 91.4$ cm
- Figure 2.4-2: $\beta = -4^{\circ}, 0^{\circ}, \text{ and } 4^{\circ}$; $\lambda = 4.57$ m
- Figure 2.4-3: $\beta = 12^{\circ}$; $\lambda = 91.4$ cm
- Figure 2.4-4: $\beta = 12^{\circ}$; $\lambda = 4.57$ m
- Figure 2.4-5: $\beta = 30^{\circ}$; $\lambda = 91.4$ cm
- Figure 2.4-6: $\beta = 30^{\circ}$; $\lambda = 4.57$ m
- Figure 2.4-7: $\beta = 60^{\circ}$; $\lambda = 91.4$ cm
- Figure 2.4-8: $\beta = 60^{\circ}$; $\lambda = 4.57$ m

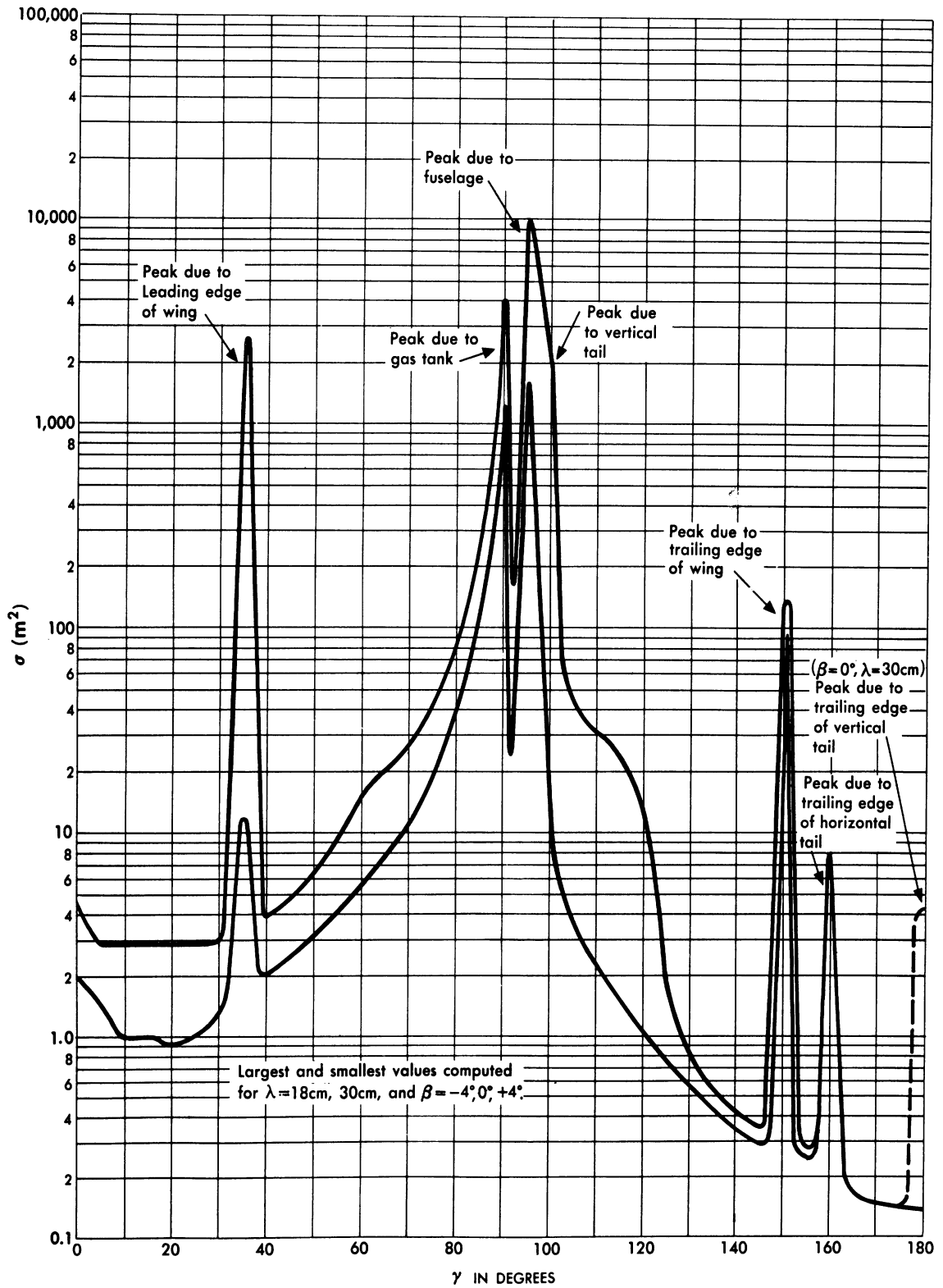


FIG. 2.3 - 1 CROSS - SECTION OF A B - 47 AT L - BAND FREQUENCIES FOR $-4^\circ \leq \beta \leq +4^\circ$.

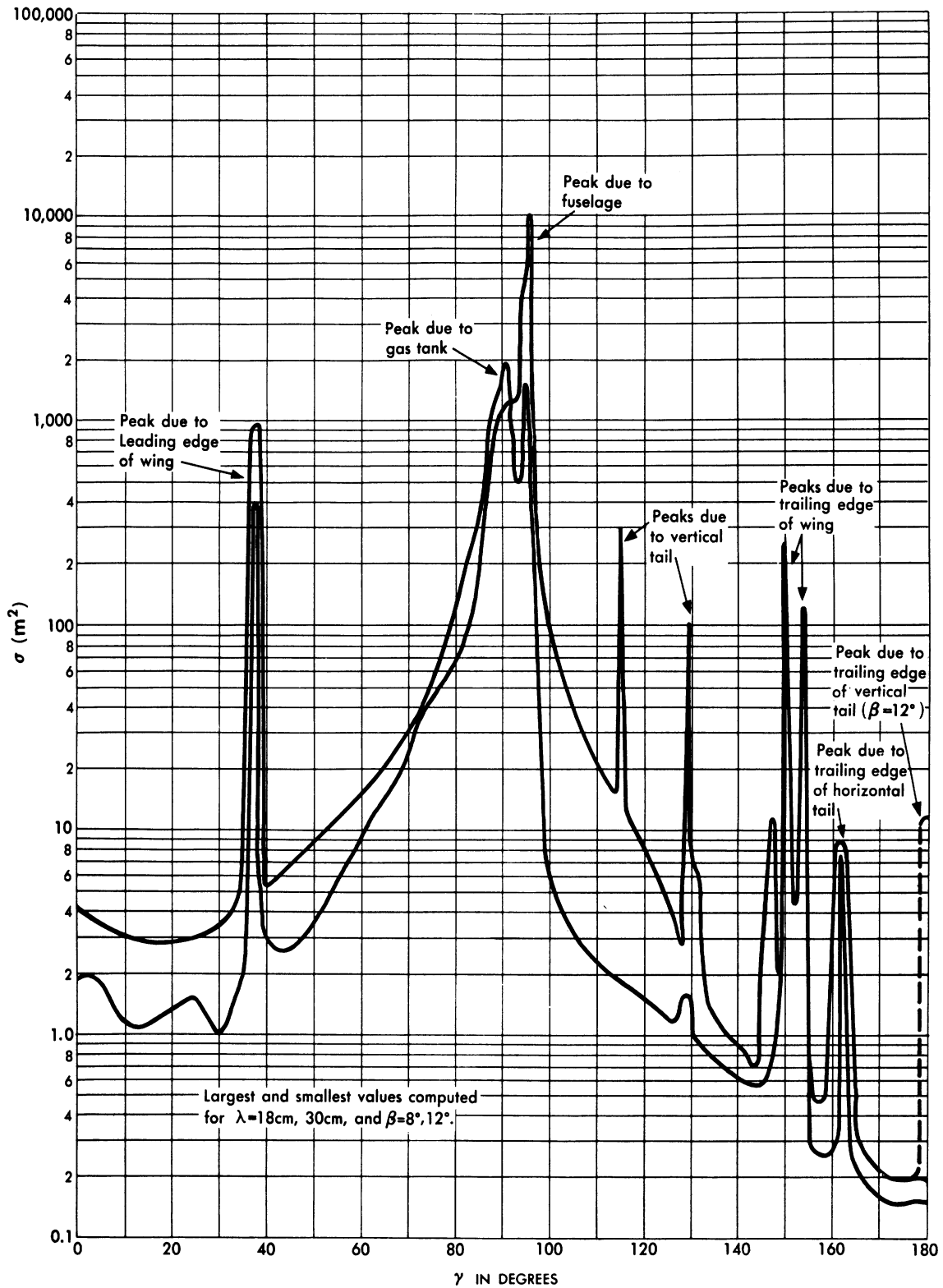


FIG. 2.3-2 CROSS-SECTION OF A B-47 AT L-BAND FREQUENCIES FOR $8^\circ \leq \beta \leq 12^\circ$.

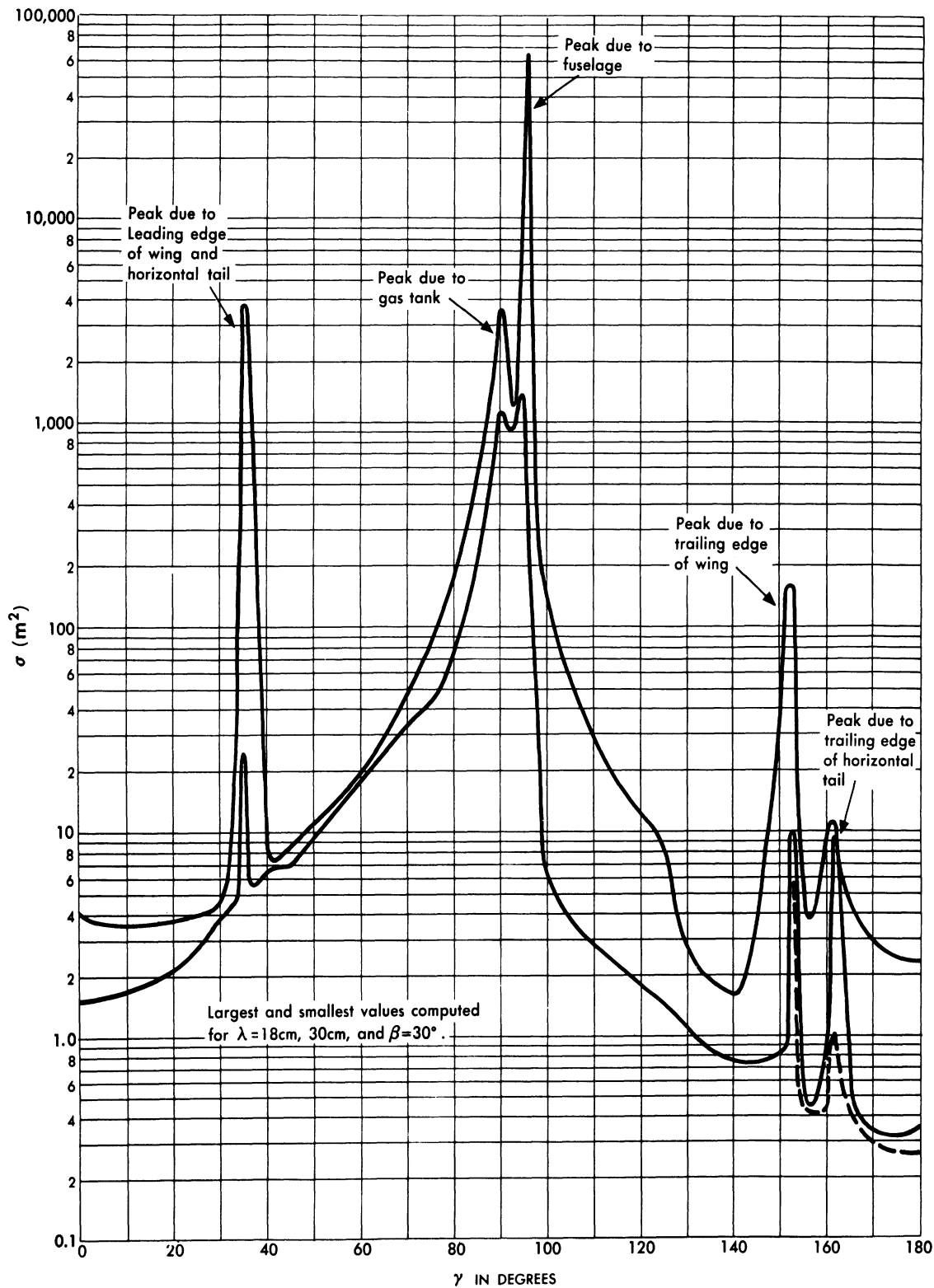


FIG. 2.3 - 3 CROSS - SECTION OF A B - 47 AT L - BAND
FREQUENCIES FOR $\beta = 30^\circ$

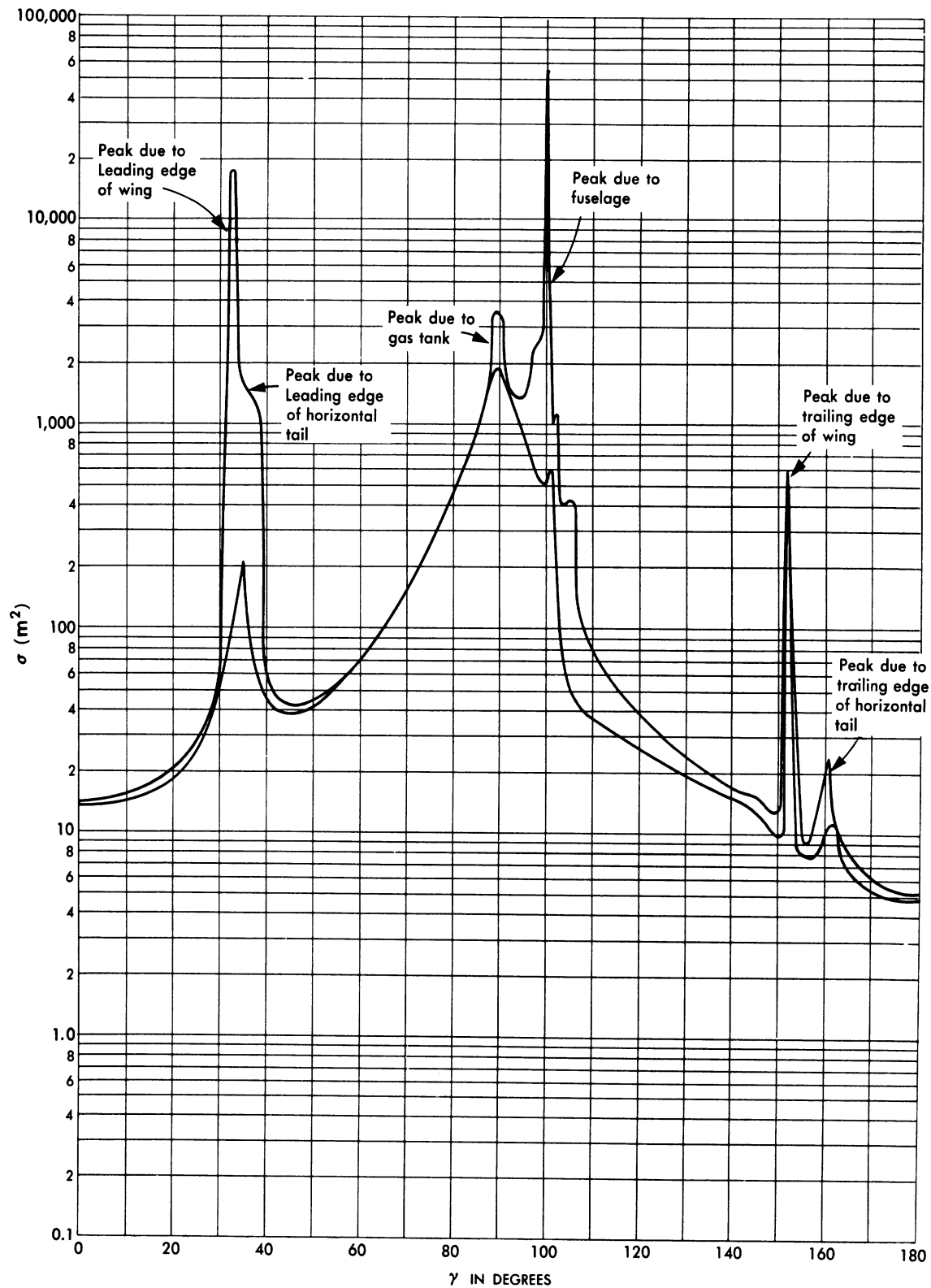


FIG. 2.3-4 CROSS-SECTION OF A B-47 AT L-BAND FREQUENCIES FOR $\beta = 60^\circ$ (Largest and Smallest Values Computed for $\lambda = 18$ cm and 30 cm)

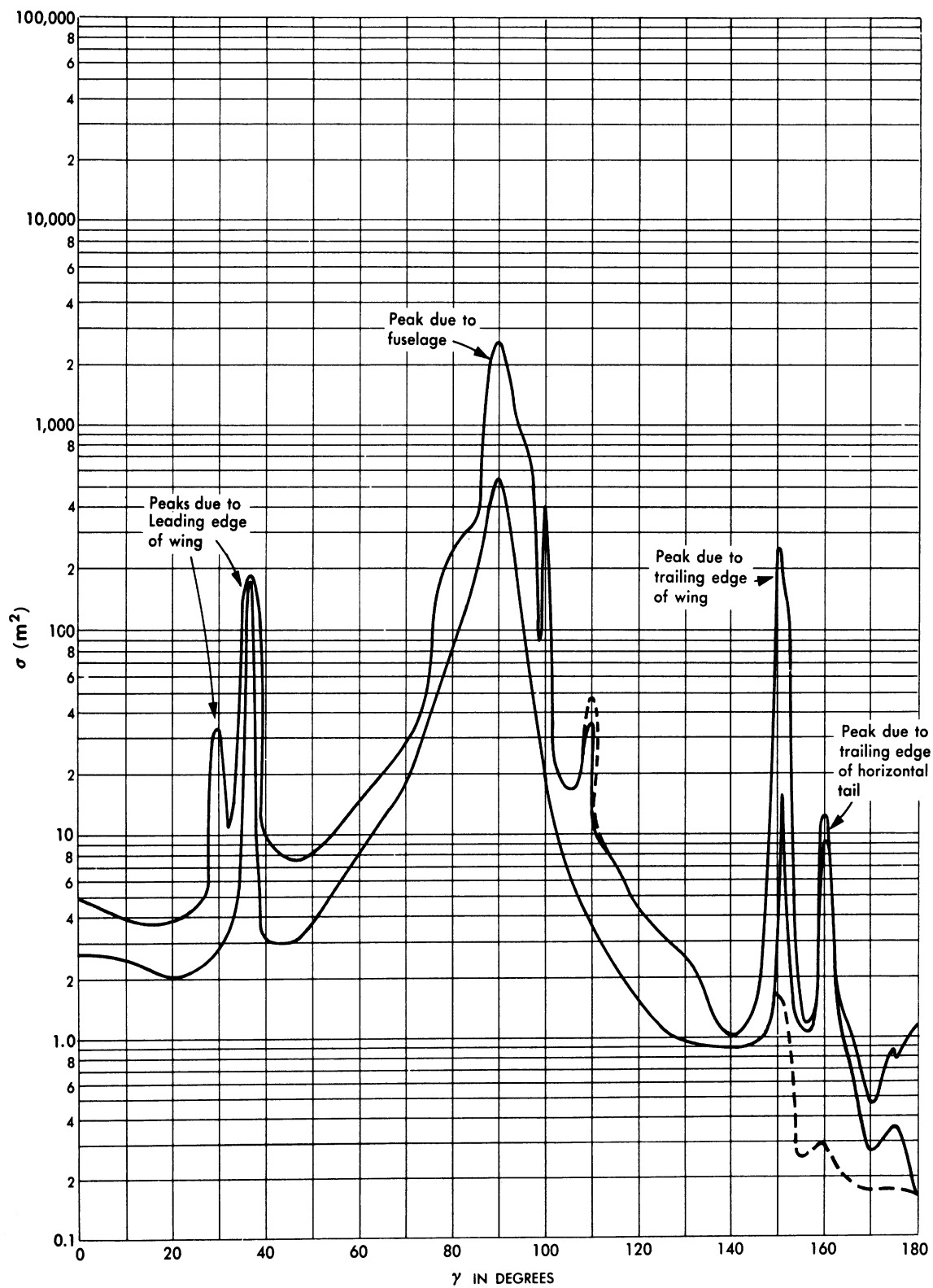


FIG. 2.4-1 CROSS-SECTION OF A B-47 FOR $\lambda=91.4 \text{ cm. AND } -4^\circ \leq \beta \leq +4^\circ$
(Largest and Smallest Values Computed)

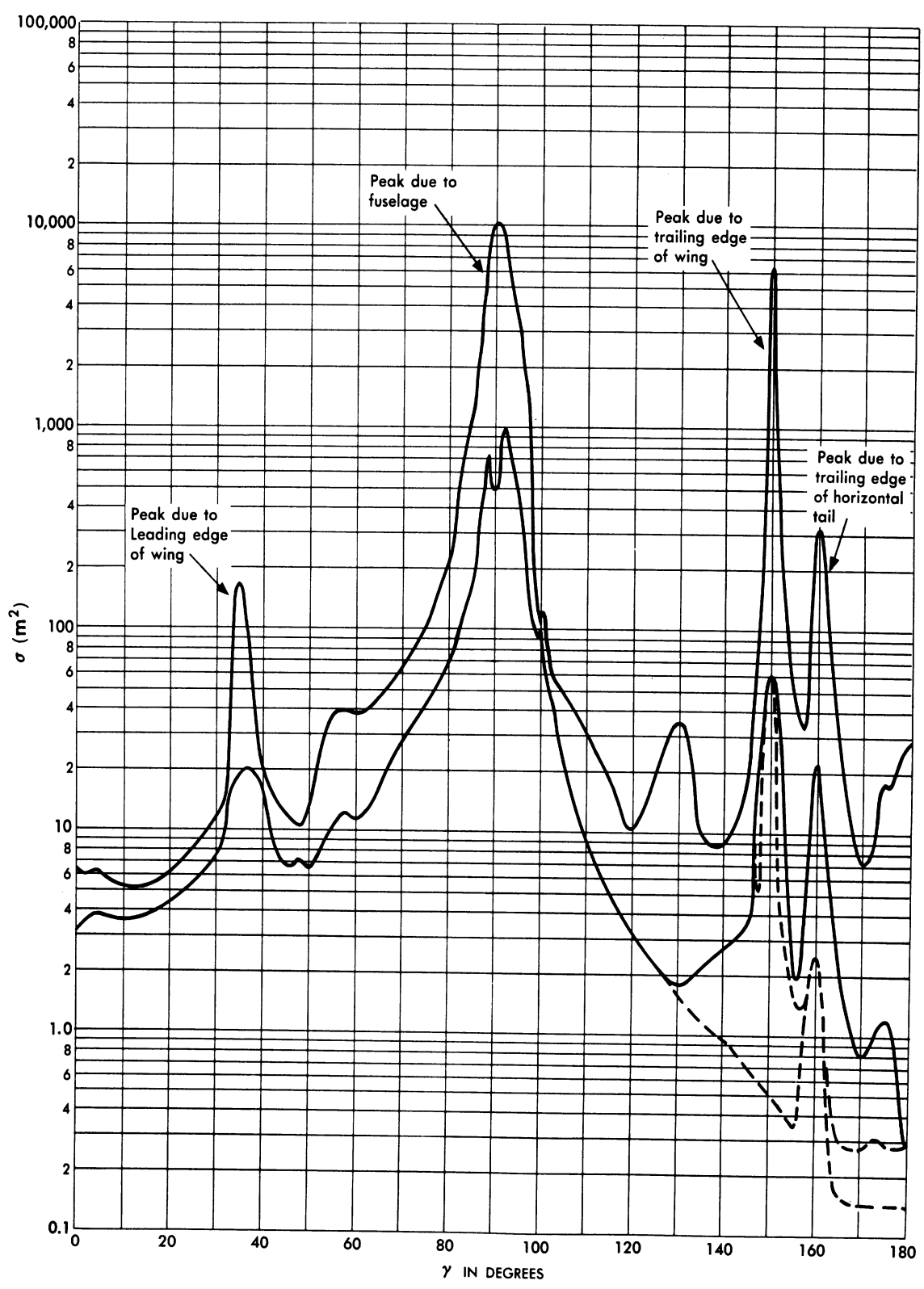


FIG. 2.4-2 CROSS-SECTION OF A B-47 FOR $\lambda=4.57$ m AND $-4^\circ \leq \beta \leq +4^\circ$
(Largest and Smallest Values Computed)

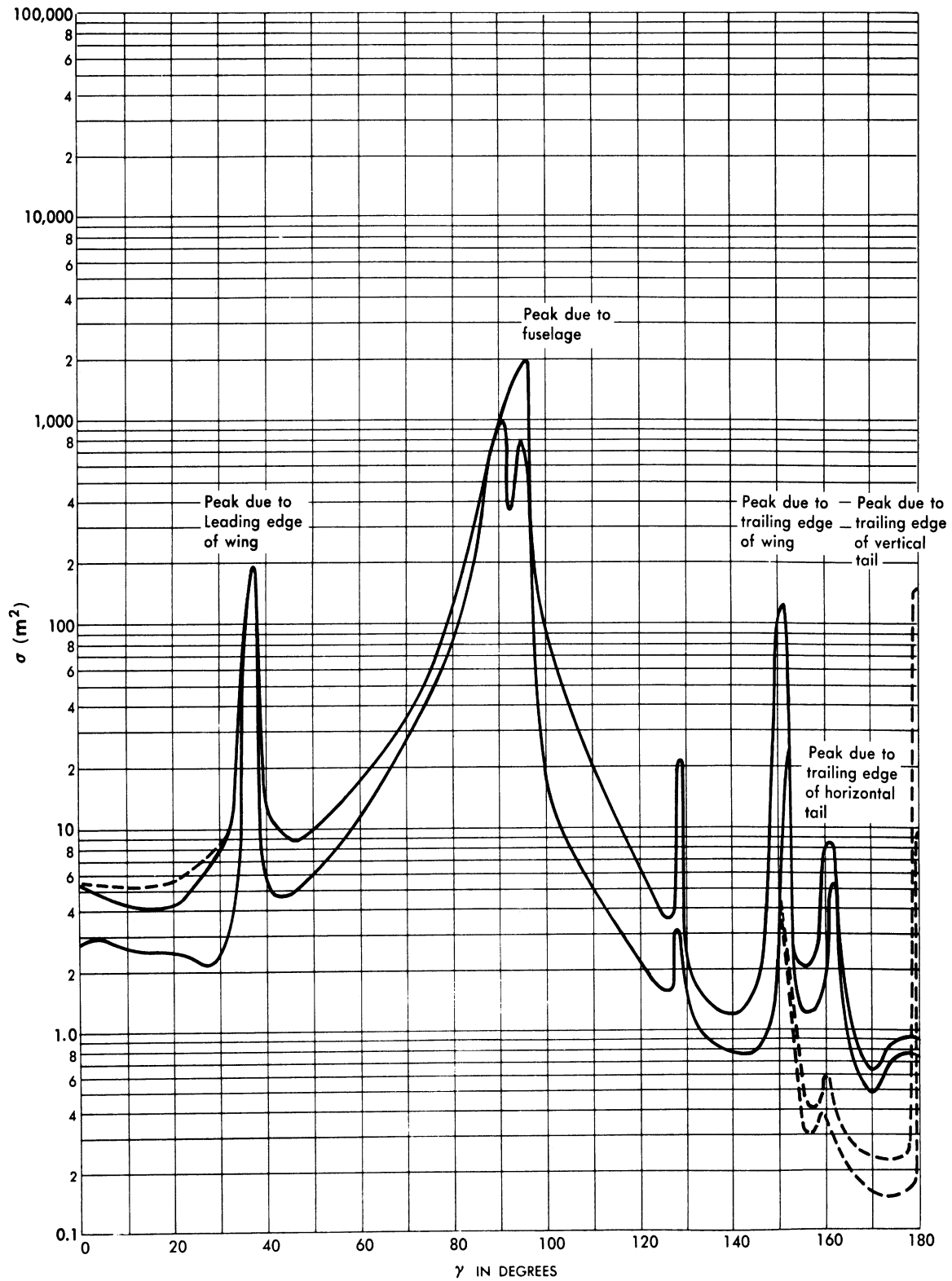


FIG. 2.4-3 CROSS-SECTION OF A B-47 FOR $\beta=12^\circ$ AND $\lambda=91.4m$.
(Largest and Smallest Values Computed)

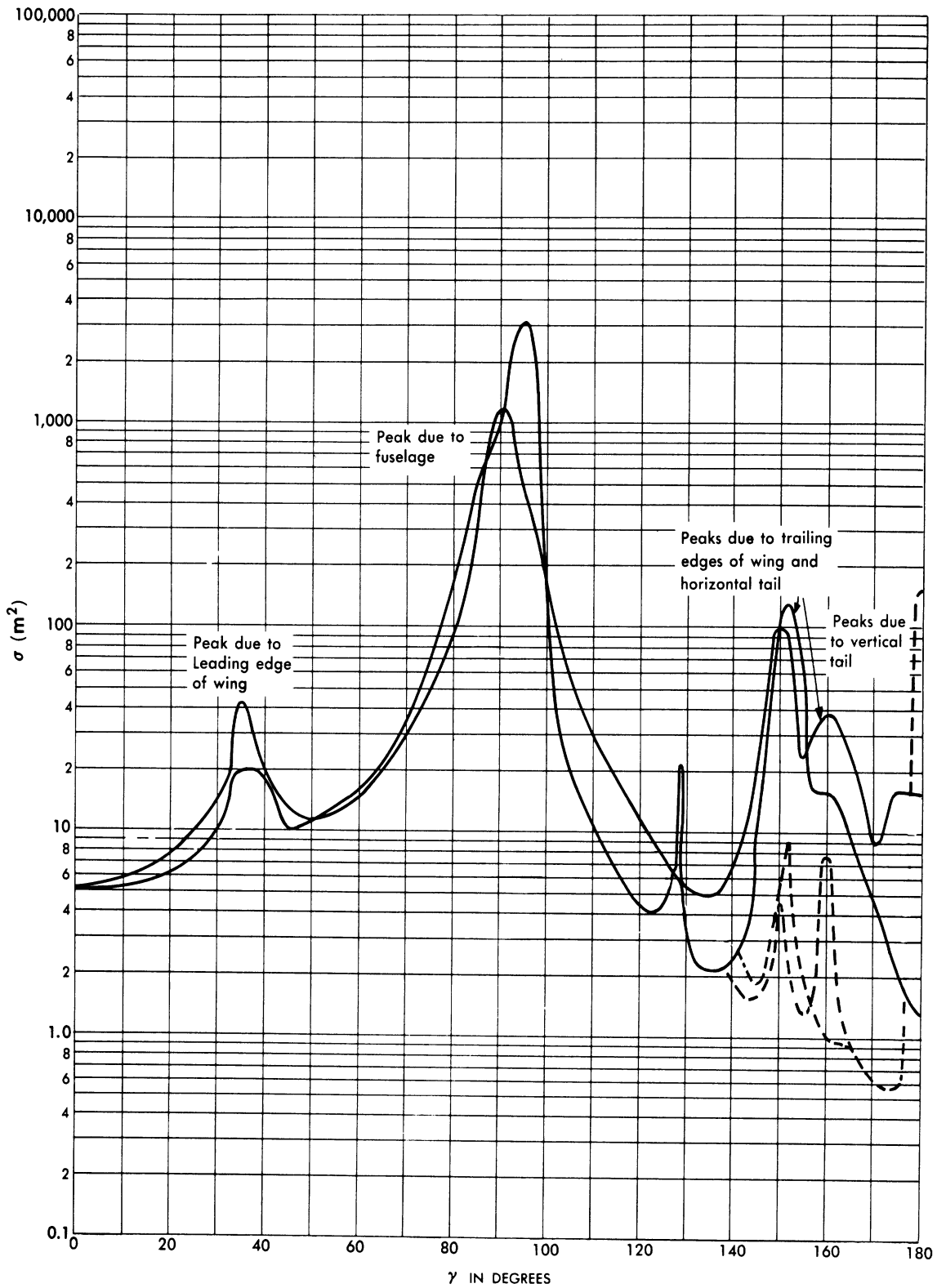


FIG. 2.4-4 CROSS-SECTION OF A B-47 FOR $\beta = 12^\circ$ AND $\lambda = 4.57$ m
(Largest and Smallest Values Computed)

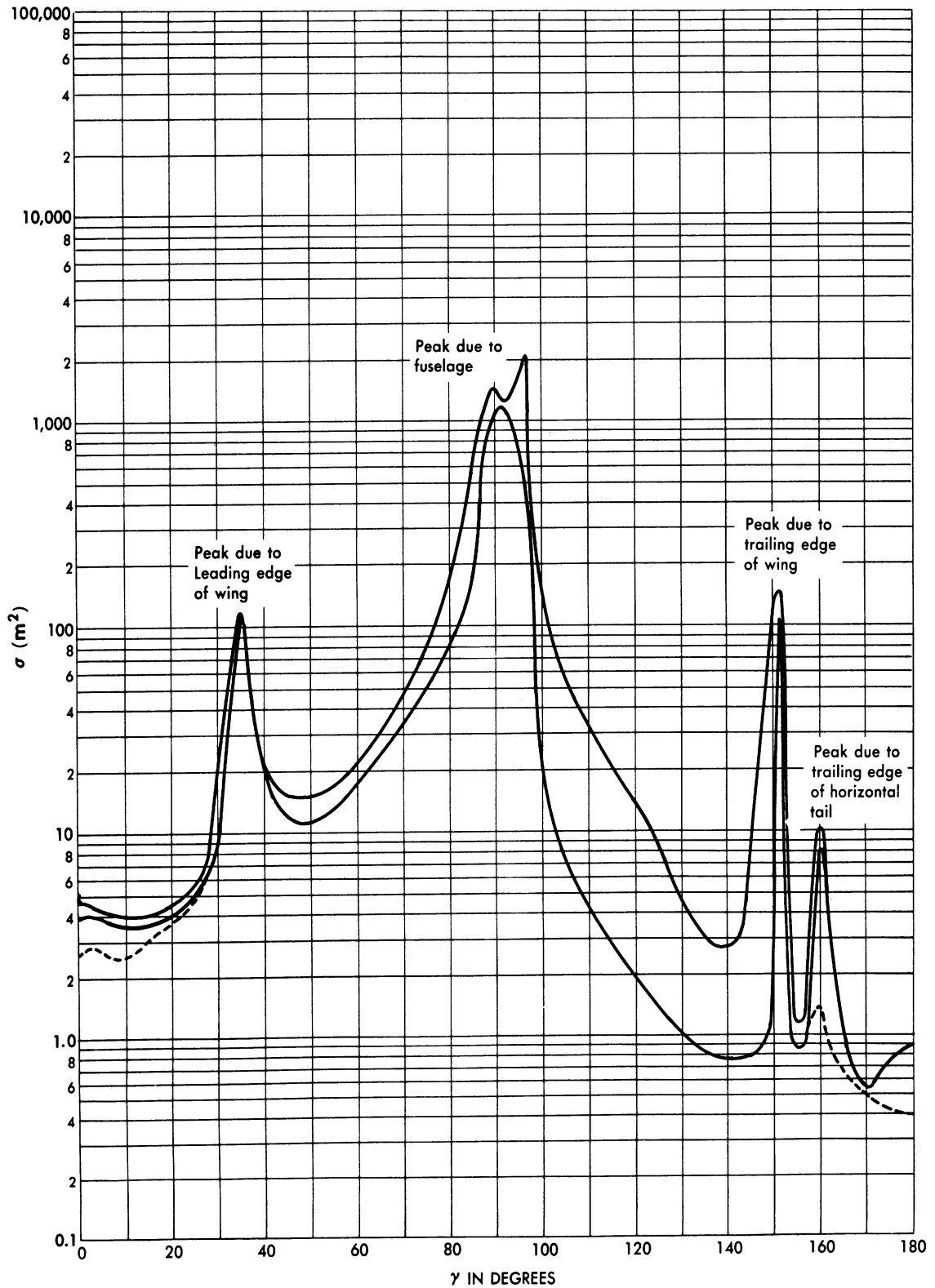


FIG. 2.4-5 CROSS-SECTION OF A B-47 FOR $\beta = 30^\circ$ AND $\lambda = 91.4$ cm.
(Largest and Smallest Values Computed)

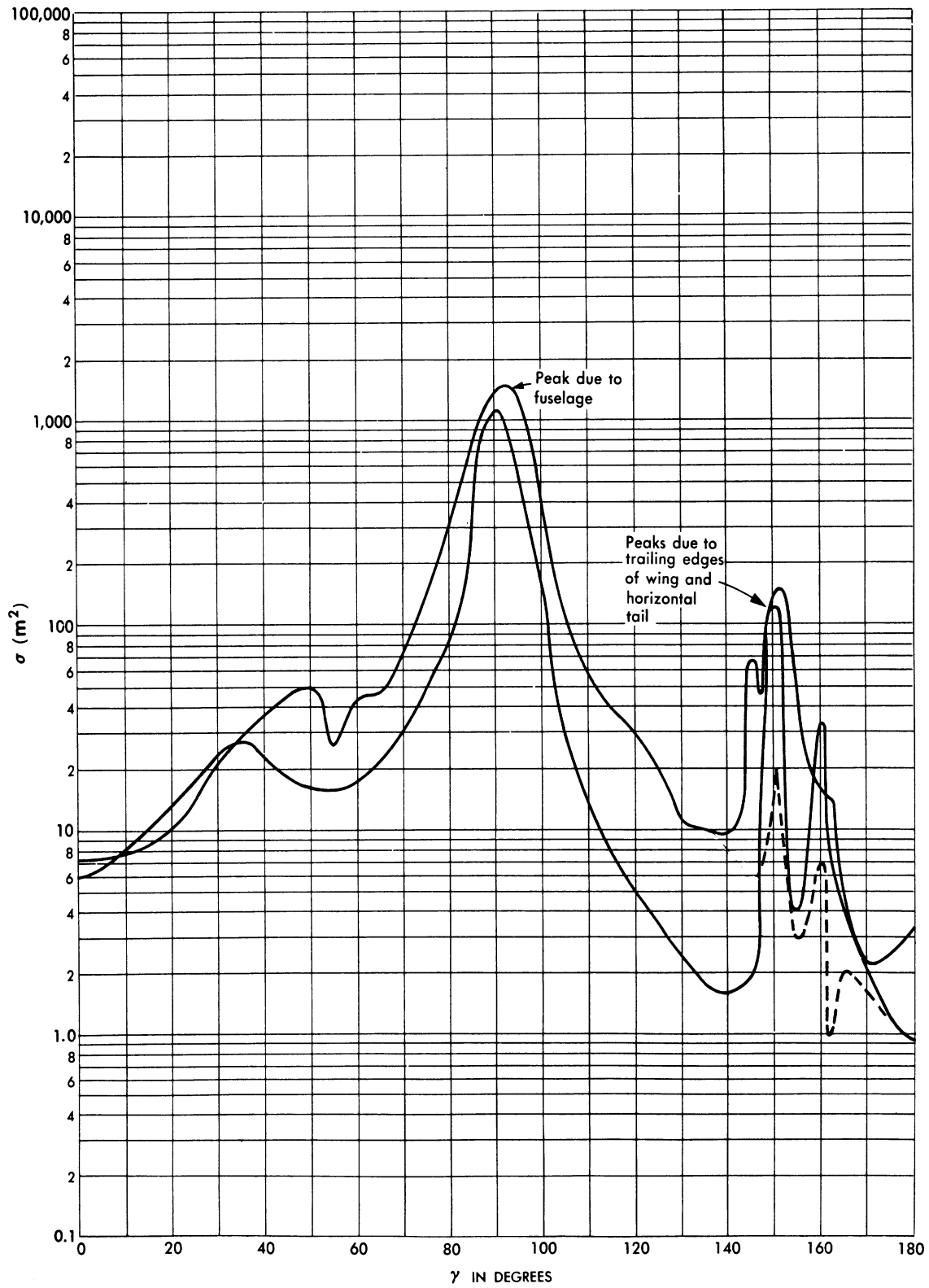


FIG. 2.4-6 CROSS-SECTION OF A B-47 FOR $\beta = 30^\circ$ AND $\lambda = 4.57$ m
(Largest and Smallest Values Computed)

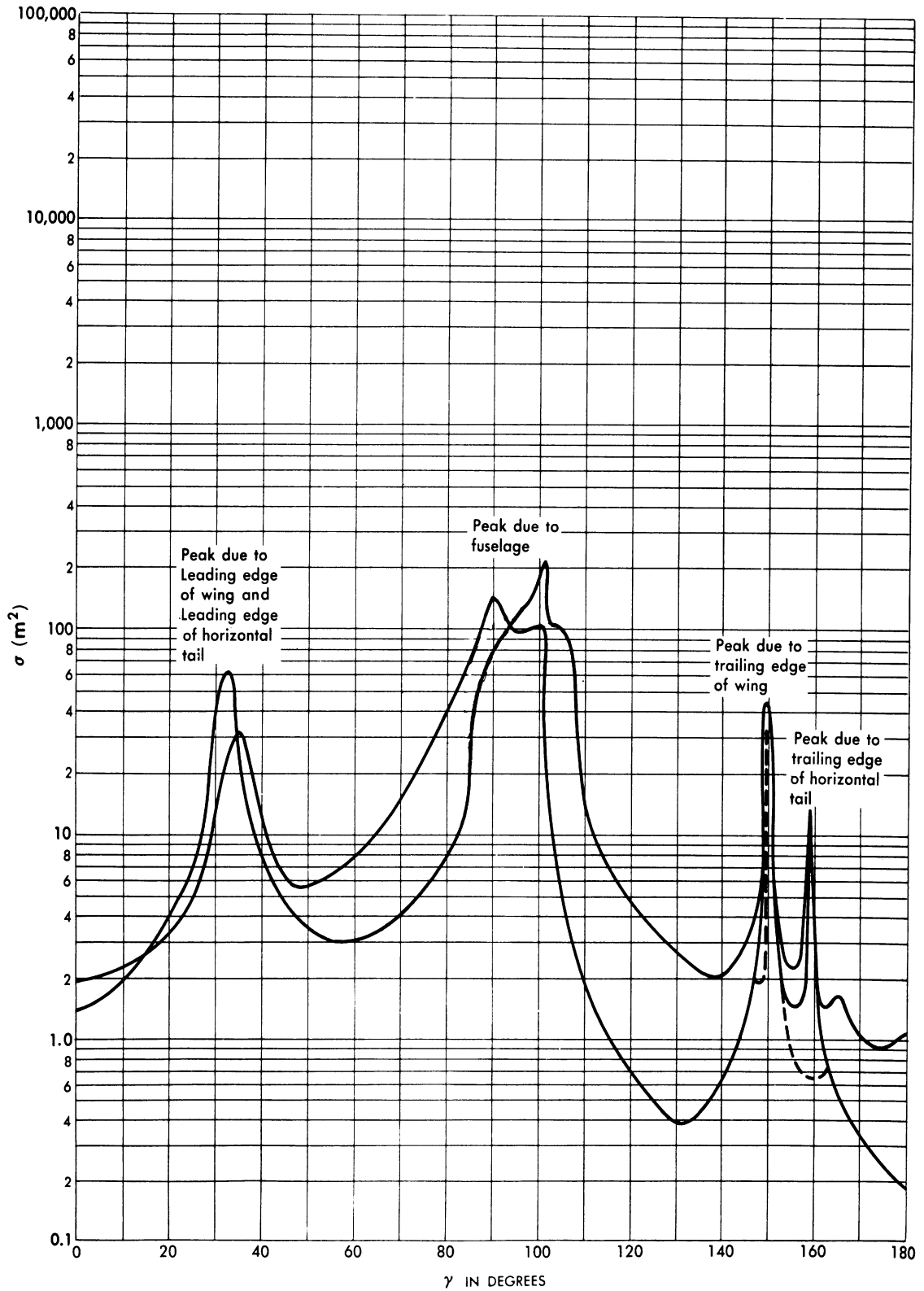


FIG. 2.4-7 CROSS-SECTION OF A B-47 FOR $\beta=60^\circ$ AND $\lambda=91.4$ m.
(Largest and Smallest Values Computed)

~~CONFIDENTIAL~~

UNIVERSITY OF MICHIGAN

2260-1-T

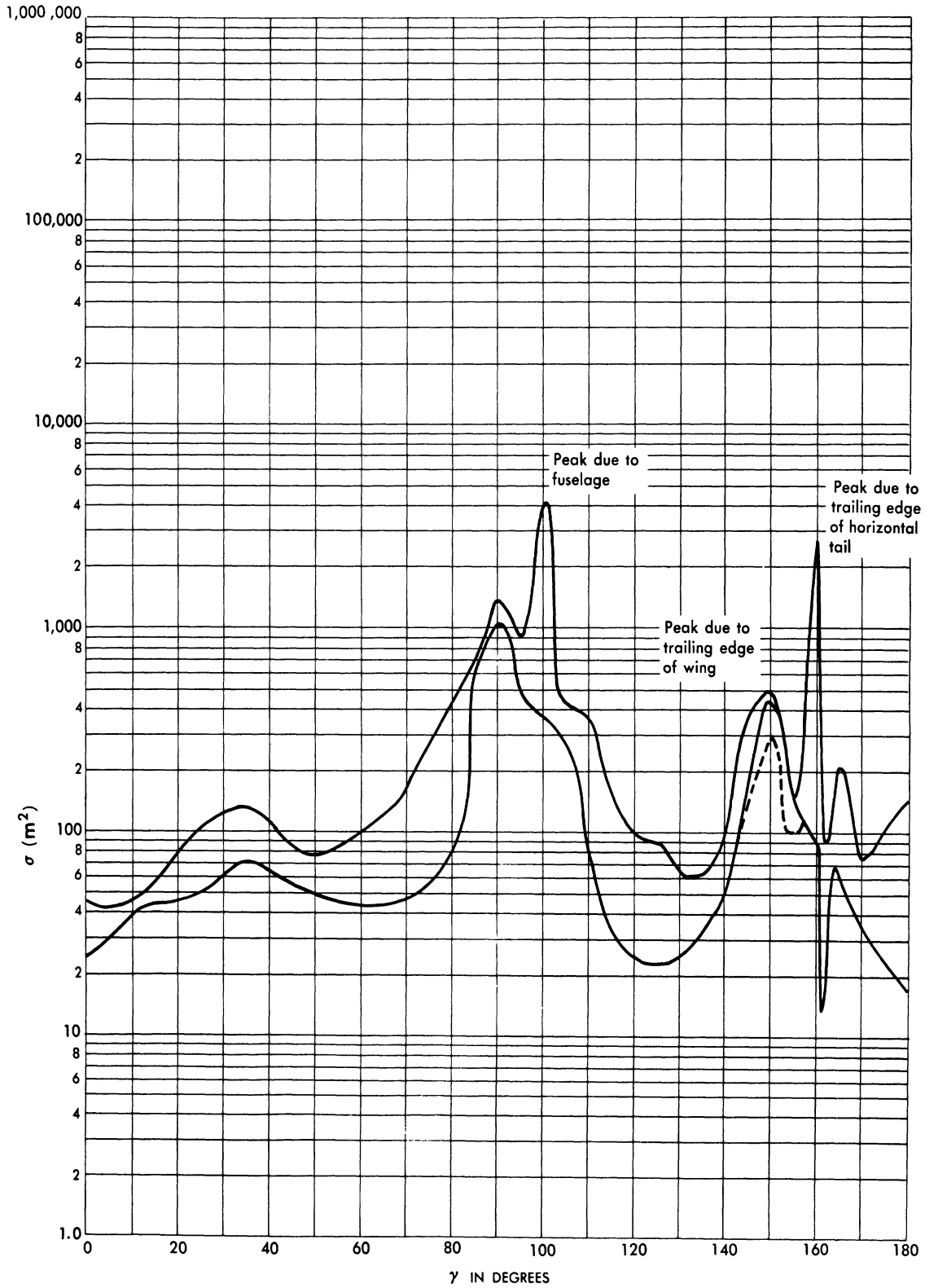


FIG. 2.4-8 CROSS-SECTION OF A B-47 FOR $\beta = 60^\circ$ AND $\lambda = 4.57$ m
(Largest and Smallest Values Computed)

~~CONFIDENTIAL~~

UNIVERSITY OF MICHIGAN

2260-1-T

The results obtained for the $\beta = 90^\circ$ case were

$$\sigma \approx 2.4 \times 10^3 \text{ square meters at } \lambda = 91.4 \text{ cm,}$$

and

$$\sigma \approx 1.3 \times 10^3 \text{ square meters at } \lambda = 4.57 \text{ m.}$$

Examination of the eight figures shows that the results obtained for the two methods are in good agreement.

III

THEORETICAL CROSS-SECTIONS OF B-52 AIRCRAFT3.1 METHOD

The method employed for the theoretical computations of the cross-sections of the B-52 is the same as that employed for the B-47 except that three different breakdowns were used for the B-52 rather than two as in the B-47 computations. The results obtained by the three methods for the cross-section of a B-52 are presented in the same manner as for the B-47.

3.2 X-BAND AND S-BAND CROSS-SECTIONS

All of the data obtained for the B-52 at X- and S-band by Methods I and II are summarized in Figures 3.2-1 through 3.2-5, except for the results obtained for $\beta = 90^\circ$. The results obtained for $\beta = 90^\circ$ were

$$\sigma \approx 8 \times 10^3 \text{ square meters for } \lambda = 3.05 \text{ cm and } \lambda = 9.14 \text{ cm,}$$
$$\sigma \approx 9 \times 10^3 \text{ square meters for } \lambda = 12.2 \text{ cm.}$$

The agreement between the results obtained is fairly good (to within a factor of 5 or less) except at the sharp peaks and for the following regions in β and γ where, in some cases, the results differ by a factor of 10 or more:

For $\beta = -4^\circ$, at $\gamma \approx 0^\circ$ and in the region $100^\circ < \gamma < 180^\circ$;

For $0^\circ \leq \beta \leq 30^\circ$ in the region $100^\circ < \gamma < 180^\circ$; and

For $\beta = 60^\circ$ in the regions $0^\circ \leq \gamma < 20^\circ$, $40^\circ < \gamma < 80^\circ$; and $100^\circ < \gamma < 180^\circ$.

No additional information could be gained by including the results of Method III on these figures and thus only the results from the first two methods have been graphed. It should be pointed out, however, that the results obtained by Method III were in good agreement with the data shown on Figures 3.2-1 through 3.2-5.

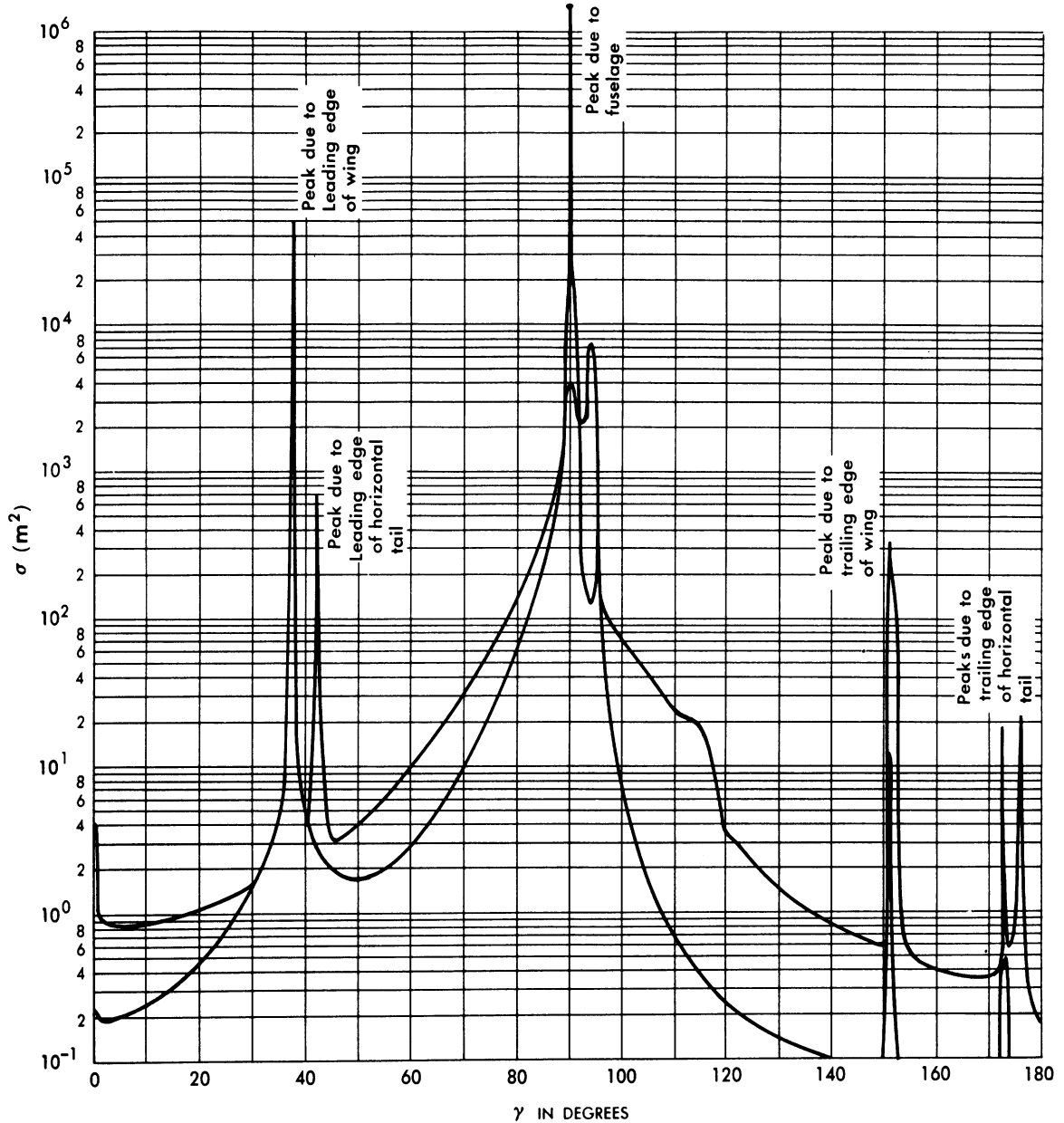


FIG. 3.2-1 CROSS-SECTION OF A B-52 AT X-AND S-BAND FREQUENCIES FOR $\beta = -4^\circ$ (Largest and Smallest Values Computed for $\lambda = 3$ cm, 9 cm and 12 cm)

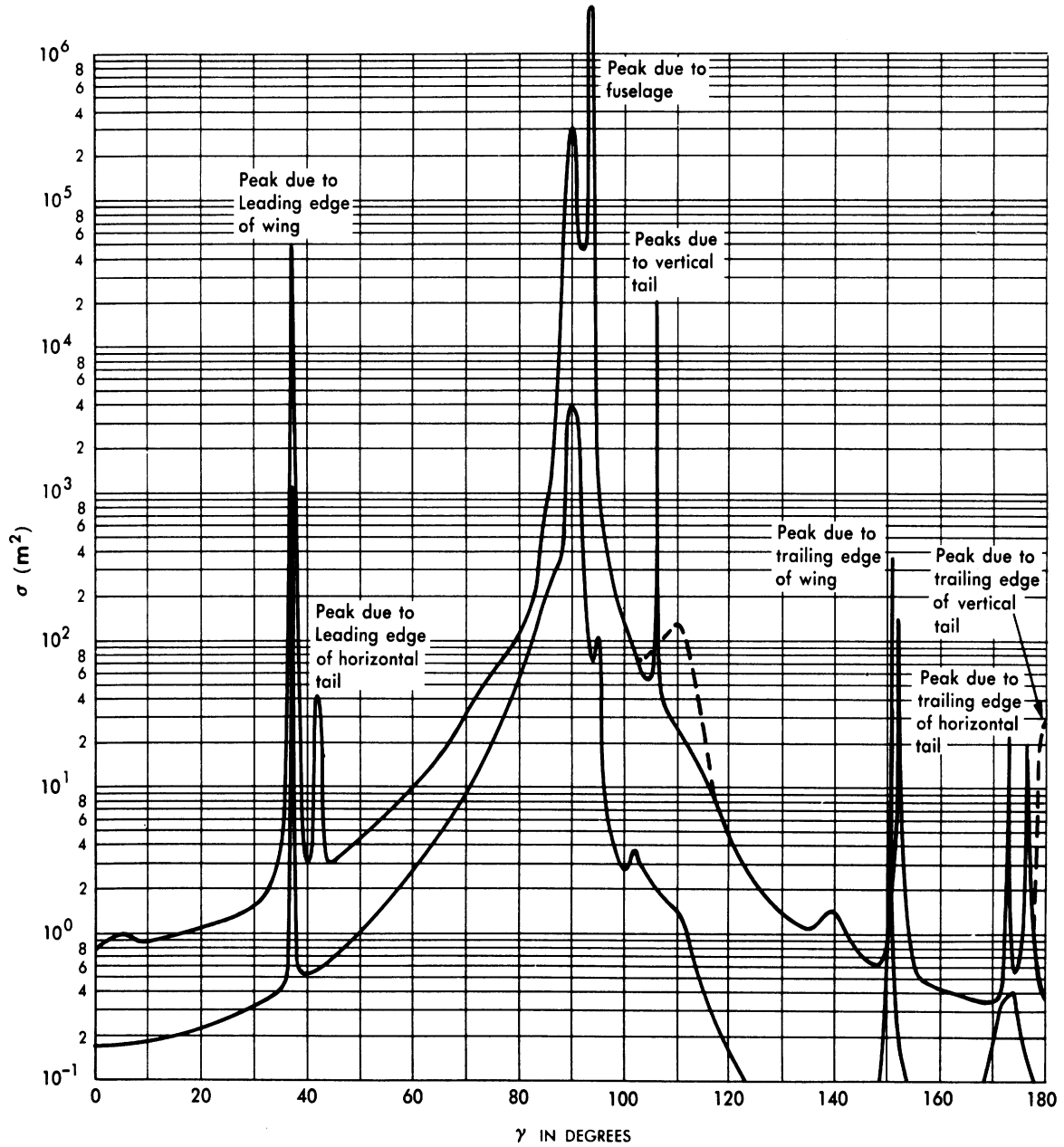


FIG. 3.2-2 CROSS-SECTION OF A B-52 AT X-AND S-BAND FREQUENCIES FOR $0^\circ \leq \beta \leq 4^\circ$ (Largest and Smallest Values Computed for $\beta = 0^\circ$ and 4° and $\lambda = 3\text{ cm}, 9\text{ cm}$ and 12 cm)

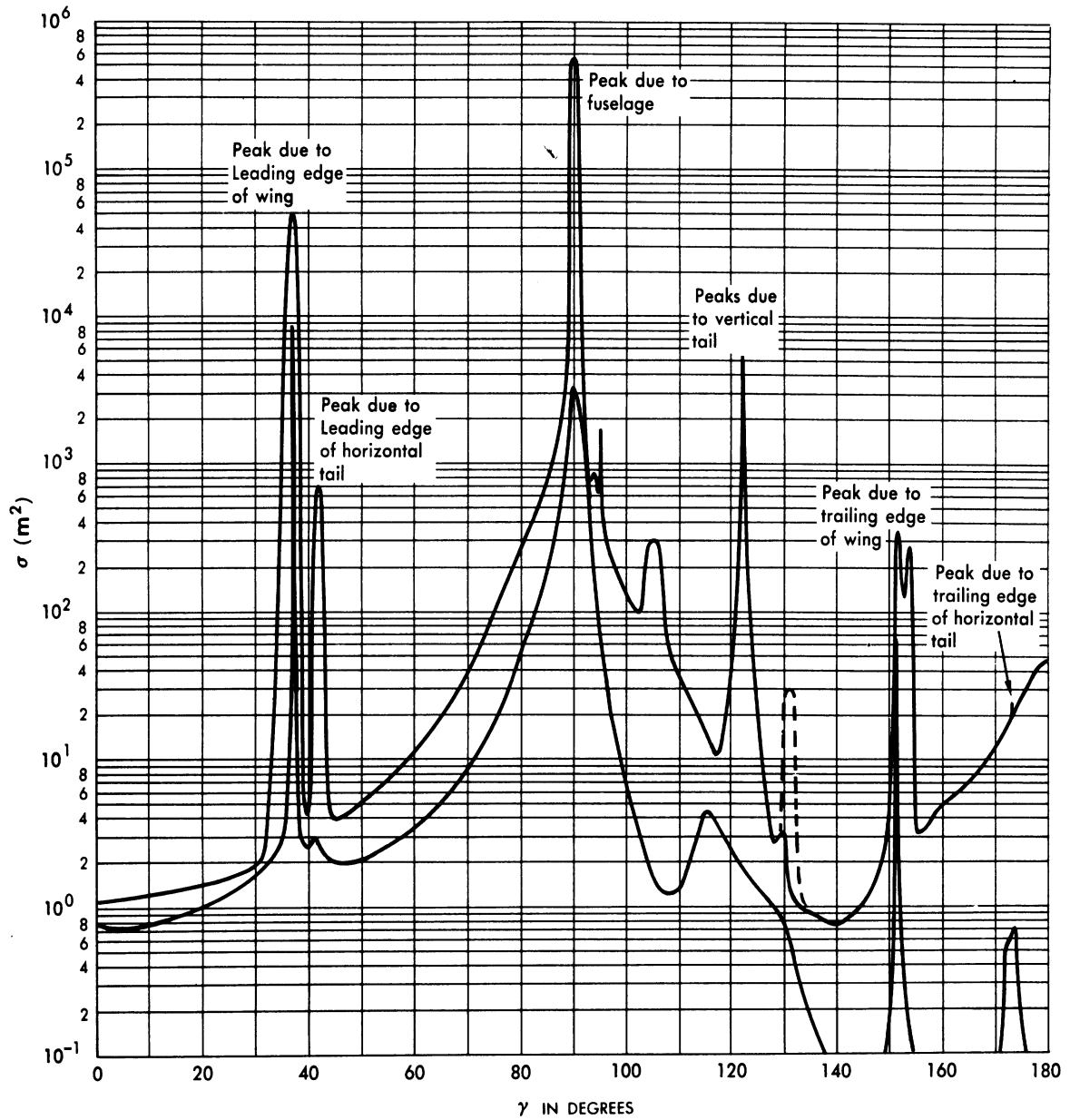


FIG. 3.2-3 CROSS-SECTION OF A B-52 AT X-AND S-BAND FREQUENCIES FOR $8^\circ \leq \beta \leq 12^\circ$ (Largest and Smallest Values Computed for $\beta=8^\circ$ and 12° and $\lambda=3\text{cm}, 9\text{cm}$ and 12cm)

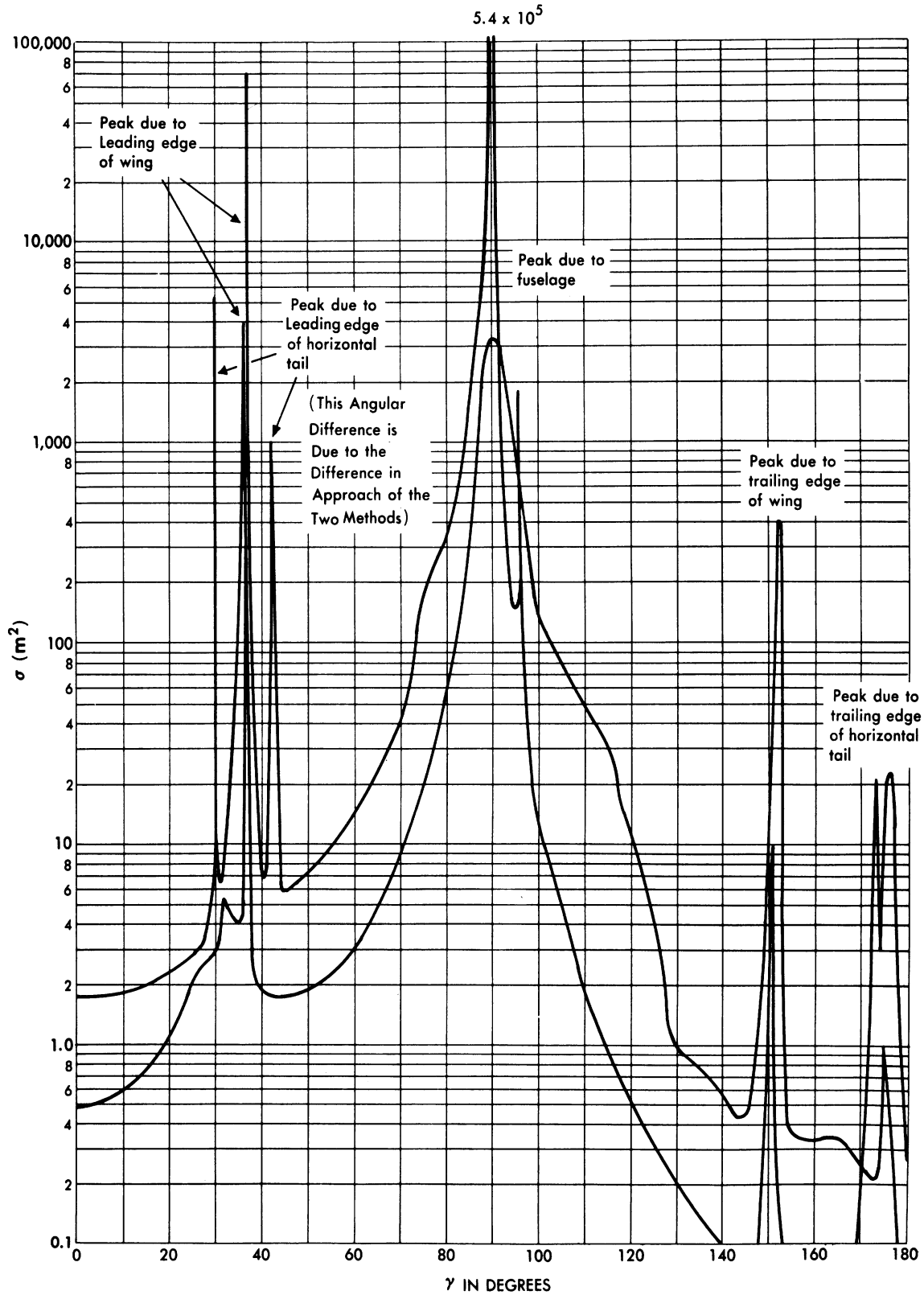


FIG. 3.2-4 CROSS-SECTION OF A B-52 AT X-AND S-BAND FREQUENCIES FOR $\beta = 30^\circ$ (Largest and Smallest Values Computed for $\lambda = 3$ cm, 9 cm and 12 cm)

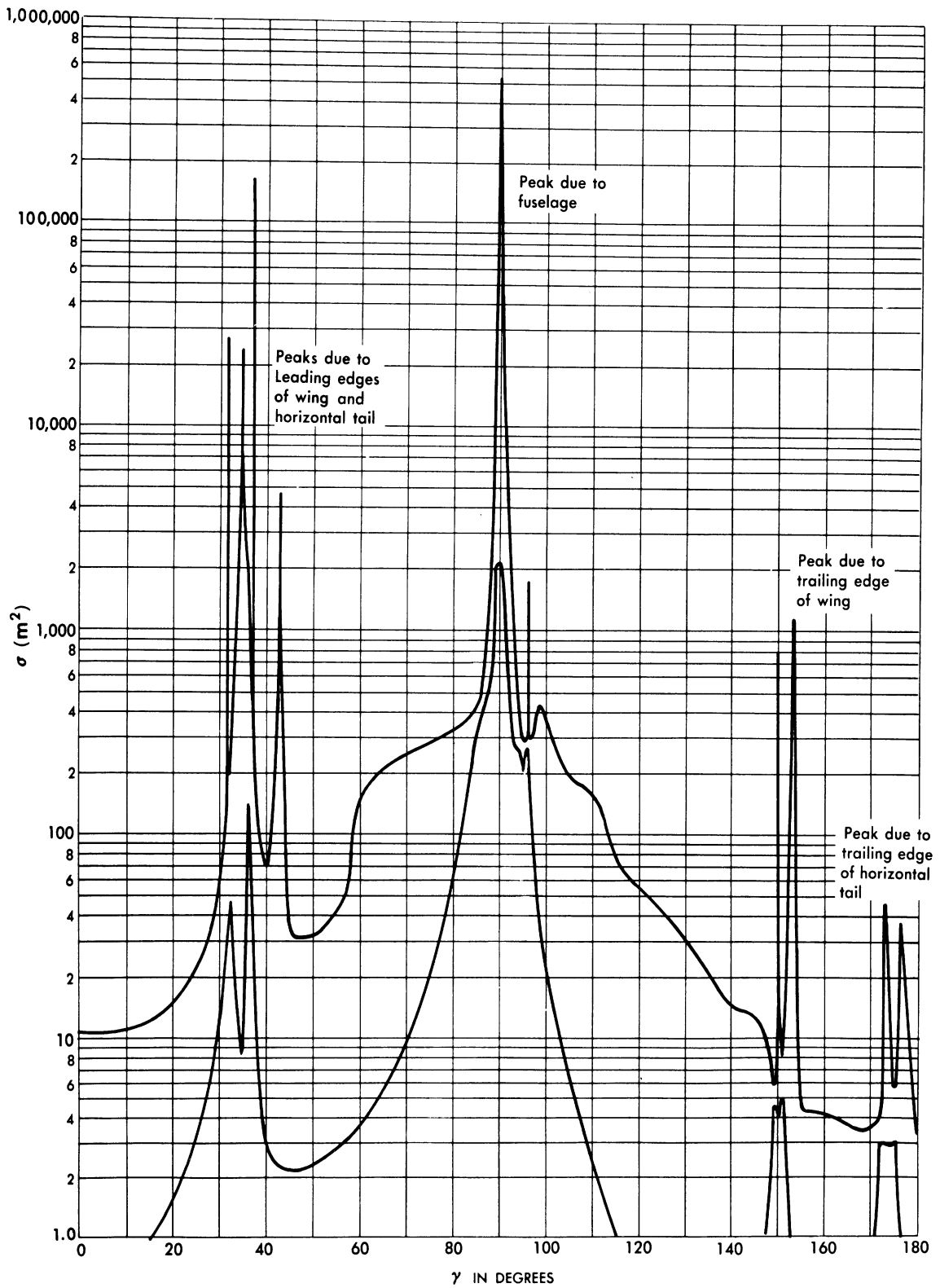


FIG. 3.2-5 CROSS-SECTION OF A B-52 AT X-AND S-BAND FREQUENCIES FOR $\beta=60^\circ$ (Largest and Smallest Values Computed for $\lambda = 3 \text{ cm}, 9 \text{ cm}$ and 12 cm)

3.3 L-BAND CROSS-SECTIONS

The B-52 cross-sections computed by Methods I and II at the L-band wavelengths of $\lambda = 18.3$ cm and $\lambda = 30.5$ cm are summarized in Figures 3.3-1 through 3.3-5¹. It is seen that the results obtained by the two methods are in reasonable agreement. In general, the comments made in Section 3.2 relative to the X- and S-band results hold also for the L-band computations.

The results obtained for the $\beta = 90^\circ$ cases are:

$$\sigma \approx 1.3 \times 10^4 \text{ square meters for } \lambda = 18.3 \text{ cm}$$

$$\sigma \approx 2 \times 10^4 \text{ square meters for } \lambda = 30.5 \text{ cm.}$$

3.4 CROSS-SECTIONS FOR $\lambda = 91.4$ cm AND $\lambda = 4.57$ m

The cross-sections computed for the B-52 at the long wavelengths of $\lambda = 91.4$ cm and $\lambda = 4.57$ m are summarized in Figures 3.4-1 through 3.4-12. Only the 91.4 cm case was computed by Method I and then only for $\beta = -4^\circ, 12^\circ, \text{ and } 60^\circ$. All eight β values were computed for both wavelengths by Methods II and III.

Figure 3.4-1 summarizes the $-4^\circ \leq \beta \leq +4^\circ$ data for $\lambda = 91.4$ cm; Figure 3.4-2 presents the Methods II and III results for $\beta = 8^\circ$ and $\lambda = 91.4$ cm; Figure 3.4-3 compares the results obtained by the three methods for the $\beta = 12^\circ, \lambda = 91.4$ cm case; Figure 3.4-4 presents the Methods II and III results for the $\beta = 30^\circ$ and $\lambda = 91.4$ cm case; and Figure 3.4-5 compares the results from the three methods for the $\beta = 60^\circ$ and $\lambda = 91.4$ cm case.

The results obtained by Methods II and III for the $\lambda = 4.57$ m case are presented in Figures 3.4-6 through 3.4-12. ($\beta = -4^\circ, 0^\circ, 4^\circ, 8^\circ, 12^\circ, 30^\circ, \text{ and } 60^\circ$.)

¹As in the preceding section the Method III results are not included on the graphs; the Method III results were compatible with the data shown on Figures 3.3-1 through 3.3-5.

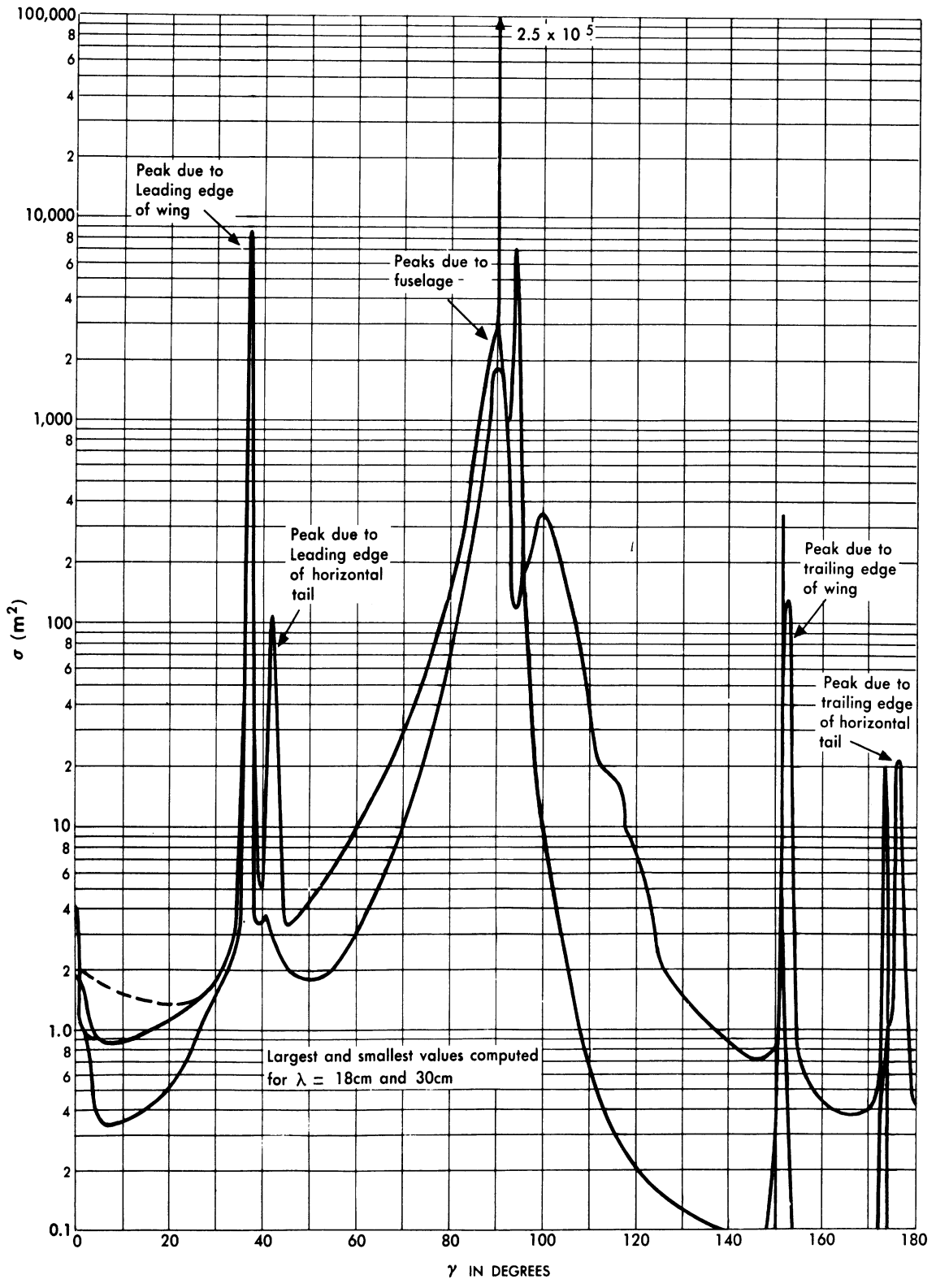


FIG. 3.3-1 CROSS-SECTION OF A B-52 AT L BAND FREQUENCIES
FOR $\beta = -4^\circ$

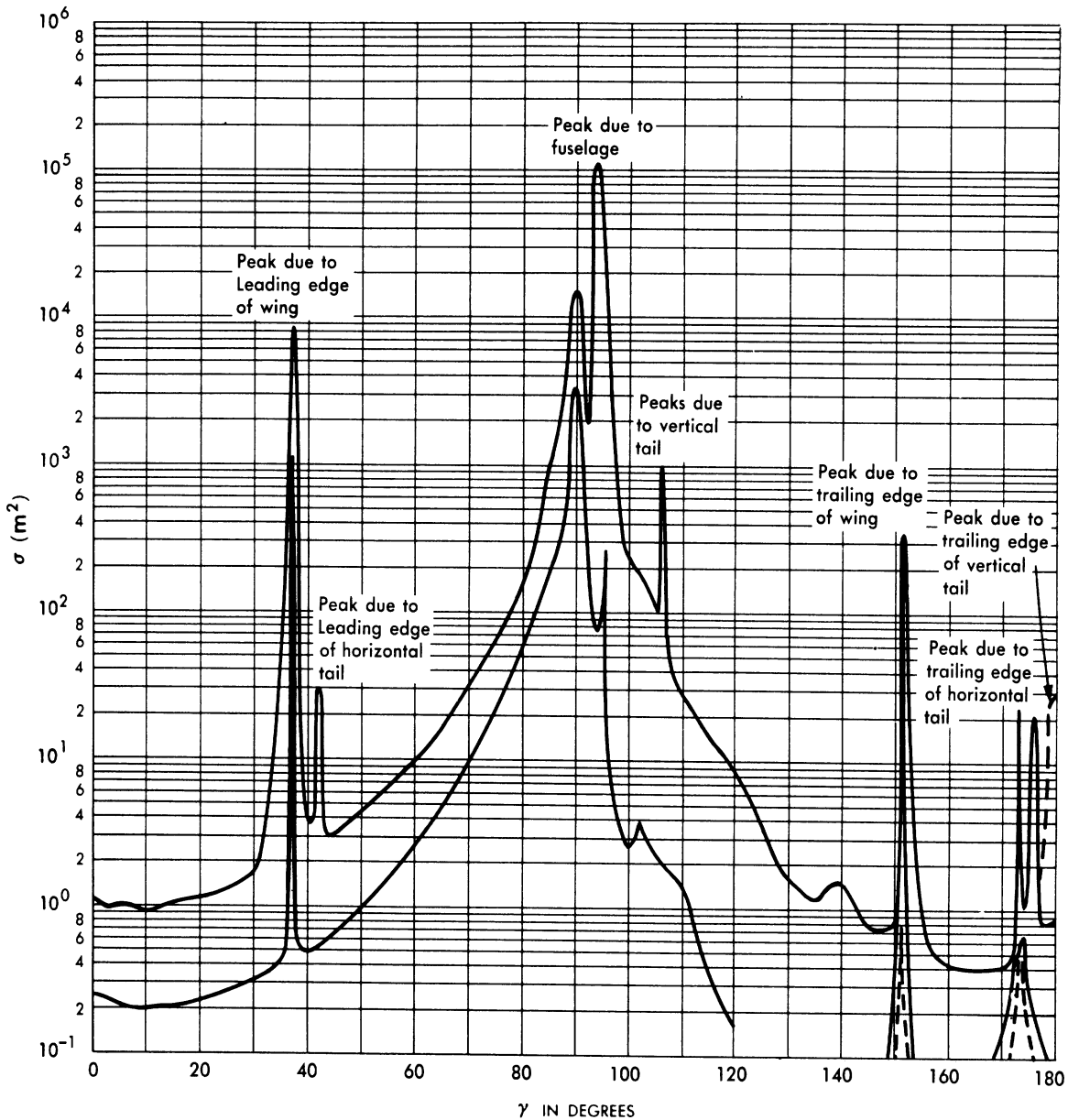


FIG. 3.3-2 CROSS-SECTION OF A B-52 AT L-BAND FREQUENCIES
FOR $0^\circ \leq \beta \leq 4^\circ$ (Largest and Smallest Values Computed
for $\beta = 0^\circ$ and 4° and $\lambda = 18$ cm and 30 cm)

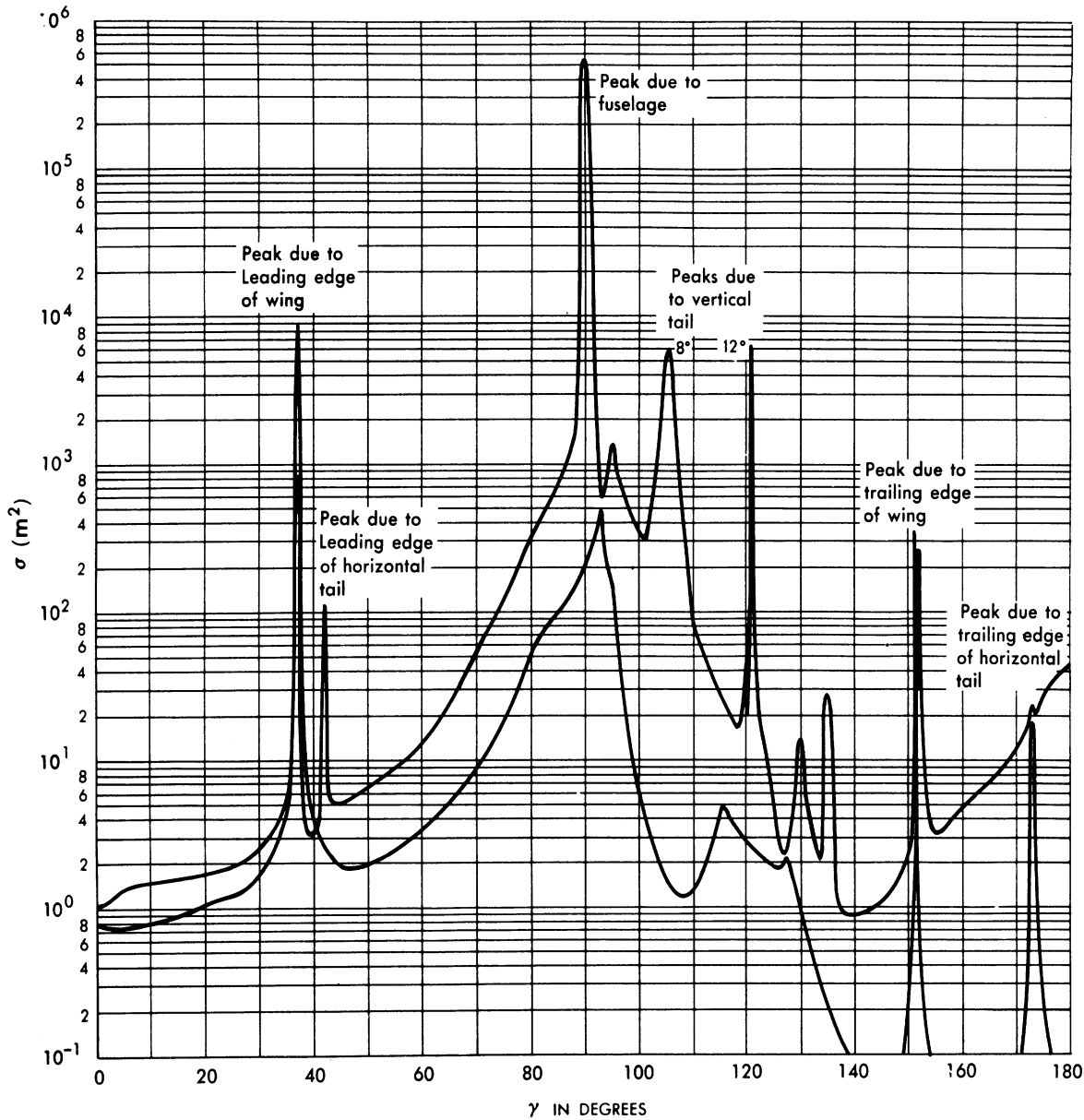


FIG. 3.3-3 CROSS-SECTION OF A B-52 AT L-BAND FREQUENCIES
FOR $8^\circ \leq \beta \leq 12^\circ$ (Largest and Smallest Values Computed
for $\beta = 8^\circ$ and 12° and $\lambda = 18\text{cm}$ and 30cm)

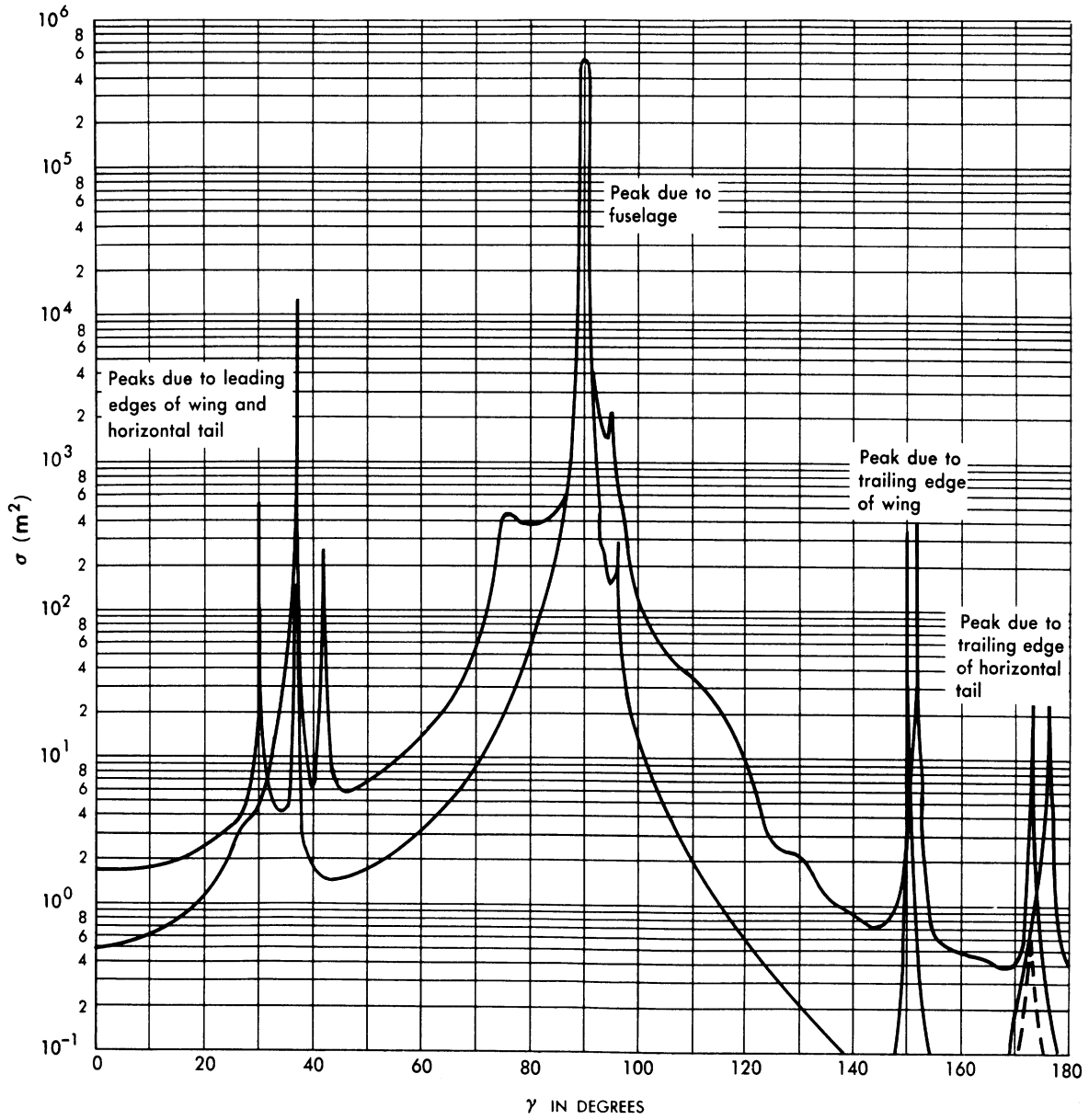


FIG. 3.3-4 CROSS-SECTION OF A B-52 AT L-BAND FREQUENCIES FOR $\beta = 30^\circ$
(Largest and Smallest Values Computed for $\lambda = 18$ cm. and 30 cm.)

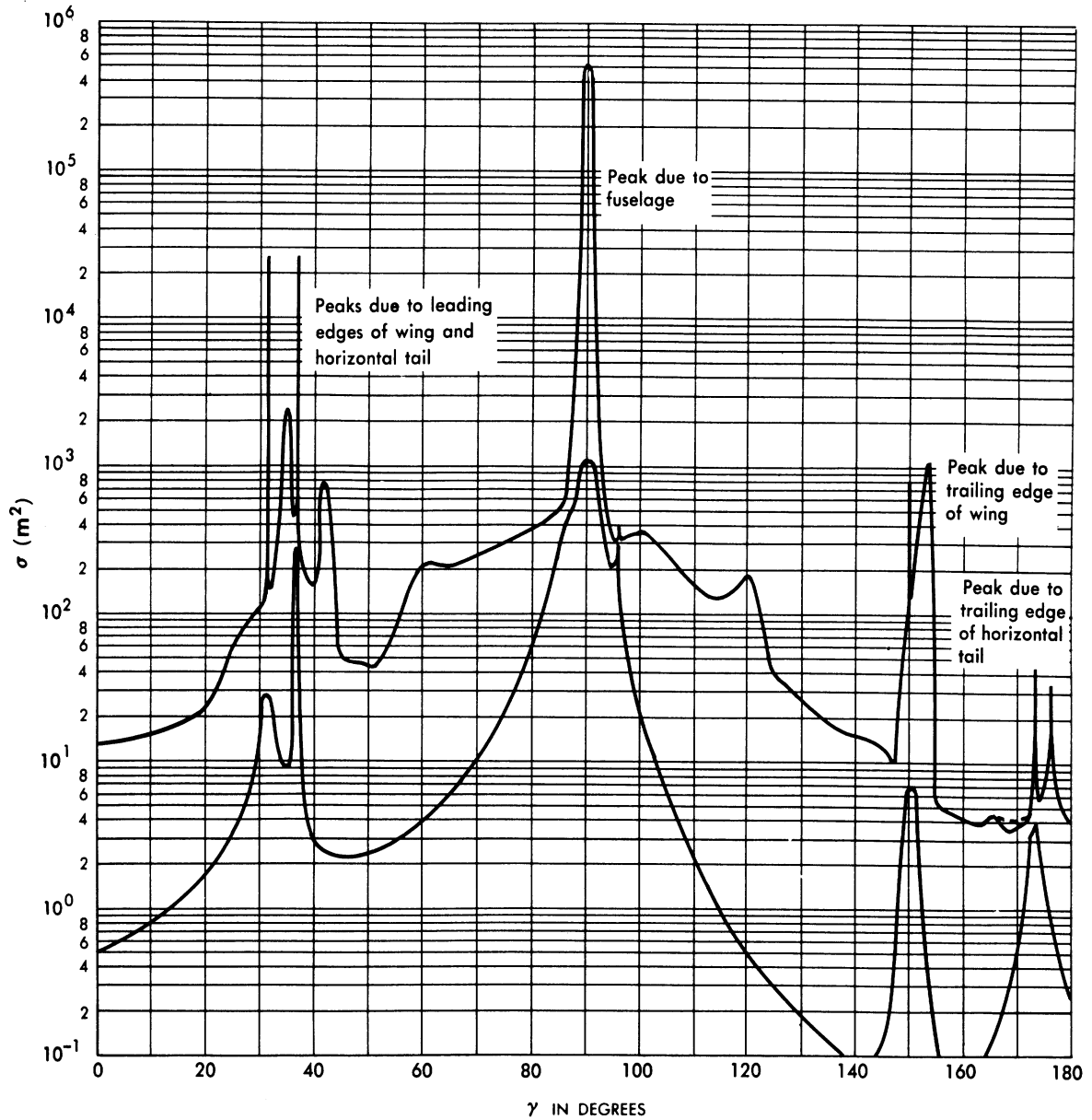


FIG. 3.3-5 CROSS-SECTION OF A B-52 AT L-BAND FREQUENCIES FOR $\beta = 60^\circ$
(Largest and Smallest Values Computed for $\lambda = 18$ cm. and 30 cm.)

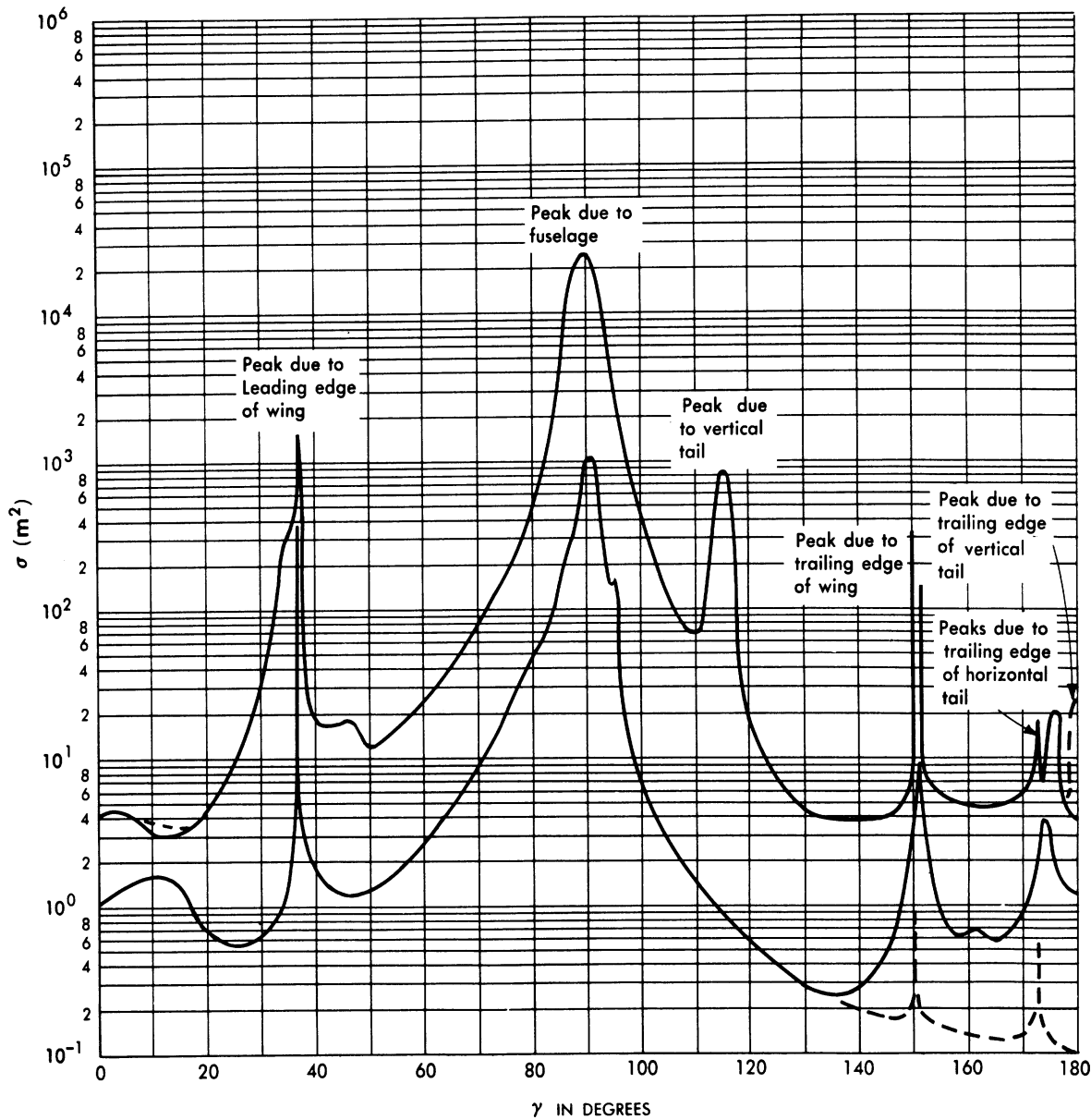


FIG. 3.4-1 CROSS-SECTION OF A B-52 FOR $\lambda = 91.4$ cm. AND $-4^\circ \leq \beta \leq 4^\circ$
(Largest and Smallest Values Computed)

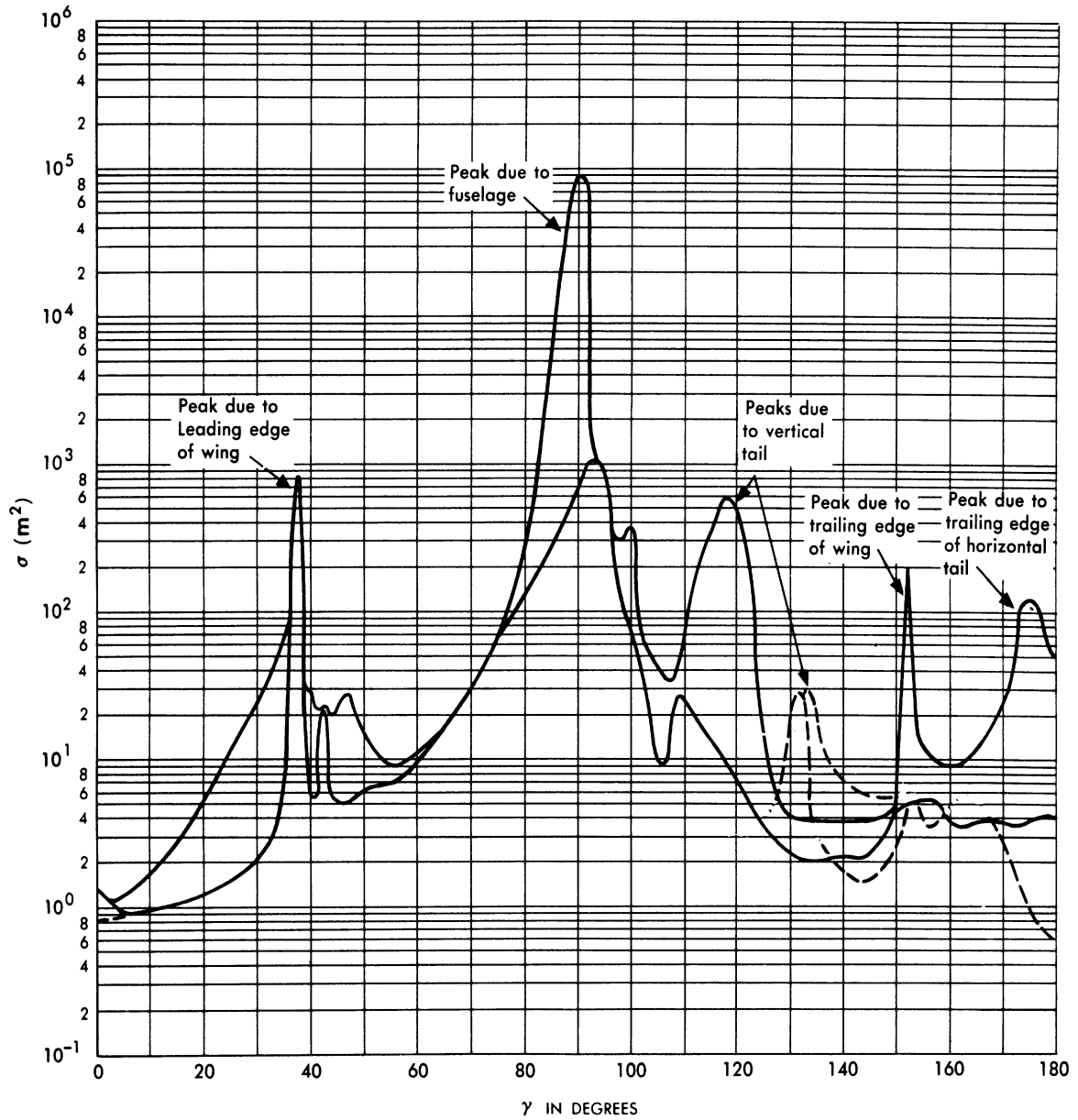


FIG. 3.4-2 CROSS-SECTION OF A B-52 FOR $\beta = 8^\circ$ AND $\lambda = 91.4$ cm.
(Largest and Smallest Values Computed)

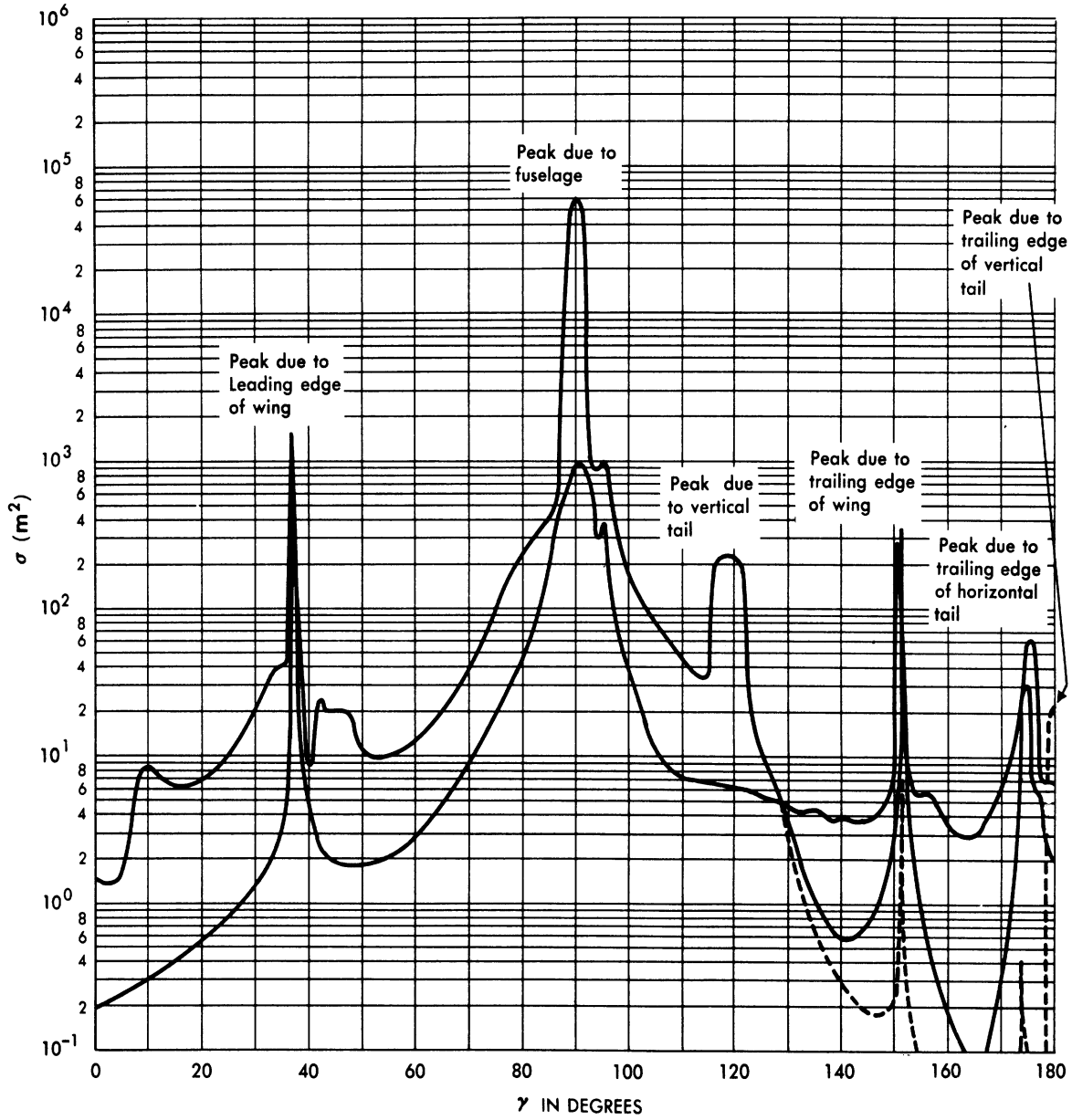


FIG. 3.4 - 3 CROSS-SECTION OF A B-52 FOR $\beta = 12^\circ$ AND $\lambda = 91.4$ cm.
(Largest and Smallest Values Computed)

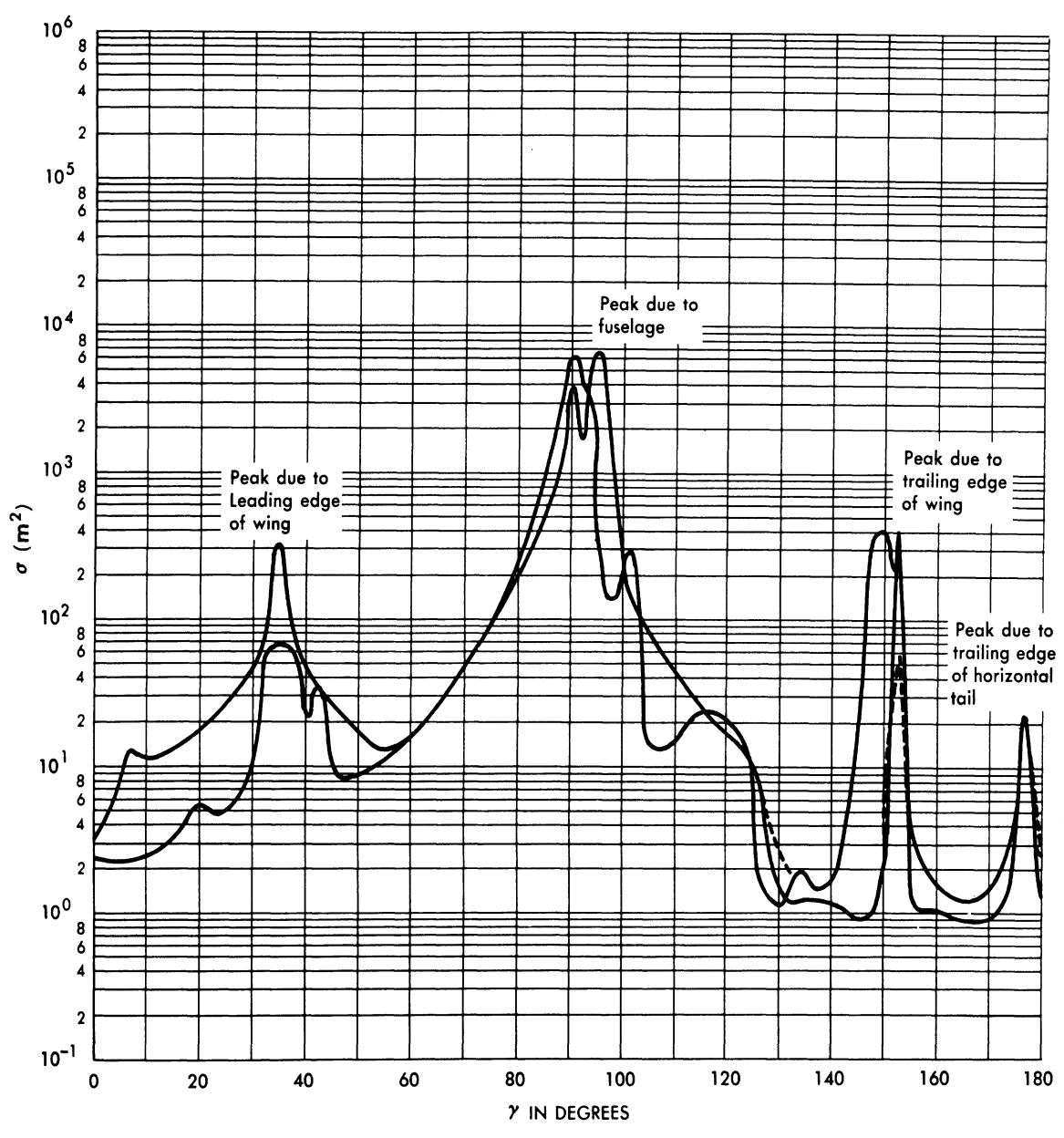


FIG. 3.4 - 4 CROSS-SECTION OF A B-52 FOR $\beta = 30^\circ$ AND $\lambda = 91.4$ m.
(Largest and Smallest Values Computed)

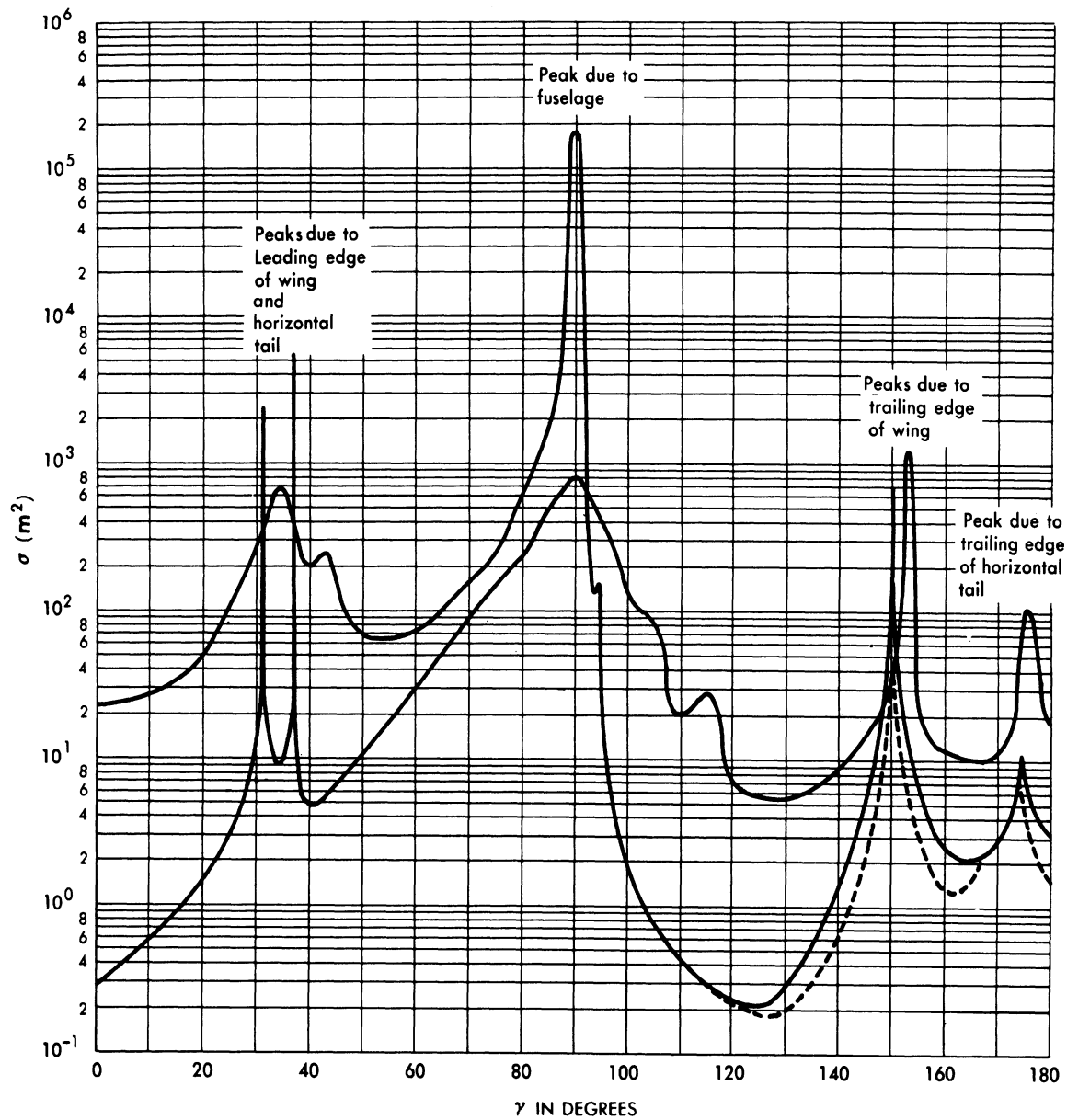


FIG. 3.4-5 CROSS-SECTION OF A B-52 FOR $\beta = 60^\circ$ AND $\lambda = 91.4$ m.
(Largest and Smallest Values Computed)

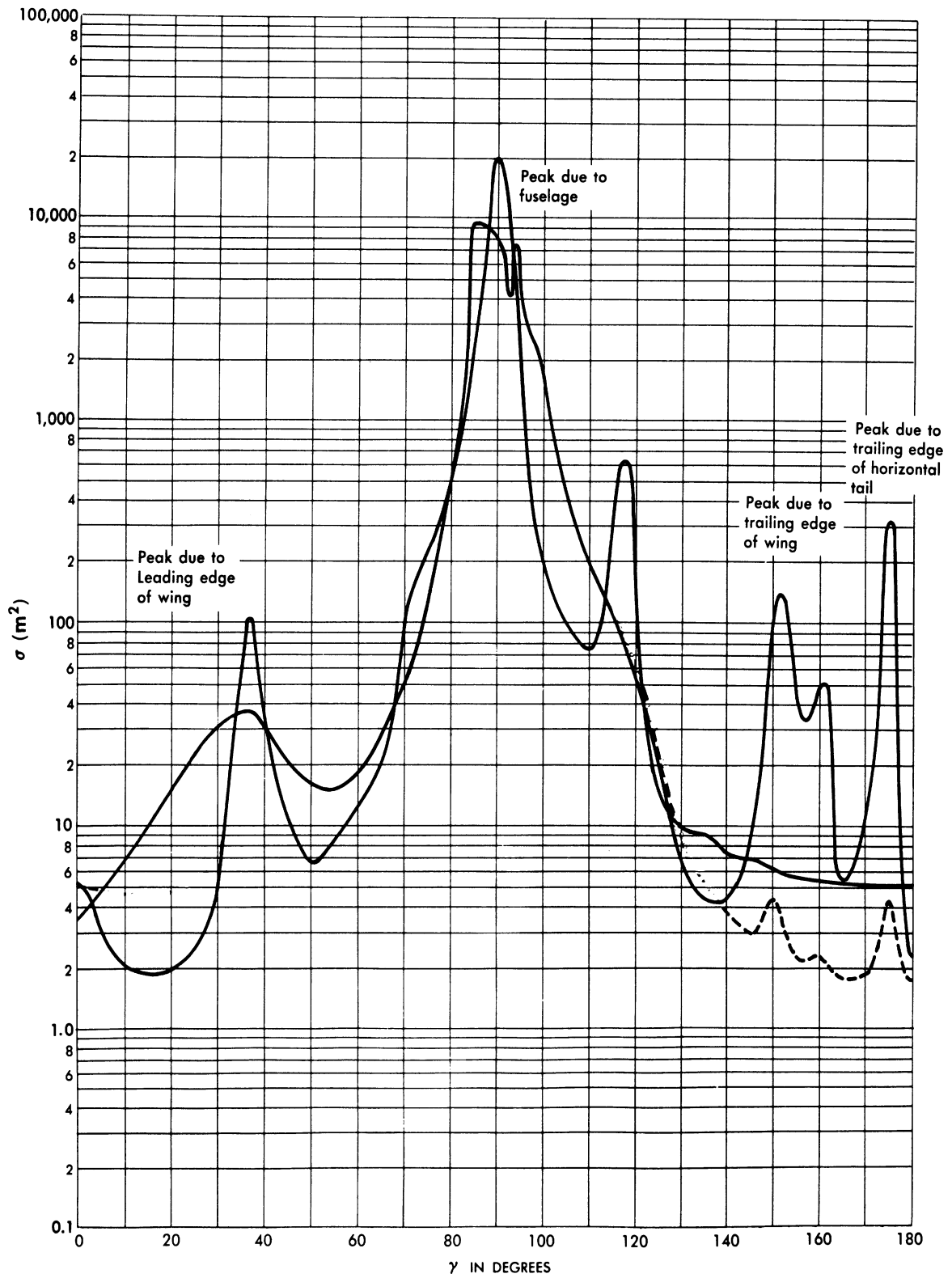


FIG. 3.4-6 CROSS-SECTION OF A B-52 FOR $\beta = -4^\circ$ AND $\lambda = 4.57 m$.
(Largest and Smallest Values Computed)

~~CONFIDENTIAL~~

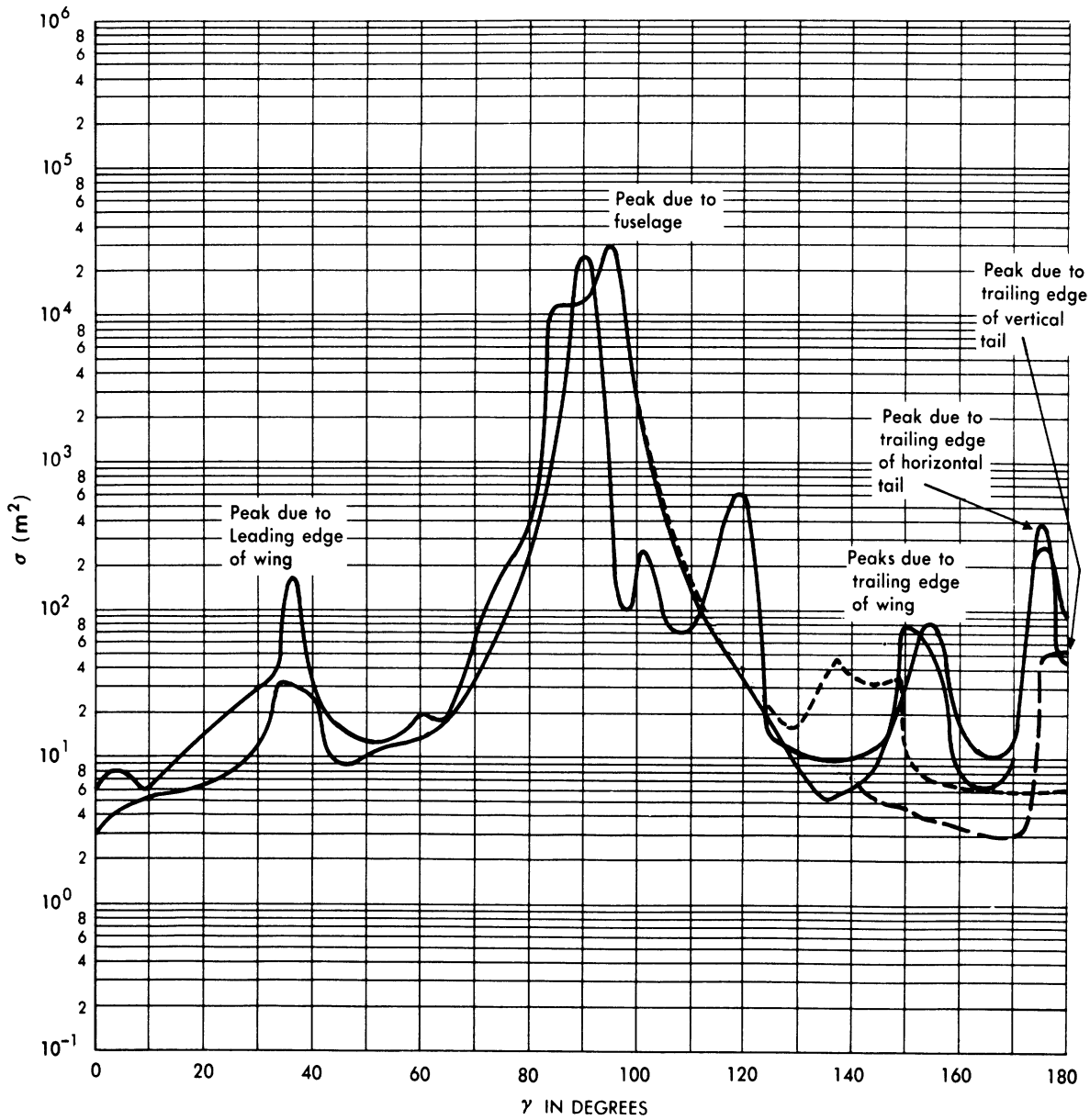


FIG. 3.4-7 CROSS-SECTION OF A B-52 FOR $\beta = 0^\circ$ AND $\lambda = 4.57$ m.
(Largest and Smallest Values Computed)

~~CONFIDENTIAL~~

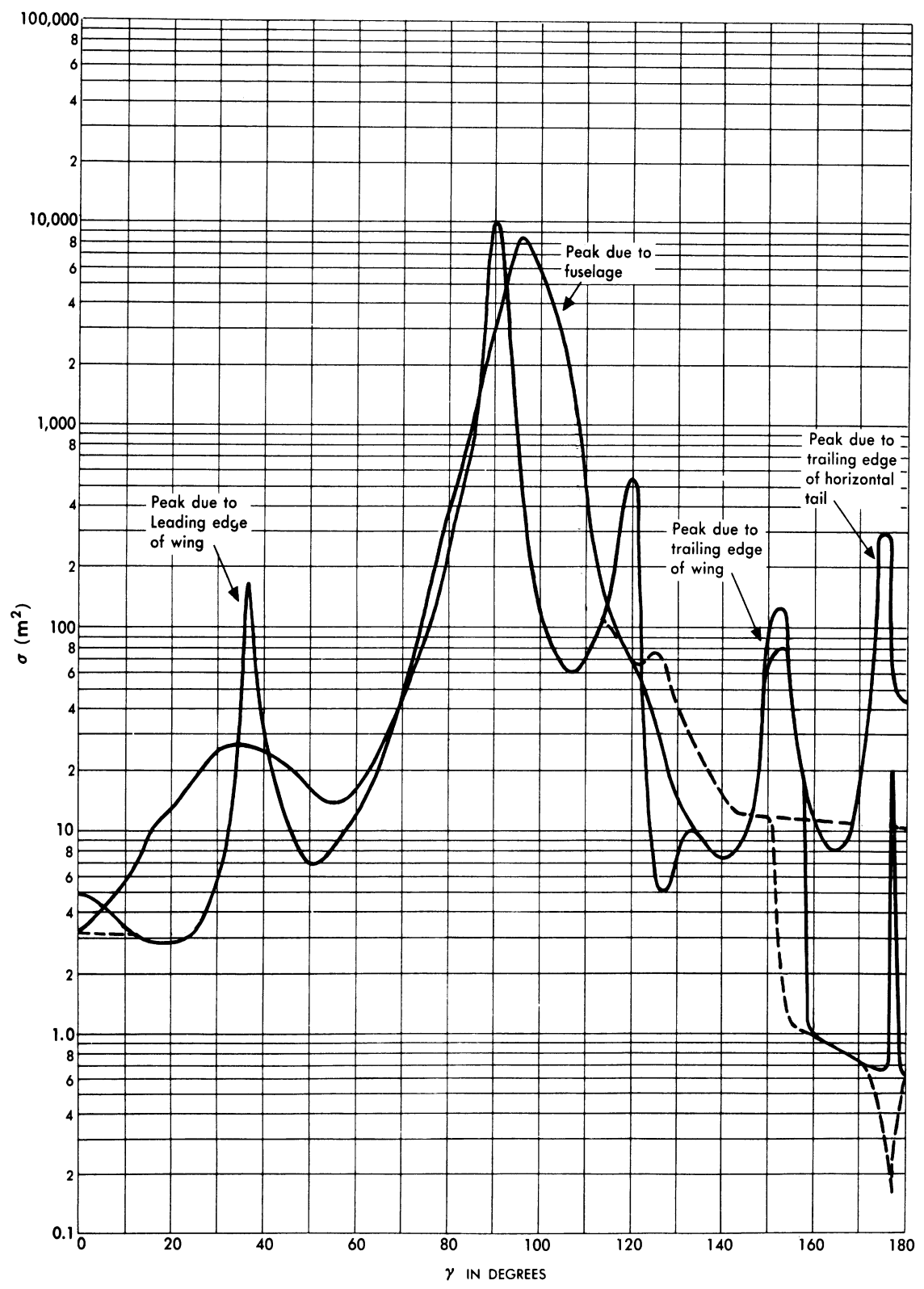


FIG. 3.4-8 CROSS-SECTION OF A B-52 FOR $\beta=4^\circ$ AND $\lambda=4.57$ m.
(Largest and Smallest Values Computed)

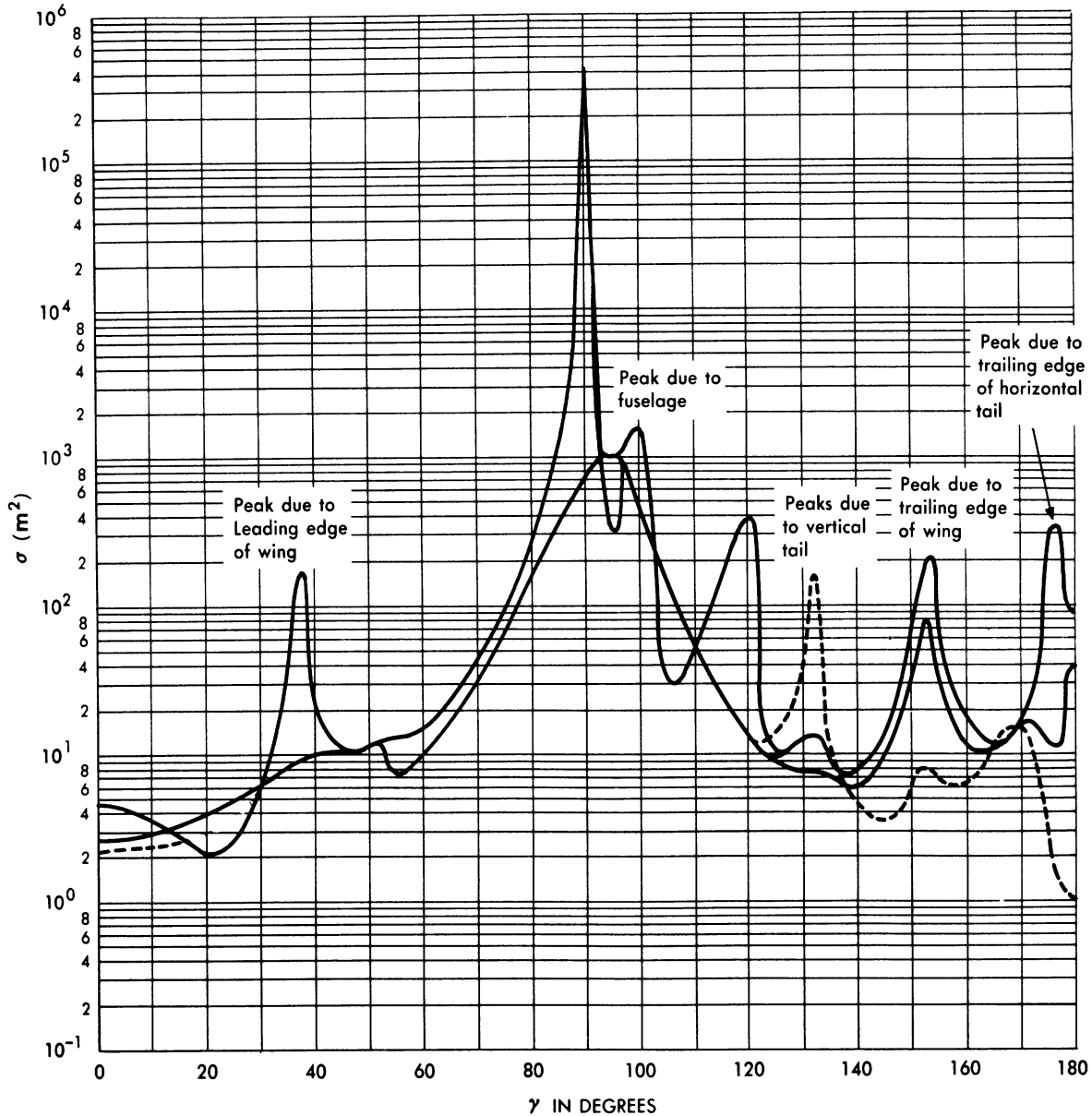


FIG. 3.4 - 9 CROSS-SECTION OF A B-52 FOR $\beta = 8^\circ$ AND $\lambda = 4.57$ m.
(Largest and Smallest Values Computed)

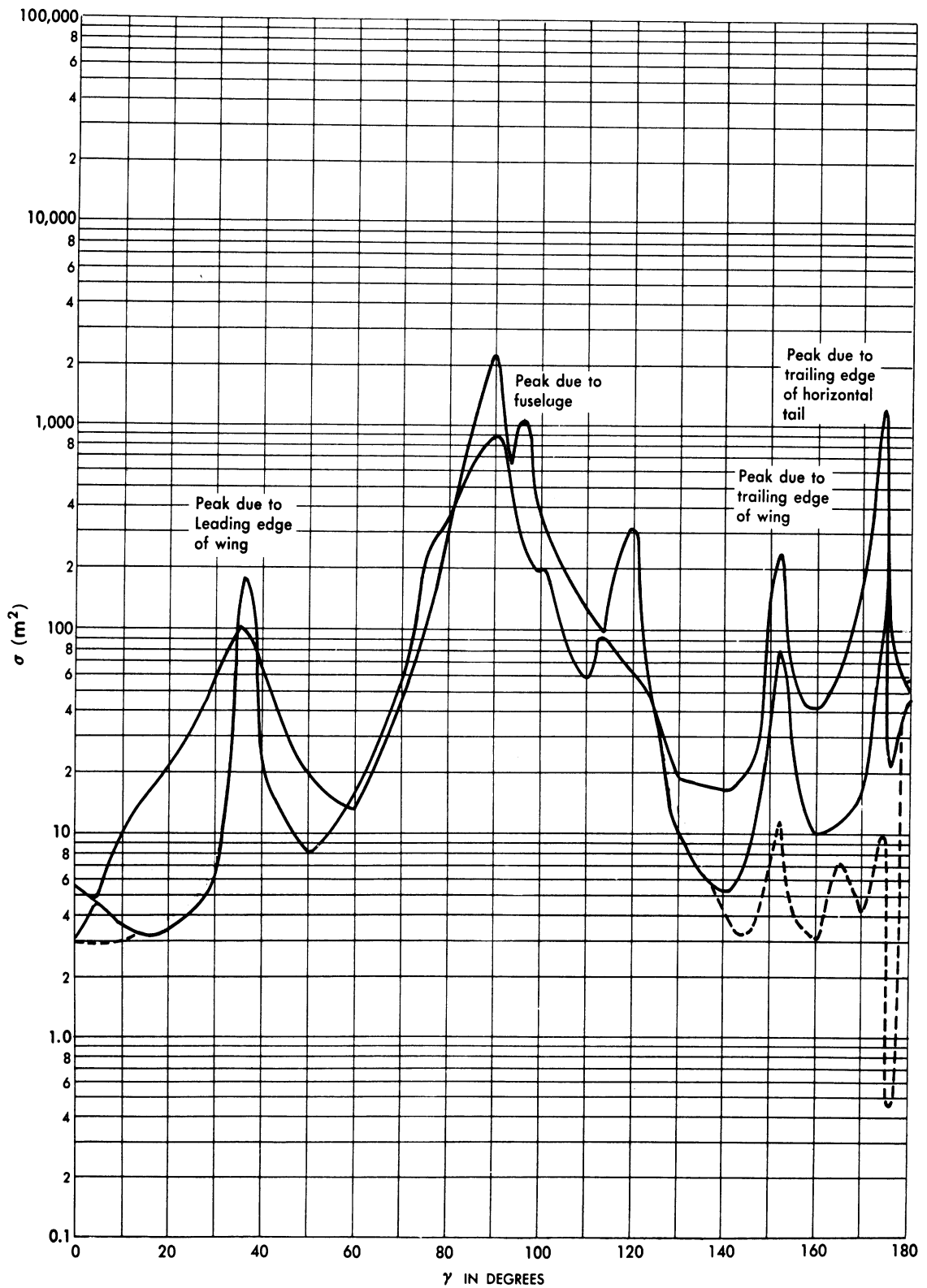


FIG. 3.4--10 CROSS-SECTION OF A B-52 FOR $\beta = 12^\circ$ AND $\lambda = 4.57$ m
(Largest and Smallest Values Computed)

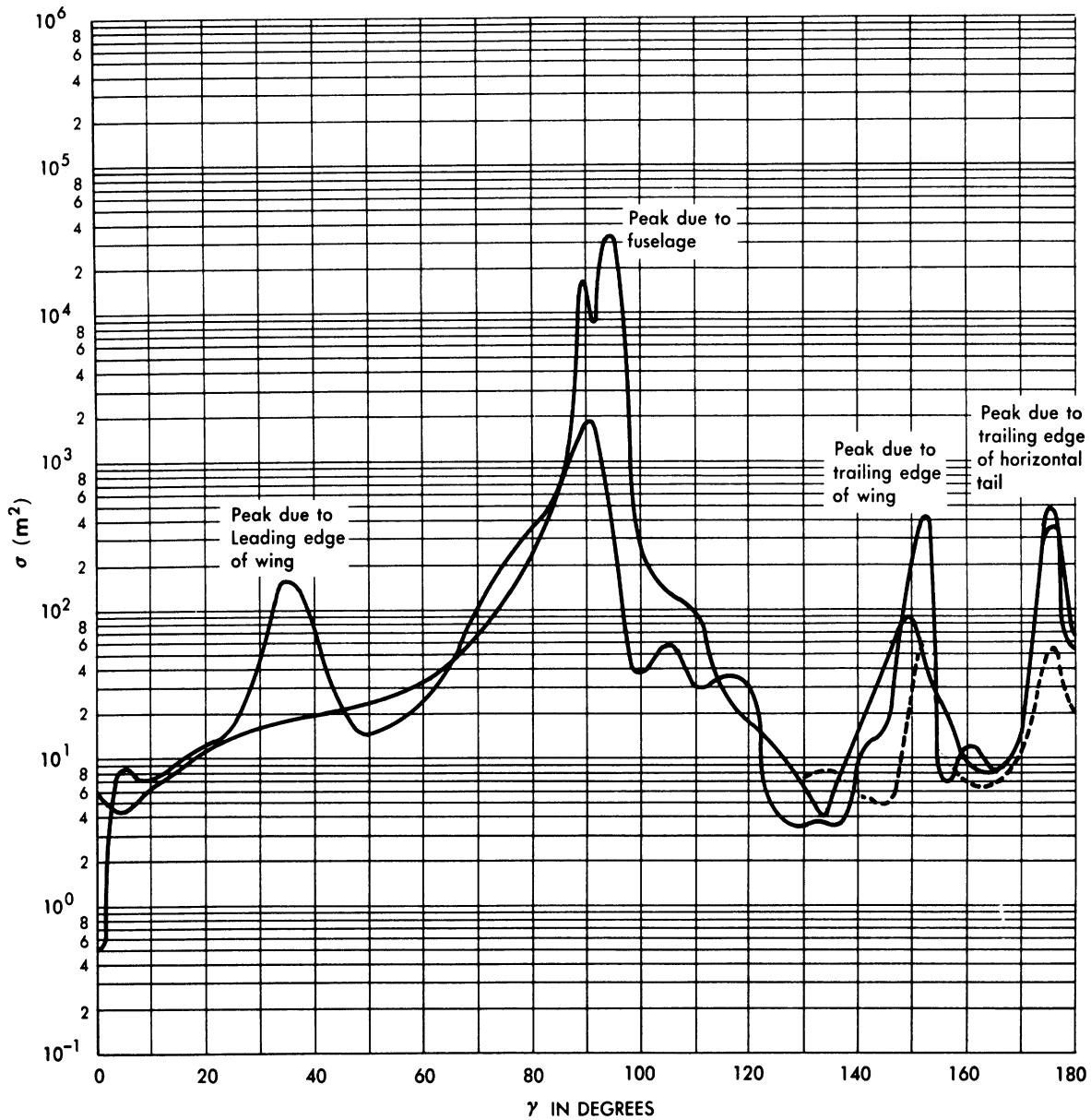


FIG. 3.4 - 11 CROSS-SECTION OF A B-52 FOR $\beta = 30^\circ$ AND $\lambda = 4.57$ m.
(Largest and Smallest Values Computed)

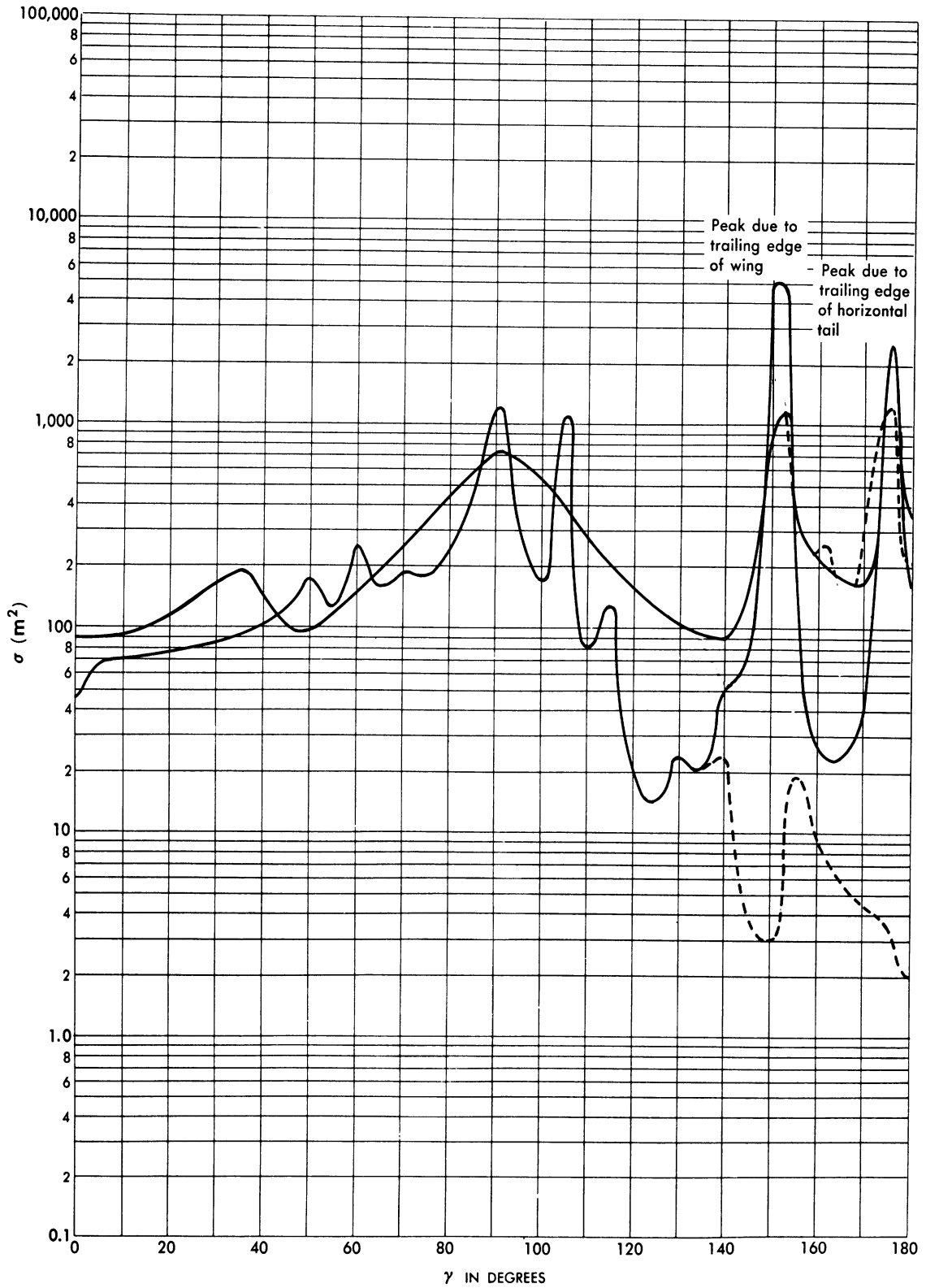


FIG. 3.4 - 12 CROSS-SECTION OF A B-52 FOR $\beta=60^\circ$ AND $\lambda=4.57$ m.
(Largest and Smallest Values Computed)

UNIVERSITY OF MICHIGAN
2260-1-T

The results obtained for the $\beta = 90^\circ$ cases are:

$$\sigma \approx 1 \times 10^4 \text{ square meters for } \lambda = 91.4 \text{ cm}$$

$$\sigma \approx 1 \times 10^5 \text{ square meters for } \lambda = 4.57 \text{ m.}$$

IV

COMPARISON BETWEEN THEORY AND EXPERIMENT

Since the authors do not know of any experimental data which exist for the B-52, this section must by necessity deal only with the B-47. Experimental data on the B-47 have been obtained by Ohio State University, the Hughes Aircraft Company, and the Aircraft Radiation Laboratory of the Wright Air Development Center.

The Ohio State experiments were made on 1/123-scale models at 9000 Mc with c-w equipment. This gave an equivalent frequency of 73 Mc for the full scale B-47. An extensive tabulation of these results appears in Reference 2; a comparison between typical Ohio State experimental data and equivalent theoretical results given in Section II is shown in Figures 4-1 and 4-2¹. Recently, unpublished results have been obtained at Ohio State University for a full scale B-47 at 73 Mc, 195 Mc, and 600 Mc. These later experiments were made with K-band pulse equipment and X-band c-w equipment (the X-band equipment is discussed in Reference 3 and the K-band equipment is discussed in Reference 4). The 1/123-scale model gave the equivalent full scale frequency of 195 Mc when measured at K-band; a 1/40-scale model was used at K-band to obtain the 600 Mc results. The 1/40-scale model did not simulate the B-47 properly as it had the wrong wing and engine structure; some of these effects were reduced by the use of "harp" cloth. Since there is a basic difference between the geometry used in the Ohio State University experiments and the geometry used in the theoretical computations discussed in Section II, a graphical description of the geometry used in the Ohio State University experiments is shown in Figure 4-3. (Comparison of this figure with Figure 2.1-1 will display the differences in geometry.) A comparison between these later Ohio State University measurements and the theoretical results of Section II is presented in Figures 4-4 through 4-12. In Figures 4-4 through 4-6, the comparison is made for $0^\circ \leq \beta \leq 180^\circ$ while

¹For simplicity in presentation the theoretical results used for comparison with experiment in this section are averages of the results obtained by Methods I and II.

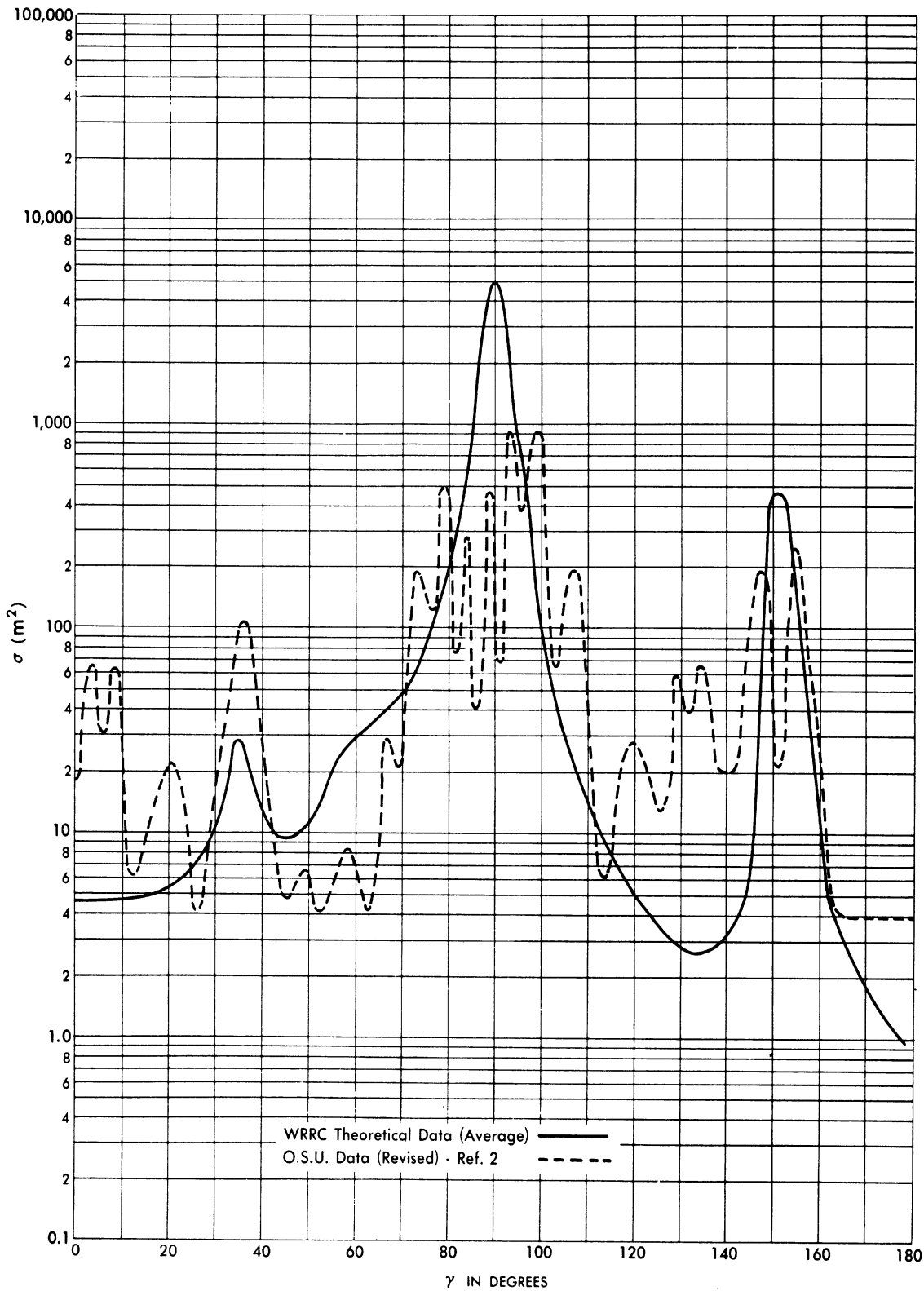


FIG. 4-1 THE B-47 - COMPARISON BETWEEN THEORY FOR $\beta=0^\circ$ AND $\lambda=4.57$ m AND REVISED O.S.U. EXPERIMENTAL DATA FOR $\beta=0^\circ$ AND $\lambda=4.11$ m. (Horizontal Polarization)

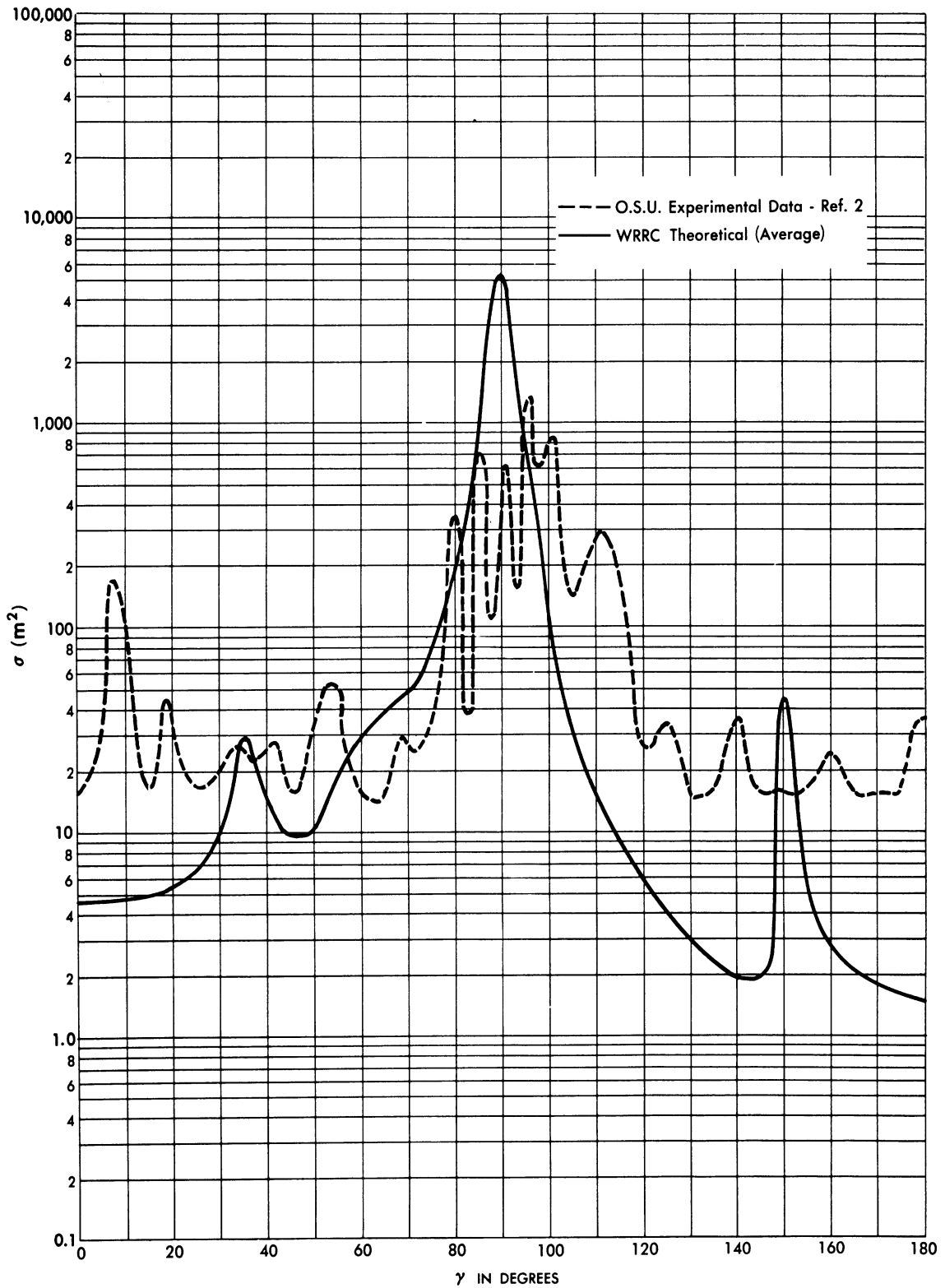


FIG. 4-2 THE B-47 - COMPARISON BETWEEN THEORY FOR $\beta=0^\circ$ AND $\lambda=4.57$ m AND O.S.U. EXPERIMENTAL DATA FOR $\beta=0^\circ$ AND $\lambda=4.11$ m (Vertical Polarization)

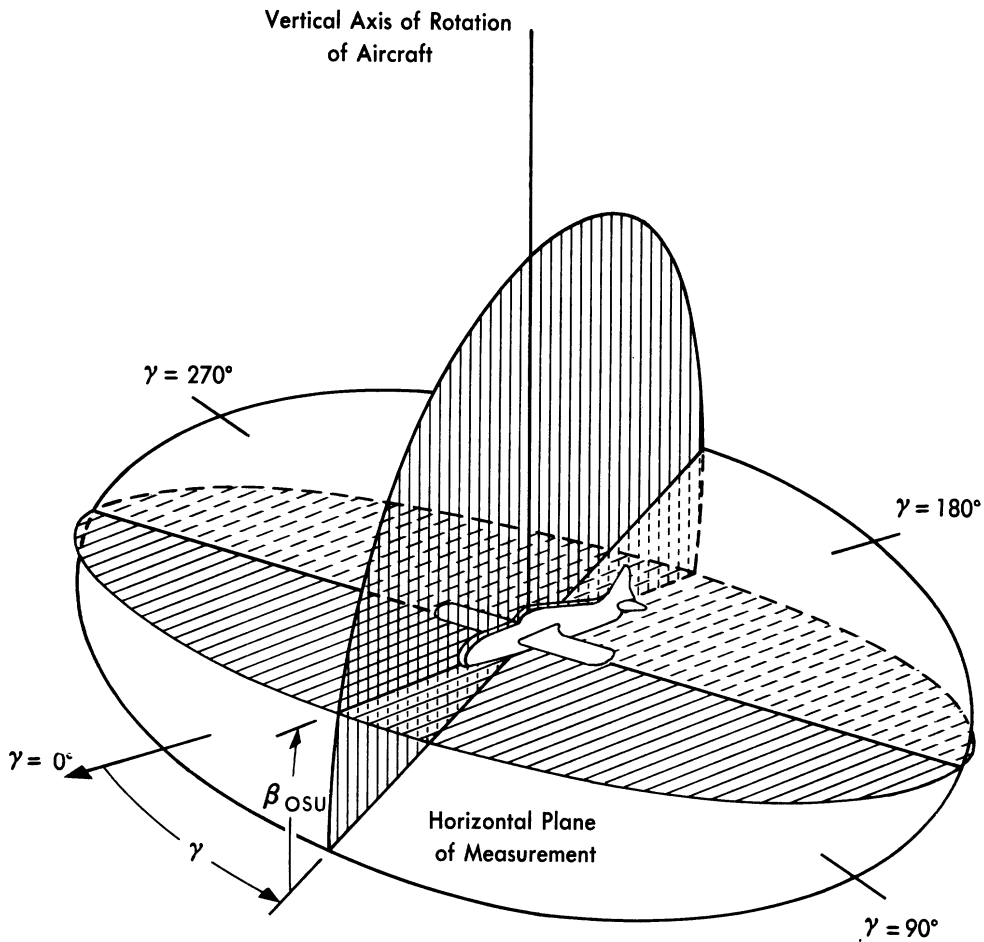


FIG. 4-3 COORDINATE SYSTEM USED IN THE OHIO STATE BACK SCATTERING EXPERIMENTS

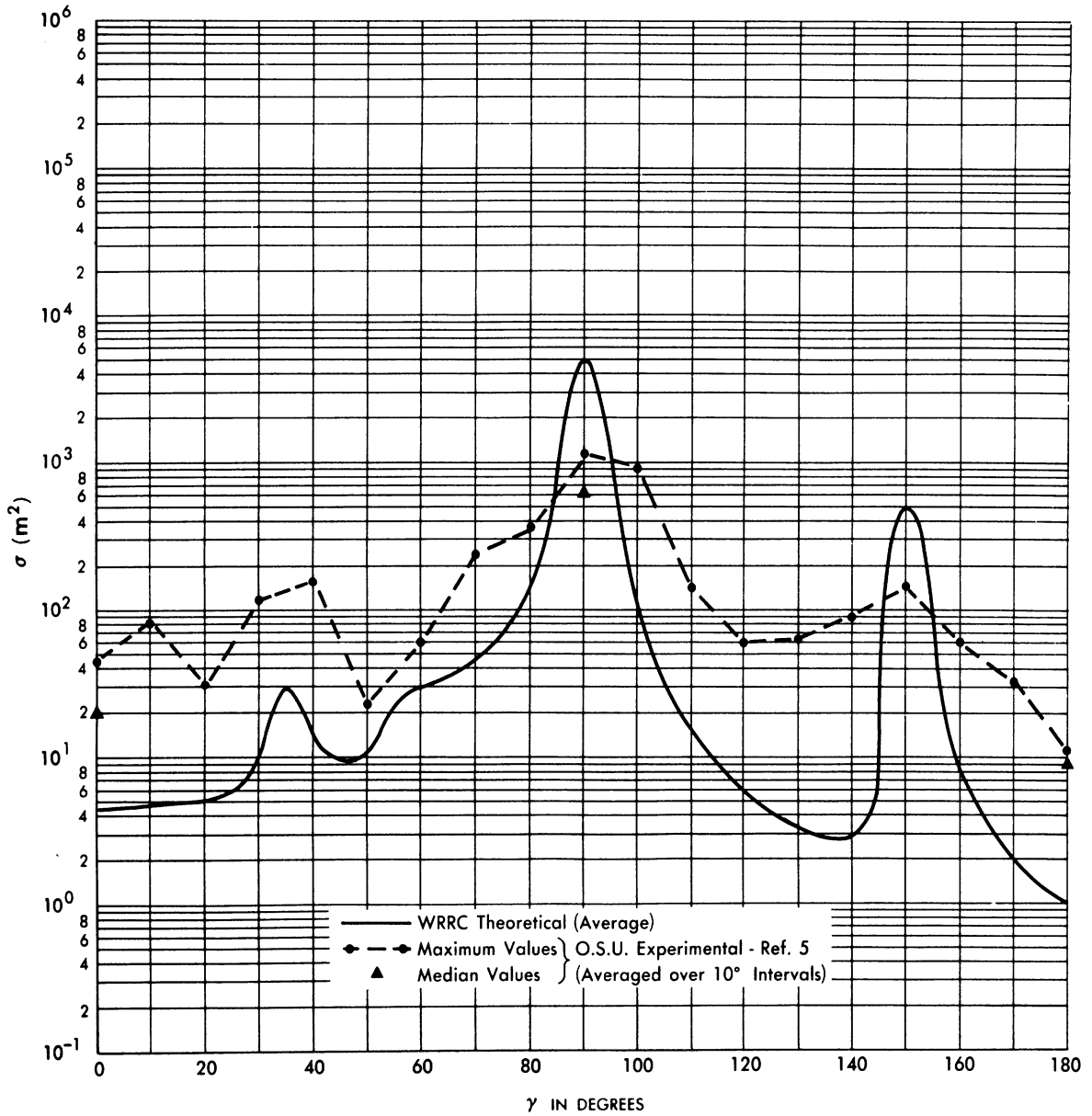


FIG. 4-4 THE B-47 - COMPARISON BETWEEN THEORY FOR $\beta = 0^\circ$ AND $\lambda = 4.57$ m. AND O.S.U. EXPERIMENTAL DATA FOR $\beta = 0^\circ$ AND $\lambda = 4.11$ m (Horizontal Polarization)

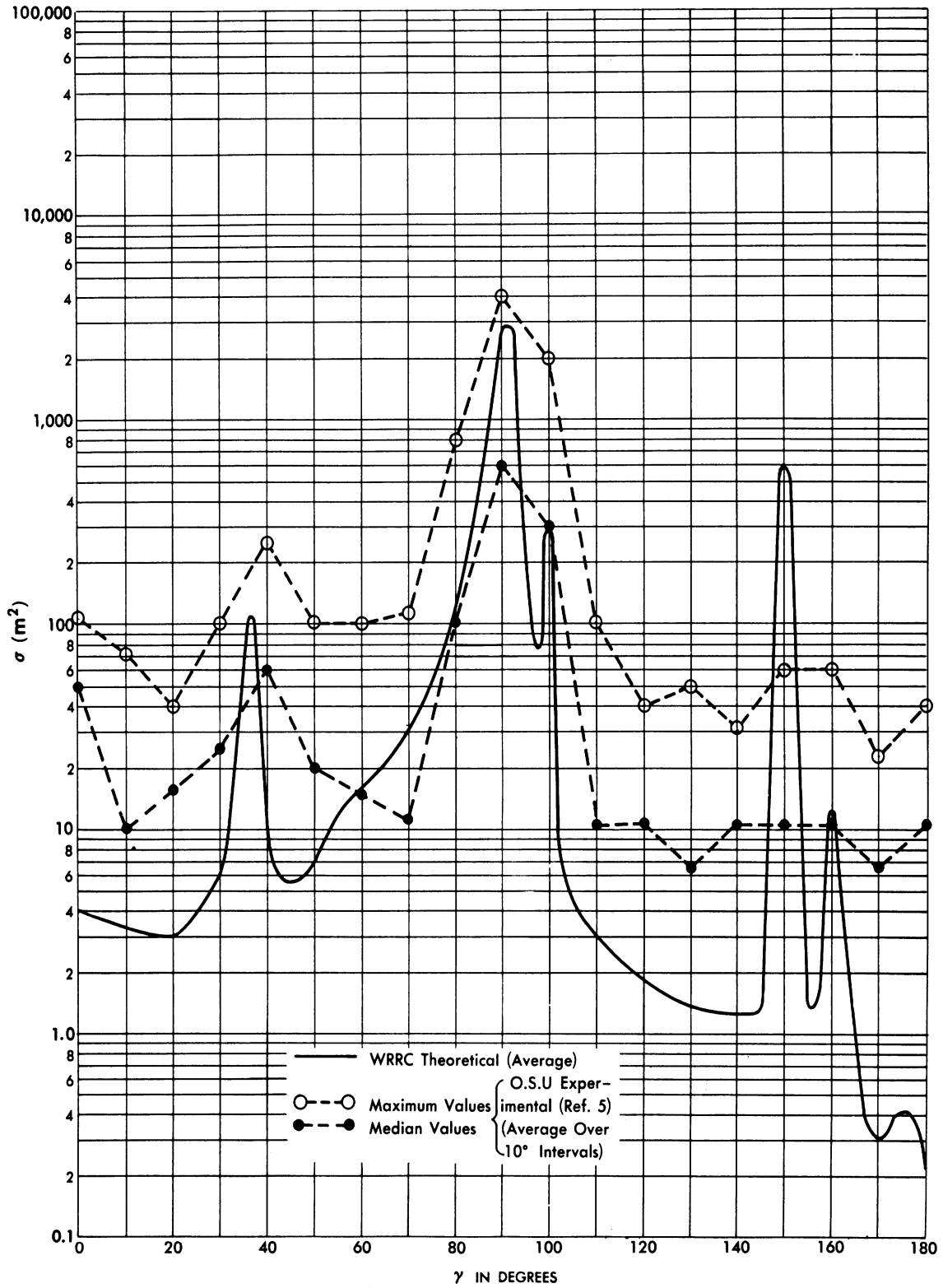


FIG. 4 - 5 THE B-47 - COMPARISON BETWEEN THEORY FOR $\beta=0^\circ$ AND $\lambda=91.4$ cm AND O.S.U. EXPERIMENTAL DATA FOR $\beta=0^\circ$ AND $\lambda=154$ cm. (Horizontal Polarization)

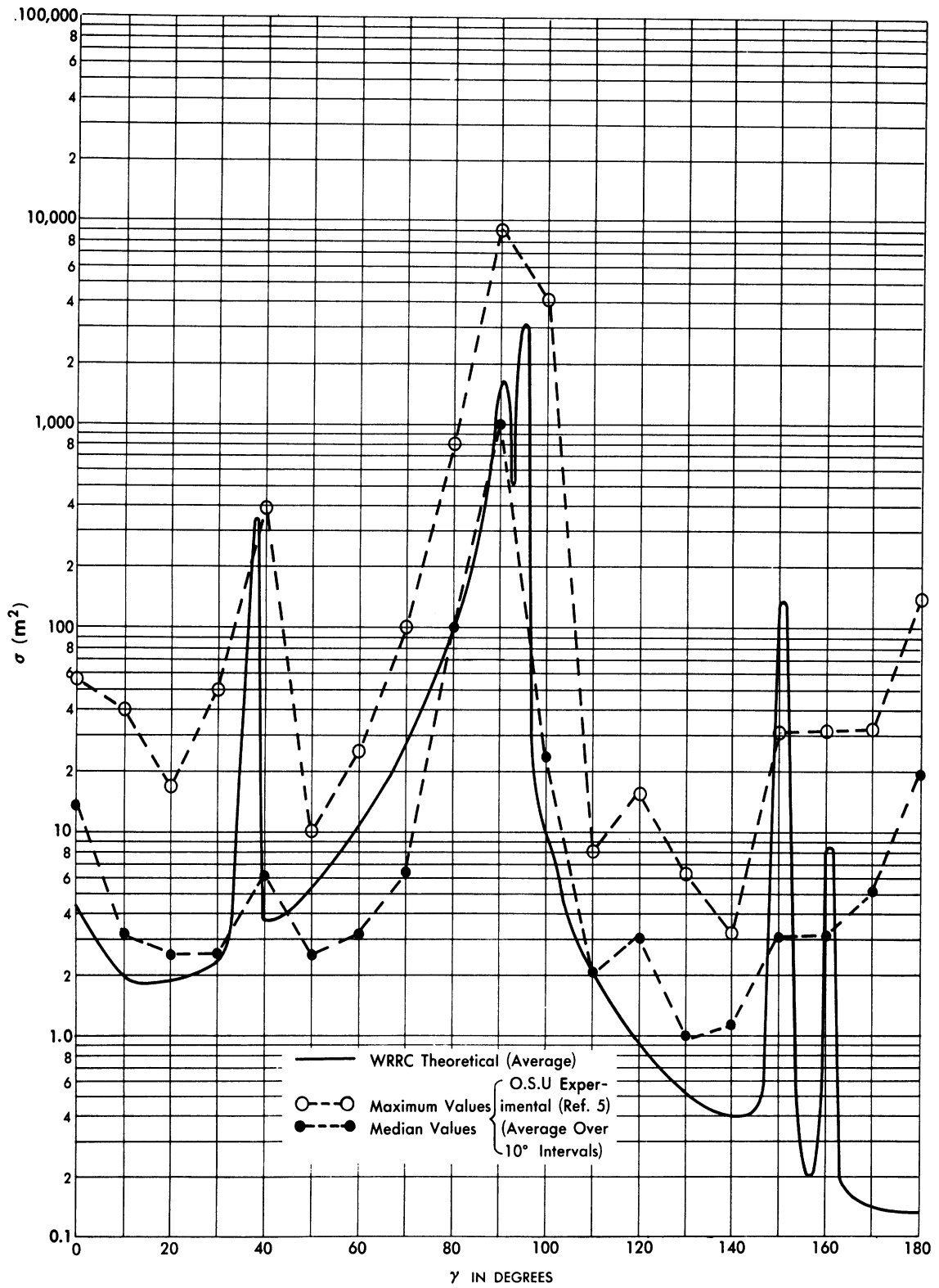


FIG. 4-6 THE B-47 - COMPARISON BETWEEN THEORY FOR $\beta=0^\circ$ AND $\lambda=30.5$ cm AND O.S.U. EXPERIMENTAL DATA FOR $\beta=0^\circ$ AND $\lambda=50$ cm (Horizontal Polarization)

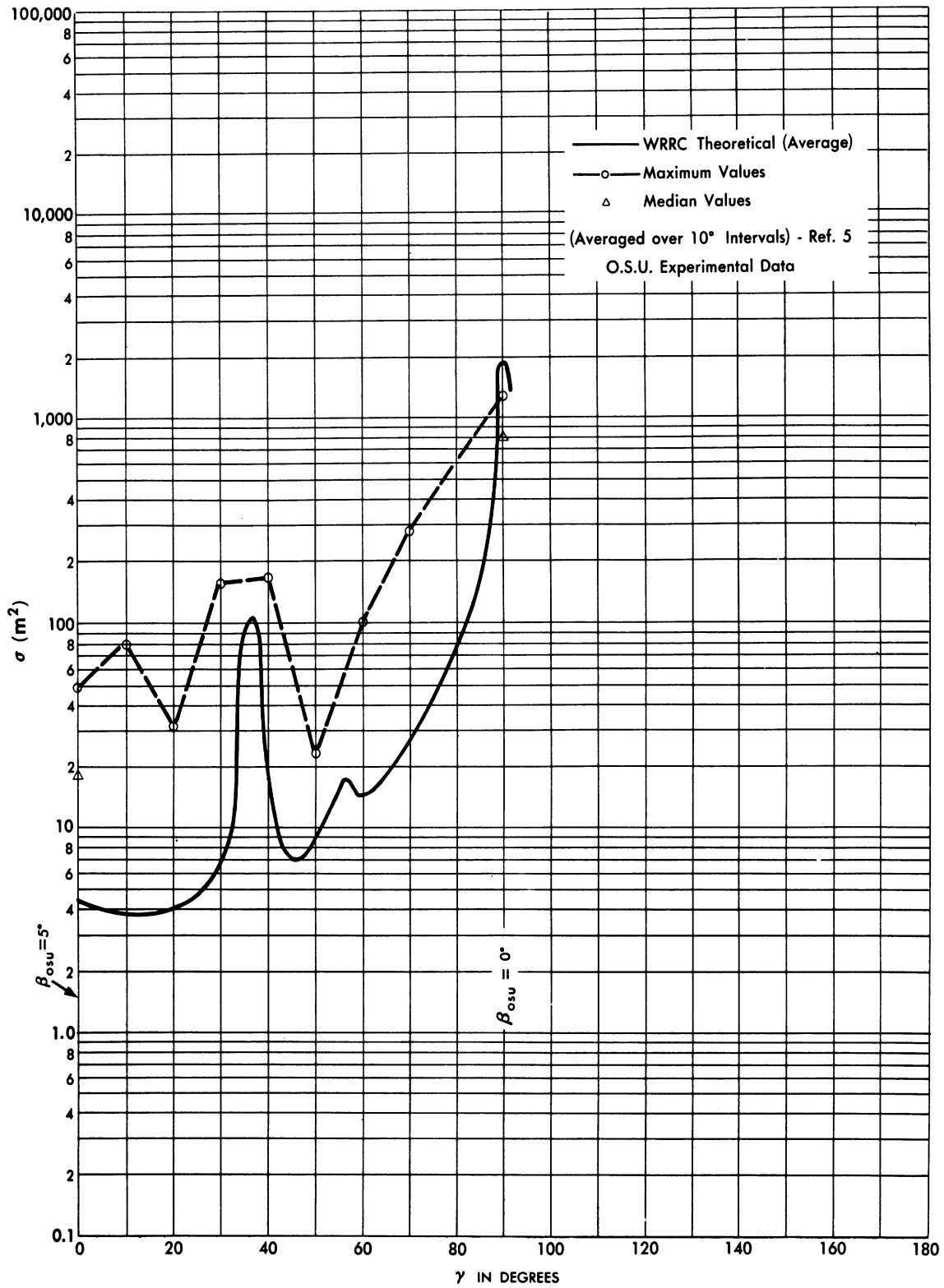


FIG. 4 - 7 THE B-47 - COMPARISON BETWEEN THEORY FOR $\beta=4^\circ$ AND $\lambda=4.57m$ AND O.S.U. EXPERIMENTAL DATA FOR $\lambda=4.11m$ AND $0^\circ \leq \beta \leq 5^\circ$ (Horizontal Polarization)

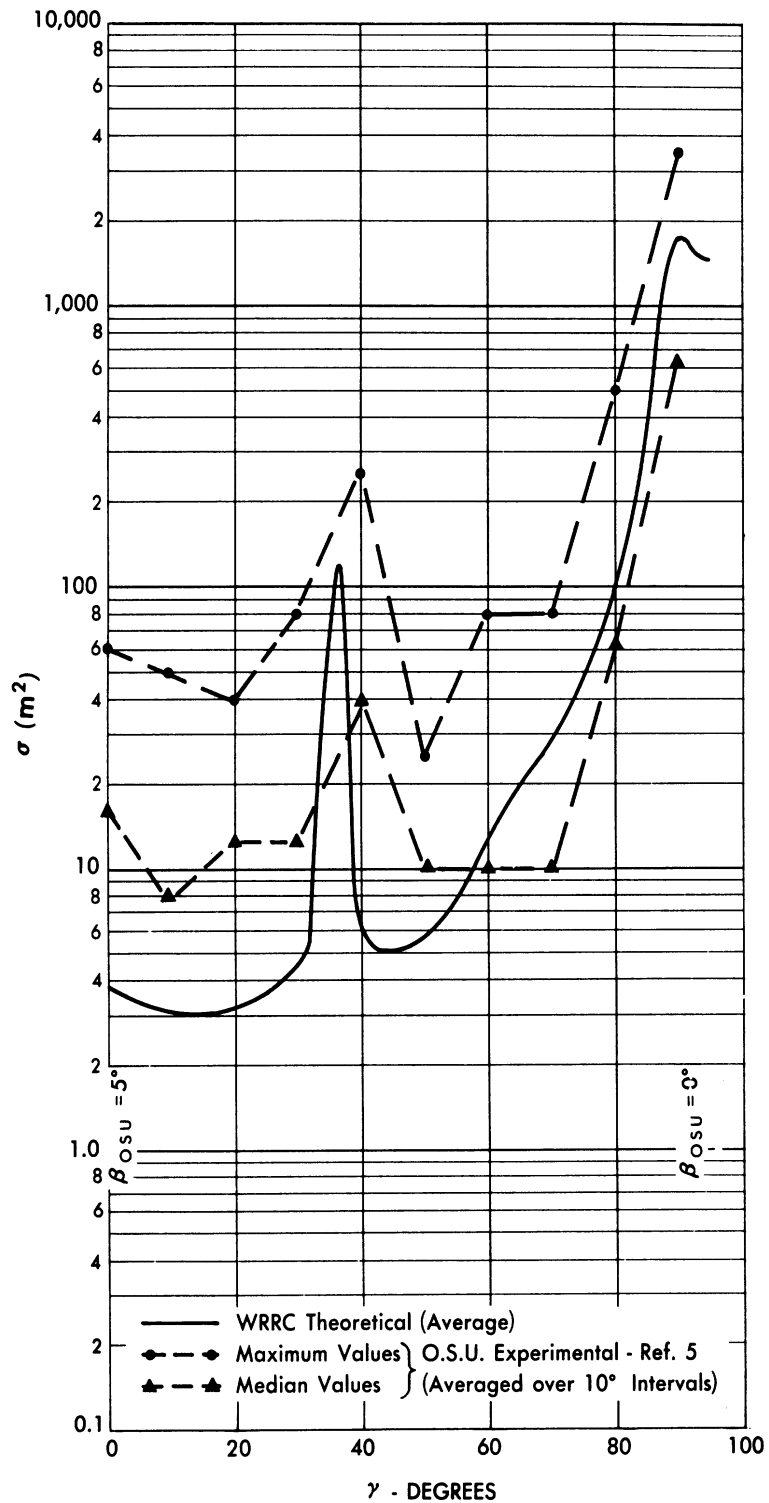


FIG. 4-8 THE B-47 - COMPARISON BETWEEN THEORY FOR $\beta=4^\circ$ AND $\lambda=91.4cm$ AND O.S.U. EXPERIMENTAL DATA FOR $\lambda=154cm$ AND $0^\circ \leq \beta \leq 5^\circ$ (Horizontal Polarization)

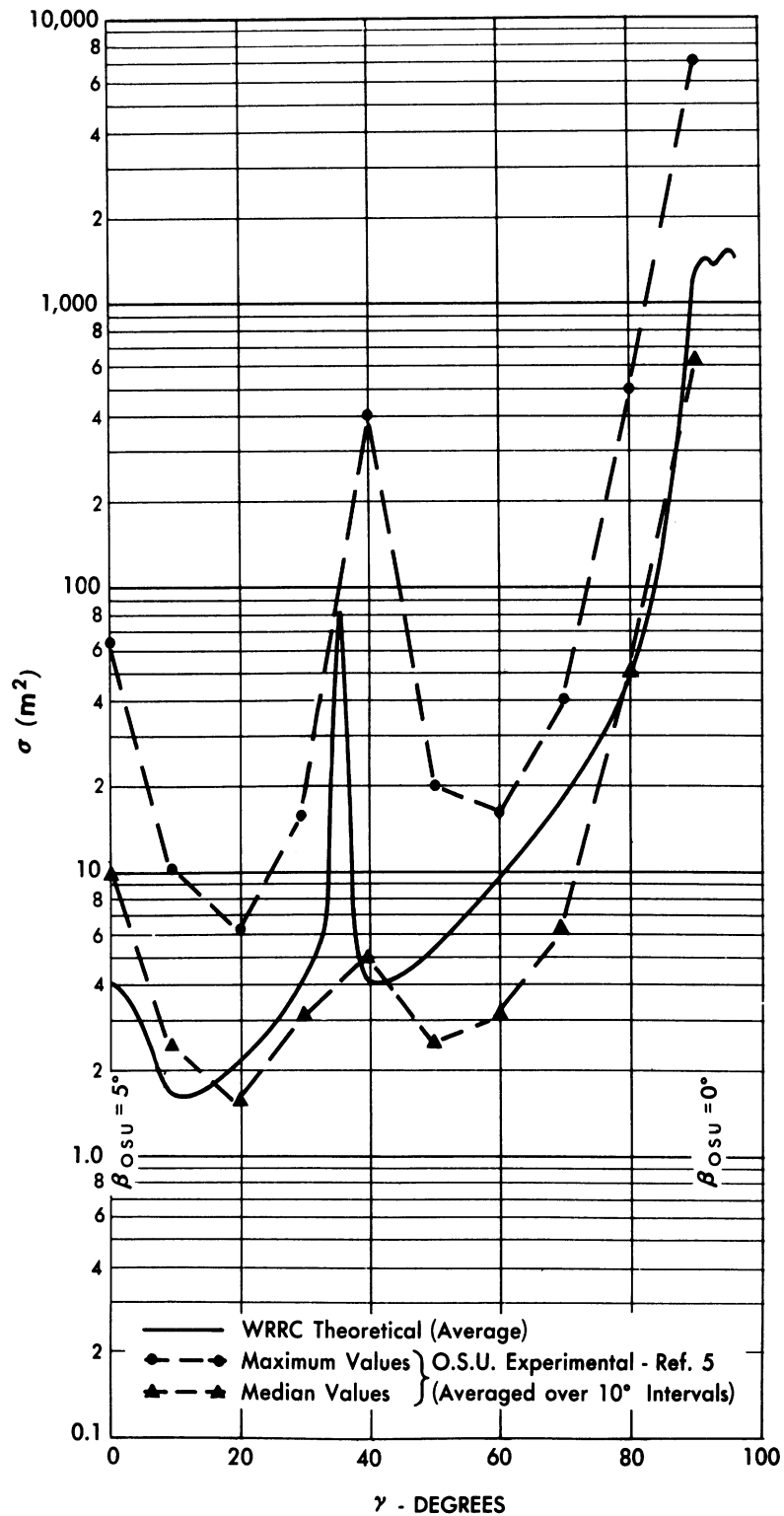


FIG. 4-9 THE B-47 - COMPARISON BETWEEN THEORY FOR $\beta=4^\circ$ AND $\lambda=30.5$ cm AND O.S.U. EXPERIMENTAL DATA FOR $\lambda=50$ cm AND $0^\circ \leq \beta \leq 5^\circ$ (Horizontal Polarization)

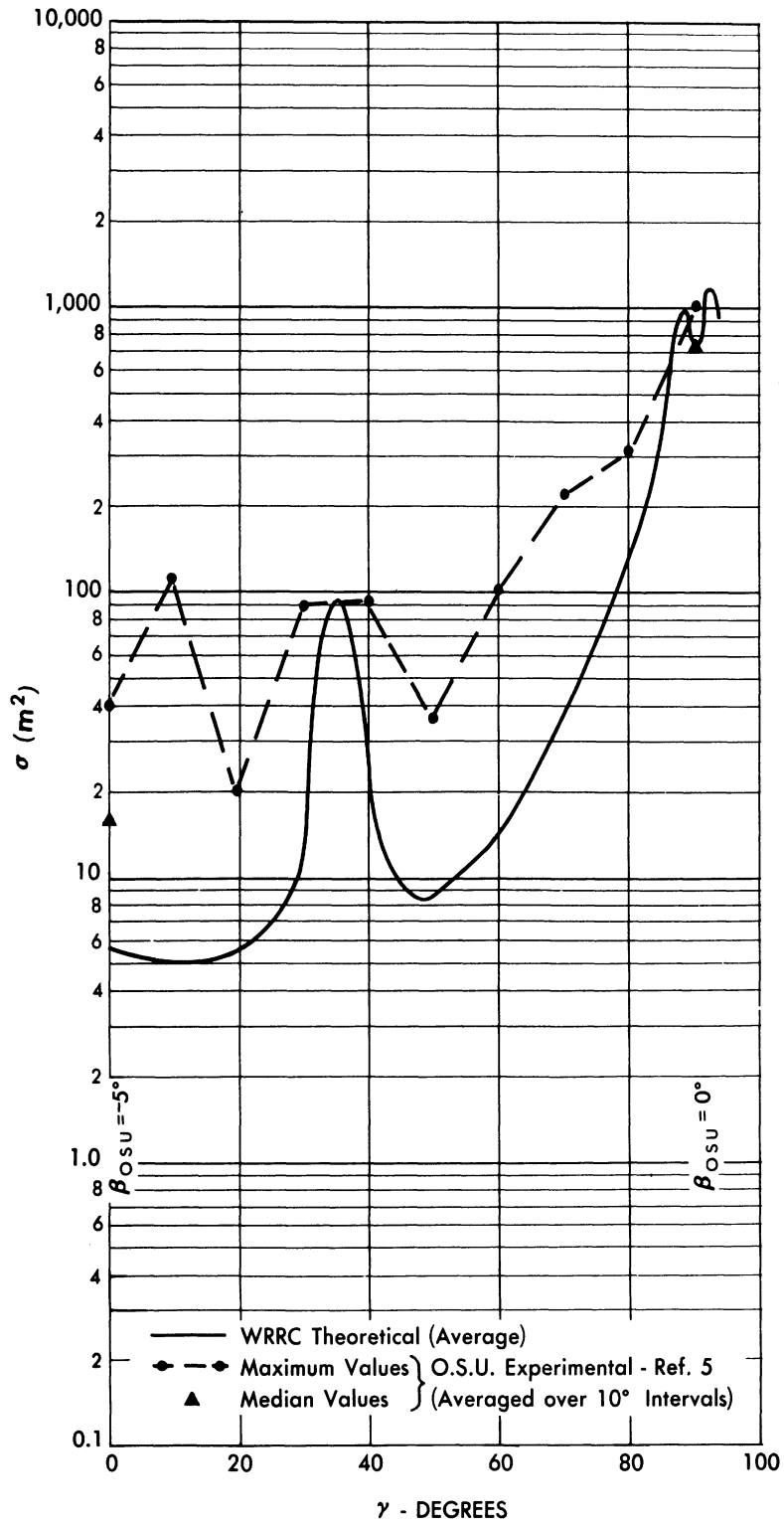


FIG. 4 - 10 THE B-47 - COMPARISON BETWEEN THEORY FOR $\beta: -4^\circ$ AND $\lambda = 4.57$ m AND O.S.U. EXPERIMENTAL DATA FOR $\lambda = 4.11$ m AND $-5^\circ \leq \beta \leq 0^\circ$ (Horizontal Polarization)

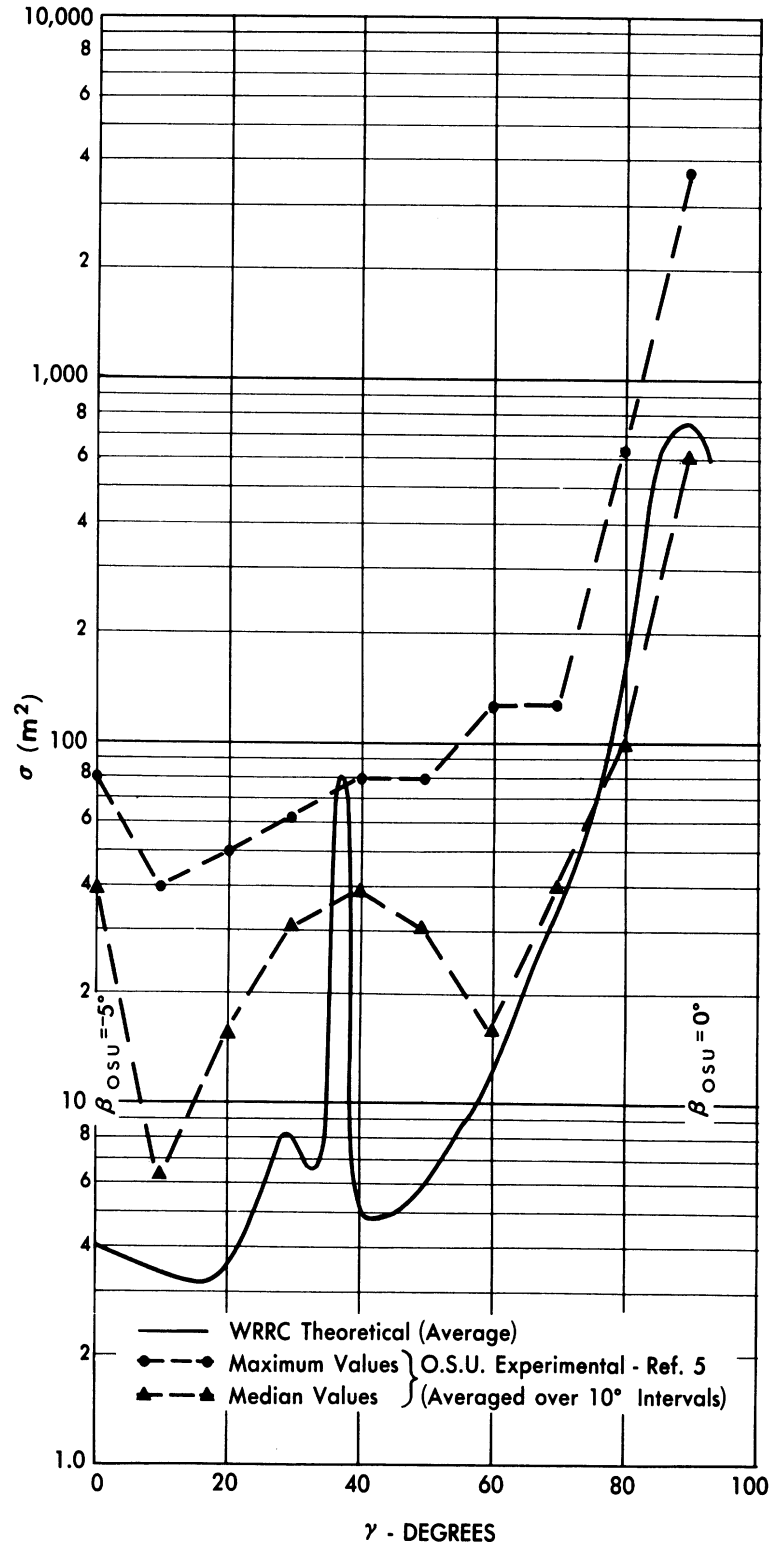


FIG. 4 - 11 THE B-47 - COMPARISON BETWEEN THEORY FOR $\beta = -4^\circ$ AND $\lambda = 91.4$ cm AND O.S.U. EXPERIMENTAL DATA FOR $\lambda = 154$ cm AND $-5^\circ \leq \beta \leq 0^\circ$ (Horizontal Polarization)

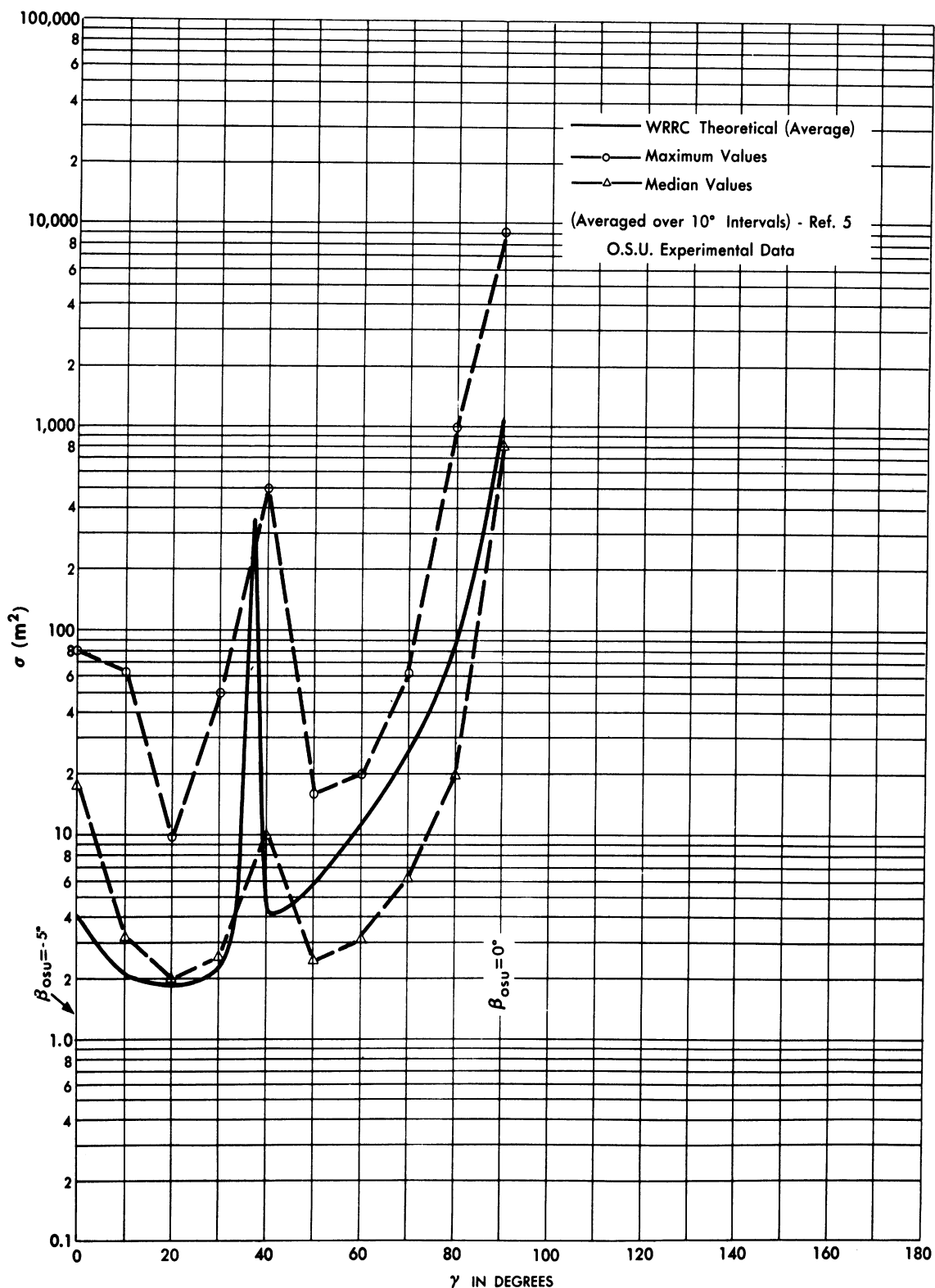


FIG. 4 - 12 THE B - 47 - COMPARISON BETWEEN THEORY FOR $\beta = -4^\circ$ AND $\lambda = 30.5$ cm AND O.S.U. EXPERIMENTAL DATA FOR $\lambda = 50$ cm AND $-5^\circ \leq \beta \leq 0^\circ$ (Horizontal Polarization)

in Figures 4-7 through 4-12 the comparison is made only in the $0^\circ \leq \beta \leq 90^\circ$ interval because of the differences in the two geometries. The results of these later Ohio State experiments appear in Reference 5¹.

The Hughes Aircraft Company has conducted dynamic radar cross-section tests on the B-47 at 9245 Mc (Ref. 6). For all crossing runs, the points are averaged over an aspect angle of $\pm 5^\circ$ (10° average). For the tail and nose aspects the points are averaged over an elevation angle of $\pm 2.5^\circ$ (5° average). Their results given in the above reference are contained in Figure 4-13. The theoretical results are also shown on the figure for comparison purposes.

The Aircraft Radiation Laboratory of the Wright Air Development Center has conducted several dynamic experiments on the B-47. Their experiments were conducted at X-band. Preliminary X-band results, published in Reference 7, were: nose-on: 24 square meters, tail-on: 12 square meters, and broadside: 178 square meters.

More extensive results by Wright Field, previously unpublished are presented in Figures 4-14 and 4-15. These results were furnished by W. Bahret from the results obtained by G. W. Schivley, H. Trigg, and himself. Comparisons have been made between theory and experiment and these comparisons are shown on the above mentioned figures. Figure 4-14 shows a comparison between these dynamic experiments and the theoretical results of Section II for $\beta = 0^\circ$ and $0^\circ \leq \gamma \leq 90^\circ$ and Figure 4-15 shows the comparison for $\gamma = 0^\circ$ and $0^\circ \leq \beta \leq 12^\circ$.

It may be noted that the nose-on experimental results are consistently higher than the theoretical nose-on results. This may be because we have assumed that very little of the energy which went into holes would return in the same direction as it went in. If future experimental results indicate the presently reported data is in the correct range, then this assumption should be considered further.

Knowing the great difficulties inherent to dynamic experiments (Ref. 8) and previous disagreements between the experiments made by different organizations on the same configuration (Ref. 9), the comparisons shown in the figures of this section are extremely encouraging.

¹These figures display the maximum and median values measured by Ohio State University over ten degree intervals compared with the average of the computed values.

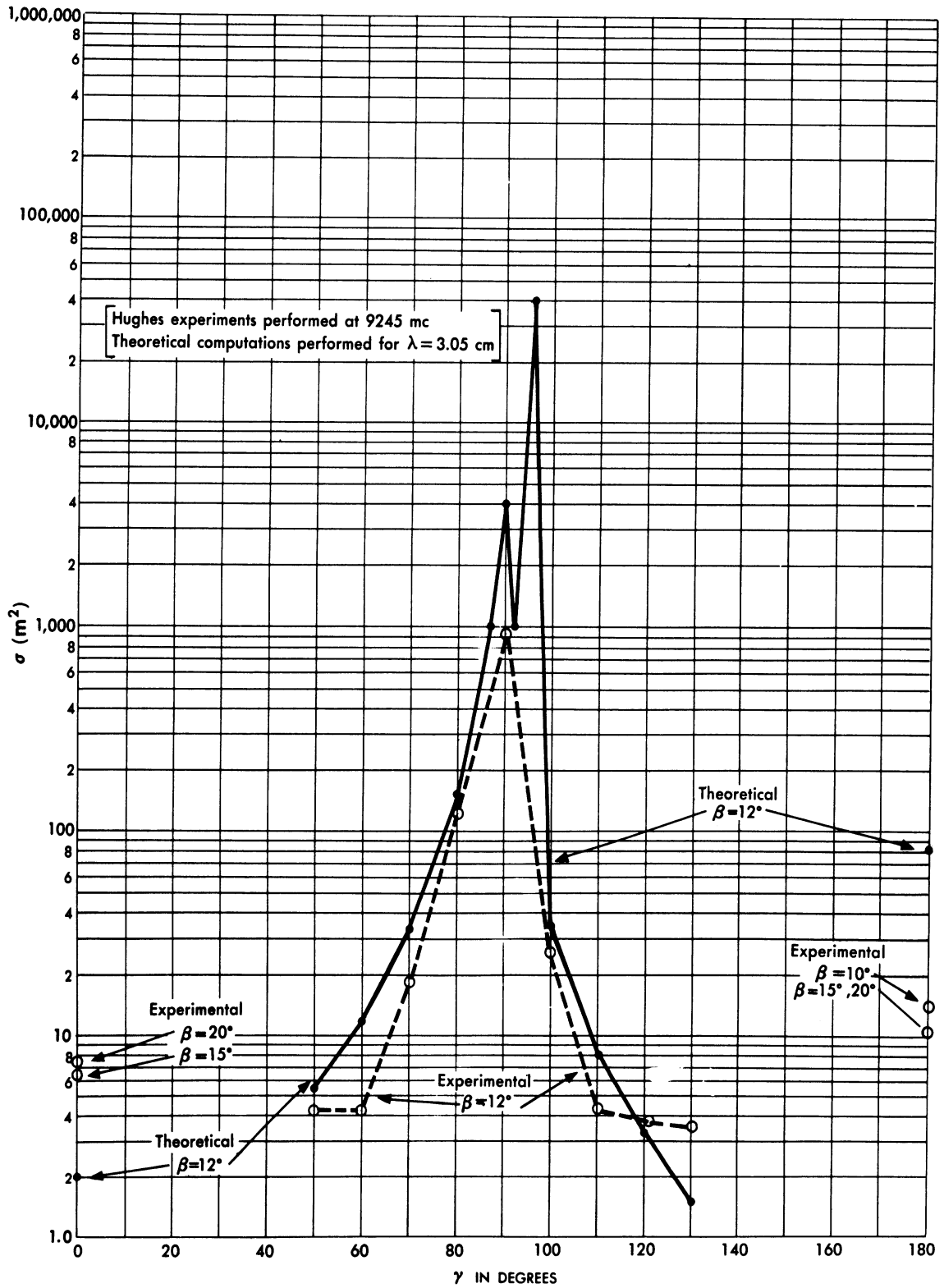


FIG. 4 - 13 THE B-47 - COMPARISON BETWEEN THEORY AND DYNAMIC EXPERIMENTAL DATA (The Hughes Aircraft Company) AT X - BAND. (Vertical Polarization; $10^\circ \leq \beta \leq 20^\circ$)

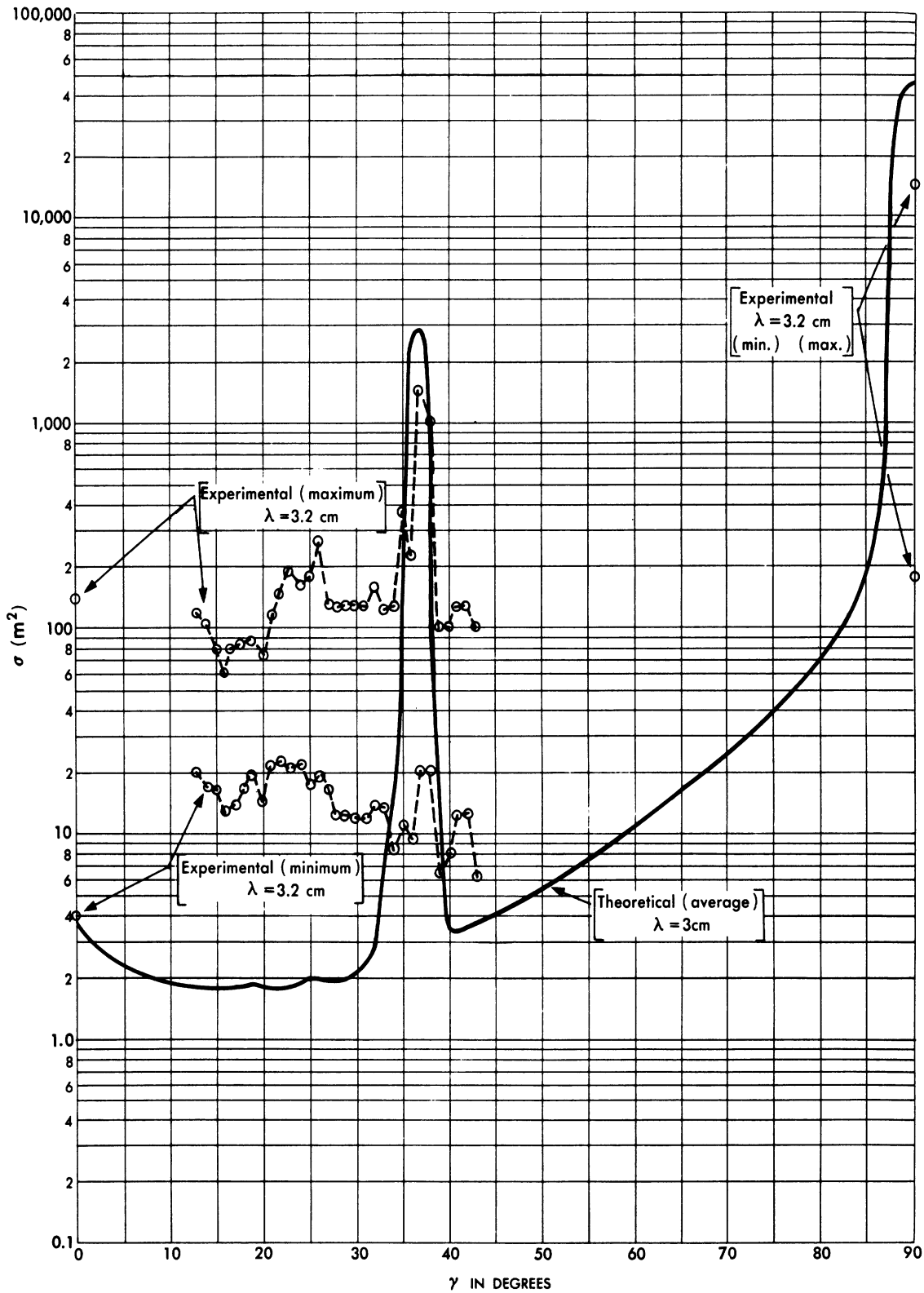


FIG. 4-14 THE B-47 - COMPARISON BETWEEN THEORY AND DYNAMIC EXPERIMENTAL DATA (Aircraft Radiation Laboratory of the Wright Air Development Center) AT X-BAND. (Vertical Polarization; $\beta=0^\circ$)

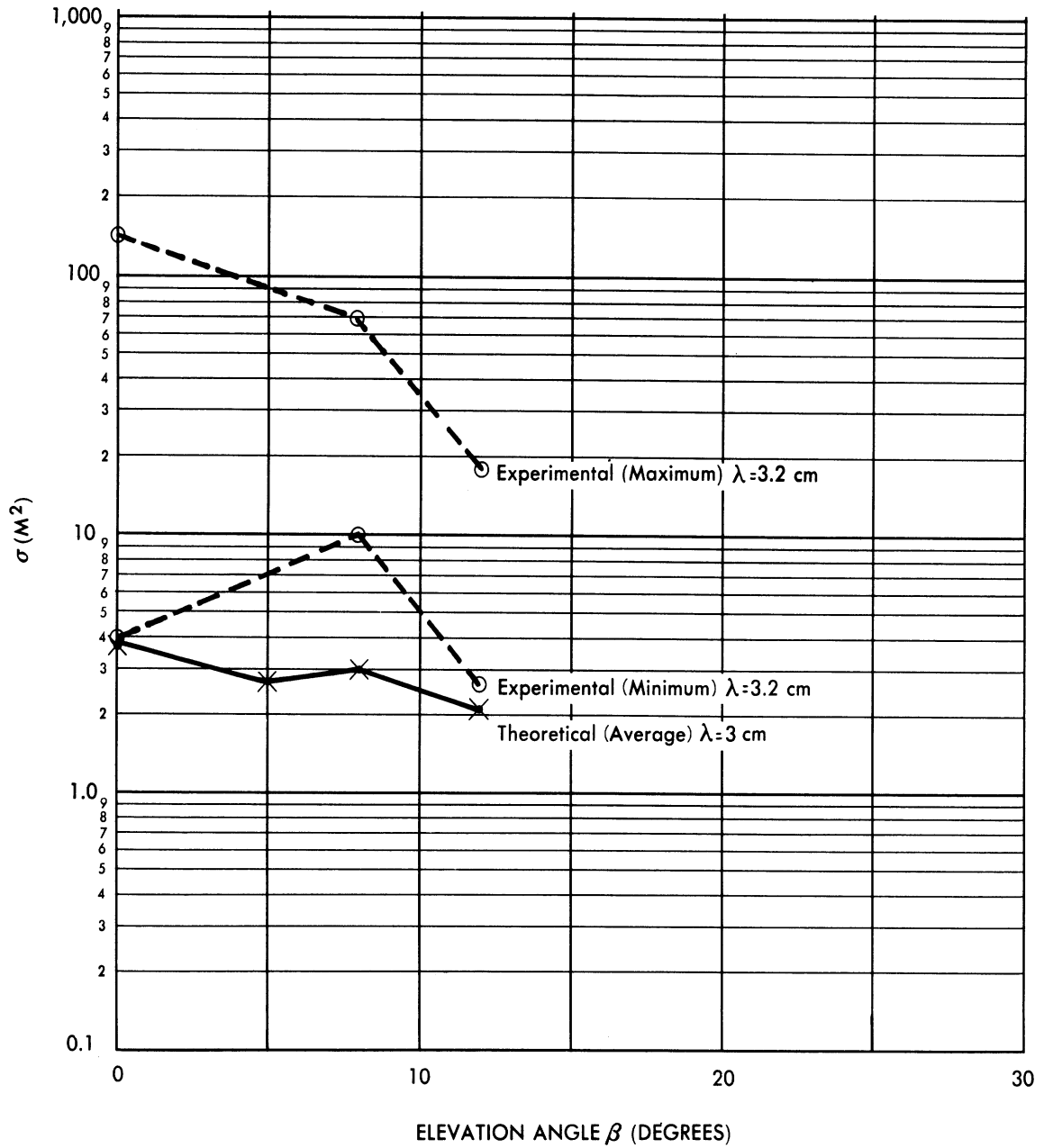


FIG. 4-15 THE B-47 - COMPARISON BETWEEN THEORY AND DYNAMIC EXPERIMENTAL DATA (Aircraft Radiation Laboratory of the Wright Air Development Center) AT X-BAND (Vertical Polarization; $\gamma=0^\circ$)

~~CONFIDENTIAL~~
CONFIDENTIAL

UNIVERSITY OF MICHIGAN

2260-1-T

REFERENCES: TEXT

- | <u>Number</u> | <u>Title</u> |
|---------------|---|
| 1 | Kerr, D. E., <u>Propagation of Short Radio Waves</u> , Volume 13, MIT Radiation Laboratory Series, McGraw-Hill Book Co., 1951. |
| 2 | "Echo Measurements of the B-47 Aircraft", Data Set No. 3 on Contract AF 33(038)-10101, 12 June 1952, Antenna Laboratory, The Ohio State University Research Foundation.
CONFIDENTIAL |
| 3 | "Present Status of the Systems for Measuring Radar Back-Scattering Coefficients", Report 302-28 on Contract W 36-039 sc 33634, 15 May 1949, Antenna Laboratory, The Ohio State University Research Foundation. CONFIDENTIAL |
| 4 | "An Investigation of Pulsed Radar Systems for Model Measurements", Report 475-6 on Contract AF 18(600)-19, 1 December 1953, Antenna Laboratory, The Ohio State University Research Foundation. CONFIDENTIAL |
| 5 | "The Echo Area of the B-47 Aircraft at Several Frequencies", Report 601-2 on Contract AF 33(616)-2546, Antenna Laboratory, Ohio State University Research Foundation (to be published). |
| 6 | Wanlass, S. D., Muchmore, R. B., and Jacob, D. M., "X-Band Radar Cross-Section Measurements", Technical Memorandum No. 341, The Hughes Aircraft Company, 1 March 1954. CONFIDENTIAL |
| 7 | Schivley, G. W., "Measurements of B-47 Aircraft Dynamic Reflection Characteristics", Technical Note WCER 52-1, Aircraft Radiation Laboratory, Wright Air Development Center, June 1952. CONFIDENTIAL |

UNIVERSITY OF MICHIGAN

2260-1-T

REFERENCES: TEXT (Continued)

<u>Number</u>	<u>Title</u>
8	UMM-128, "Studies in Radar Cross-Sections XIII - Description of a Dynamic Measurement Program", by K. M. Siegel and J. M. Wolf, University of Michigan, Willow Run Research Center, May 1954 . CONFIDENTIAL
9	UMM-127, "Studies in Radar Cross-Sections XII - Summary of Radar Cross-Section Studies Under Project MIRO", by K. M. Siegel, M. E. Anderson, R. R. Bonkowski and W. C. Orthwein, University of Michigan, Willow Run Research Center, December 1953 . SECRET

APPENDIX A

(UNCLASSIFIED when detached from report.)

RADAR CROSS-SECTION COMPUTATION PROCEDURES

A.1 INTRODUCTION

This appendix contains a set of notes prepared by one of the authors, C. E. Schensted, for use by the computation personnel. These notes are presented here verbatim except for changes in numbering to conform with the rest of this report¹. They show the methods by which the computations were performed and may serve as reference material for other workers in the field who wish to calculate the approximate radar cross-sections of complex bodies such as the B-47 and B-52 aircraft. Application of the methods to obtain the numerical results summarized in the body of this report is discussed in Appendix B.

The procedure used requires a knowledge of approximate radar cross-sections of a variety of scatterers of relatively simple shapes, such as ellipsoids, ogives, rings, corner reflectors, etc., and formulas for these cross-sections are catalogued in Section A.3 of this appendix.

A.1.1 Definition of Radar Cross-Section

The radar cross-section, σ , of an object is determined by the ratio of the intensities of the scattered and incident electromagnetic fields on the assumption that the incident energy forms a homogeneous plane wave. If the amount of energy crossing unit area perpendicular to the direction of incidence in unit time in the incident field is I_i and if the amount of energy crossing unit area in unit time at the receiver due to the scattered field is I_s , then the radar cross-section is defined as

$$\sigma = \lim_{R \rightarrow \infty} 4\pi R^2 \left| \frac{I_s}{I_i} \right| \quad (\text{A.1-1})$$

¹ Because these notes are verbatim, the nomenclature for angles used in this appendix differs from that used in the body of the report.

where R is the distance from the scattering object to the receiver. Since I_s varies proportionally to $1/R^2$ this limit exists.

When the transmitter and receiver are located at the same place we call σ the monostatic cross-section, otherwise we call it the bistatic cross-section. Only monostatic cross-sections will be considered in the following. When the receiving antenna is not polarized in the same way as the scattered field the receiver signal is reduced. Thus for linear polarization the measured cross-section is reduced by an amount proportional to the square of the cosine of the angle between the two polarizations. It is this apparent cross-section with which we are concerned here.

A. 1.2 Procedure

In order to compute cross-sections exactly, it is necessary to solve Maxwell's electromagnetic field equations, which lead to a single vector partial differential equation, the vector wave equation, subject to boundary conditions. Except for a few simple shapes this solution has not yet been found possible. Since exact methods are not at present available, we must resort to approximation techniques. First, as a result of the extreme complexity of the shape of aircraft, we assume that various parts of the aircraft scatter independently. We approximate the parts of the aircraft by relatively simple shapes, compute the cross-sections of the individual parts, and then combine the component cross-sections in an appropriate way. The second approximation which must be made is in determining the cross-sections of the individual parts since exact answers are not available. We will first discuss the procedures and the validity of breaking down the aircraft into component parts and the method of combining cross-sections. We will then discuss methods of obtaining approximations to the cross-sections of the parts, and we will list a number of formulas for various shapes.

A. 1.3 Replacing Parts of the Aircraft by Simple Shapes

In replacing a part of a complex structure like an aircraft by a simple shape, the most important consideration is that the wavelength dependence of the cross-section of the simple shape be the same as the

wavelength dependence of the cross-section of the true configuration. Thus in Figure A-1 the cross-section of the curved body of revolution is approximately independent of wavelength whereas the cross-section of the cylinder is proportional to $\frac{1}{\lambda}$ for incident radiation in the direction A and is proportional to λ for the direction B. As a result at short wavelengths the cross-section of the cylinder will be much too large at normal incidence (direction A) and much too small for off-normal incidence to permit the cylinder to be used as an approximation to the other body. In a similar way a body with a rounded tip should not be replaced by a body with a pointed tip and a body which is tangential to the direction of incidence at the shadow curve (the shadow curve is the curve separating the part of the body illuminated by the incident radiation from the part of the body in shadow) should not be replaced by a body which has a sharp kink at the shadow curve.

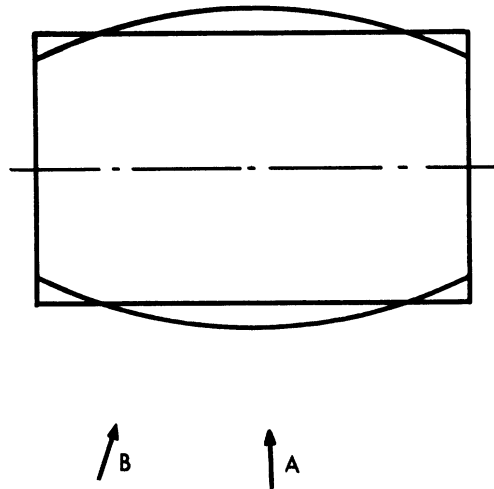


FIG. A-1

The second important consideration in replacing the aircraft by simple shapes is that the formulas for the cross-sections of the simple shapes be as simple as possible so that the computation presents as little difficulty as possible. Along this line the simplest approximate formula for the cross-section of the simple shape should be chosen within the restriction that the approximation is reasonable.

A. 1. 4 Combination of Component Cross-Sections

Only electromagnetic fields which are time harmonic will be considered here. The electric and magnetic fields will be taken to be the real parts of $\vec{E}e^{-i\omega t}$ and $\vec{H}e^{-i\omega t}$ where \vec{E} and \vec{H} are complex vectors. However, we will always consider the complex vectors \vec{E} and \vec{H} , and we will call these the electric and magnetic fields. The definition of cross-section given in Equation (A. 1-1) is equivalent to

$$\sigma = \lim_{R \rightarrow \infty} 4\pi R^2 \left| \frac{\vec{E}_s}{\vec{E}_i} \right|^2 = \lim_{R \rightarrow \infty} 4\pi R^2 \left| \frac{\vec{H}_s}{\vec{H}_i} \right|^2 \quad (\text{A. 1-2})$$

The assumption that various parts of the aircraft scatter independently is equivalent to saying that we can write $\vec{E}_s = \sum_n \vec{E}_n$ where \vec{E}_n can be obtained by considering only a part of the aircraft. The approximate methods which we will use to compute \vec{E}_n will predict (with reasonable but not perfect accuracy) that \vec{E}_n is linearly polarized (assuming, as we are, that the incident field is linearly polarized). With this approximation we can write $\vec{E}_n = \frac{\sqrt{\sigma_n}}{R\sqrt{4\pi}} \hat{e}_n e^{ik\phi_n}$ where σ_n is the cross-section

of the nth component, \hat{e}_n is a real unit vector, and ϕ_n is a phase factor (the magnitude of the incident field has been taken to be unity). With these approximations, Equation (A. 1-2) reduces to

$$\sigma = \left| \sum_n \sqrt{\sigma_n} \hat{e}_n e^{ik\phi_n} \right|^2 \quad (\text{A. 1-3})$$

As noted earlier we are only interested in determining the "effective" cross-section, which determines what the signal received will be. If \hat{d} is a unit vector in the direction in which the receiver is polarized then this effective cross-section becomes (with the approximations which are being used here)

$$\sigma_e = \left| \sum_n \sqrt{\sigma_n} (\hat{d} \cdot \hat{e}_n) e^{ik\phi_n} \right|^2 \quad (\text{A. 1-4})$$

For small wavelengths the value of $k\phi_n$ depends very critically on the wavelength and the dimensions of the aircraft so that these quantities

would have to be determined with extreme precision in order to get accurate values of $k\phi_n$. A more fundamental obstacle to obtaining accurate values of the phase function $k\phi_n$ is that the approximate methods which we use can not be expected to give accurate values of $k\phi_n$ (although they can be expected to give accurate values of σ_n). As a result of these difficulties we will not know the value of $k\phi_n$ accurately. But if all values of $k\phi_n$ are equally likely then we can use the average value, $\bar{\sigma}_e$, and the RMS spread, $\sqrt{(\sigma_e - \bar{\sigma}_e)^2}$, where the averages are with respect to the values of $k\phi_n$. We find that

$$\begin{aligned} \bar{\sigma}_e &= \frac{\left| \sum_n \sqrt{\sigma_n} (\hat{d} \cdot \hat{e}_n) e^{ik\phi_n} \right|^2}{\sum_n \sum_m \sqrt{\sigma_n \sigma_m} (\hat{d} \cdot \hat{e}_n) (\hat{d} \cdot \hat{e}_m) e^{ik(\phi_n - \phi_m)}} \\ &= \sum_n \sum_m \sqrt{\sigma_n \sigma_m} (\hat{d} \cdot \hat{e}_n) (\hat{d} \cdot \hat{e}_m) \delta_{nm} \\ &= \sum_n \sigma_n (\hat{d} \cdot \hat{e}_n)^2 \end{aligned} \tag{A.1-5}$$

$$\begin{aligned} \bar{\sigma}_e^2 + \overline{(\sigma_e - \bar{\sigma}_e)^2} &= \left(\left| \sum_n \sqrt{\sigma_n} (\hat{d} \cdot \hat{e}_n) e^{ik\phi_n} \right|^2 - \bar{\sigma}_e \right)^2 \\ &= \left| \sum_n \sqrt{\sigma_n} (\hat{d} \cdot \hat{e}_n) e^{ik\phi_n} \right|^4 \\ &= \sum_n \sum_m \sum_p \sum_q \sqrt{\sigma_n \sigma_m \sigma_p \sigma_q} (\hat{d} \cdot \hat{e}_n) (\hat{d} \cdot \hat{e}_m) (\hat{d} \cdot \hat{e}_p) (\hat{d} \cdot \hat{e}_q) e^{ik(\phi_n - \phi_m + \phi_p - \phi_q)} \end{aligned}$$

$$= \sum_n \sum_m \sum_p \sum_q \sqrt{\sigma_n \sigma_m \sigma_p \sigma_q} (\hat{d} \cdot \hat{e}_n) (\hat{d} \cdot \hat{e}_m) (\hat{d} \cdot \hat{e}_p) (\hat{d} \cdot \hat{e}_q) \left[\delta_{nm} \delta_{pq} + \delta_{nq} \delta_{mp} - \delta_{nm} \delta_{pq} \delta_{nq} \delta_{mp} \right]$$

$$= 2 \bar{\sigma}_e^2 - \sum_n \sigma_n^2 (\hat{d} \cdot \hat{e}_n)^4$$

If we let $\sigma_n (\hat{d} \cdot \hat{e}_n)^2 = \sigma_{ne}$ then we use for the cross-section

$$\sigma_e = \sum_n \sigma_{ne} \pm \sqrt{\left(\sum_n \sigma_{ne} \right)^2 - \sum_n \sigma_{ne}^2} \quad (\text{A.1-6})$$

A.1.5 Approximation of Cross-Sections

We will consider first the cross-section of a perfectly conducting wire which is many wavelengths long but only a fraction of a wavelength thick. Perhaps the simplest formula which is in good agreement with experiment is Chu's formula (Ref. A1):

$$\sigma_e = \sigma \cos^2 \phi = \frac{\pi L^2 \sin^2 \theta \left[\frac{\sin \left(\frac{2\pi L}{\lambda} \cos \theta \right)}{\frac{2\pi L}{\lambda} \cos \theta} \right]^2}{\left(\frac{\pi}{2} \right)^2 + \left(\ln \frac{\lambda}{\gamma \pi a \sin \theta} \right)^2} \cos^4 \phi, \quad (\text{A.1-7})$$

where L is the length of the wire, a is the radius of the wire, $\gamma = 1.78\dots$, θ is the angle between the wire and the direction of incidence, and ϕ is the angle between the polarization direction and the plane formed by the wire and the direction of incidence. No attempt will be made here to derive this formula. This formula presents an interesting feature which will recur often in what follows. Except for θ near 90° the two tips of the wire scatter essentially independently. A slight change in θ has a pronounced effect on the relative phase of the two components so that there is a rapid oscillation, the components sometimes adding and sometimes cancelling. When we approximate a part of the aircraft by a thin

wire we will not be able to determine the relative phase of the two components accurately so that the proper picture is to replace the wire by two independent scatterers (except for θ near 90°) each having an effective cross-section given by

$$\sigma_e = \frac{\lambda^2 \tan^2 \theta \cos^4 \phi}{16\pi \left[\left(\frac{\pi}{2}\right)^2 + \left(\ln \frac{\lambda}{\gamma \pi a \sin \theta}\right)^2 \right]} \quad (\text{A. 1-8})$$

At $\theta = 90^\circ$ Equation (A. 1-8) blows up while Equation (A. 1-7) does not. The reason for this is that at this one aspect the wire acts as a single scatterer. For $\theta = 90^\circ$ then we must use Equation (A. 1-7) which reduces to:

$$\sigma_e = \frac{\pi L^2 \cos^4 \phi}{\left(\frac{\pi}{2}\right)^2 + \left(\ln \frac{\lambda}{\gamma \pi a}\right)^2} \quad (\text{A. 1-9})$$

It can be seen that Equations (A. 1-8) and (A. 1-9) do not have the same wavelength dependence. Figure (A-2) shows the way that Equation (A. 1-8) goes into Equation (A. 1-9) at $\theta = 90^\circ$ for a number of wavelengths.

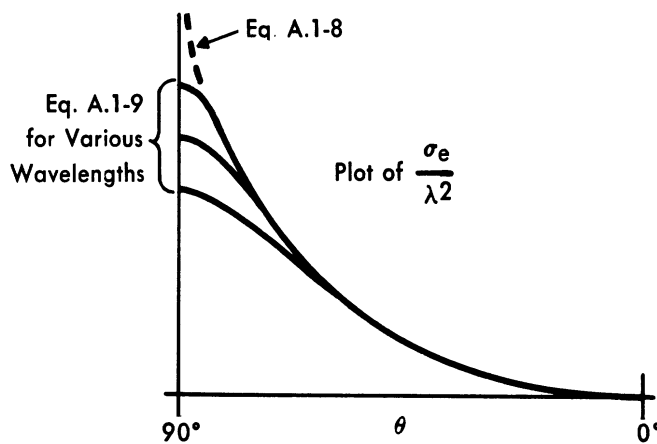


FIG. A-2

In actual use the single value at $\theta = 90^\circ$ given by Equation (A.1-9) would be faired into the curve given by Equation (A.1-8) graphically. In Figure A-2 it has been assumed that the slight dependence of σ_e/λ^2 on λ (as given by Equation (A.1-8)) due to the logarithmic term is negligible.

The procedure which has been followed here will always be used when it is found that the cross-section of some component oscillates wildly when the dimensions, wavelength, or aspect is changed.

Some of the methods of approximation which will be used in the remainder are derived from the following equations (Ref. A2)¹.

$$\vec{E}_s = \frac{1}{4\pi} \int_s \left[ik \hat{n} \times \vec{H} \frac{e^{ikr}}{r} + (\hat{n} \times \vec{E}) \times \nabla \frac{e^{ikr}}{r} + (\hat{n} \cdot \vec{E}) \nabla \frac{e^{ikr}}{r} \right] ds \quad (\text{A.1-10})$$

$$\vec{H}_s = \frac{1}{4\pi} \int_s \left[-ik \hat{n} \times \vec{E} \frac{e^{ikr}}{r} + (\hat{n} \times \vec{H}) \times \nabla \frac{e^{ikr}}{r} + (\hat{n} \cdot \vec{H}) \nabla \frac{e^{ikr}}{r} \right] ds$$

where $k = 2\pi/\lambda$, r is the distance from the integration point to the field point, \vec{E} and \vec{H} are the total fields on s (sum of incident plus scattered fields) and s is an arbitrary surface surrounding the scatterer. Generally it is simplest to take the arbitrary surface to be the scattering surface itself. Then if the scatterer is a perfect conductor we will have $\hat{n} \times \vec{E} = \hat{n} \cdot \vec{H} = 0$ so that Equation (A.1-10) becomes:

$$\vec{E}_s = \frac{1}{4\pi} \int_s \left[ik \hat{n} \times \vec{H} \frac{e^{ikr}}{r} + (\hat{n} \cdot \vec{E}) \nabla \frac{e^{ikr}}{r} \right] ds \quad (\text{A.1-11})$$

$$\vec{H}_s = \frac{1}{4\pi} \int_s (\hat{n} \times \vec{H}) \times \nabla \frac{e^{ikr}}{r} ds$$

A.1.6 Physical Optics and Geometric Optics

Both Equations (A.1-10) and (A.1-11) are exact if the correct values

¹Gaussian units are employed in this appendix.

of \vec{E} and \vec{H} are used in the integrals. Since the correct values are not known we must use approximate values and in this way we get approximate answers. In addition to using approximate values of \vec{E} and \vec{H} in the integrals we may use an approximate method (such as stationary phase) to evaluate the integrals approximately for short wavelengths. When geometric optics is used to determine approximate values of \vec{E} and \vec{H} in the integrands the approximation obtained is called physical optics. We will consider other approximations for \vec{E} and \vec{H} in calculating the cross-sections of certain configurations later on but for now we will consider only physical optics.

For the monostatic cross-section, physical optics (based on Equation (A.1-11)) gives:

$$\sigma = \sigma_e = \frac{4\pi}{\lambda^2} |g|^2 \quad (\text{A.1-12})$$

$$g = \int e^{2ik\rho} \frac{dA}{d\rho} d\rho$$

(Ref. A3), where ρ is distance measured in the direction of incidence and A is the area of the projection of the part of the scatterer to one side of a plane of constant ρ (the side indicated by arrows in Figure A-3), the

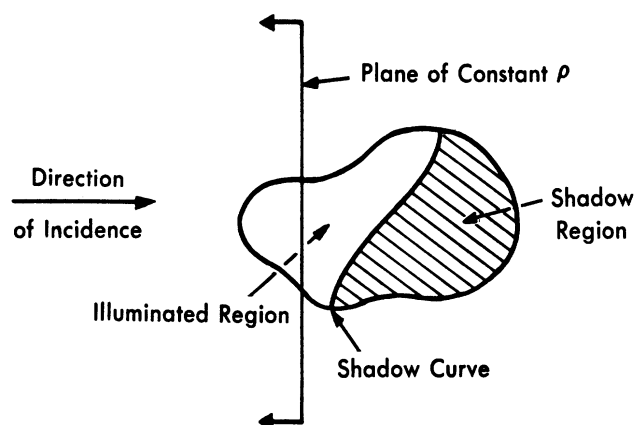


FIG. A-3

projection being made onto the plane of constant ρ . From Equation (A.1-12) we see that physical optics predicts no dependence of monostatic cross-section on polarization (at least the form of physical optics which we are using here). Equation (A.1-12) may be interpreted as saying that each element of area makes a contribution to g , but with a phase factor $e^{2ik\rho}$ so that two contributions may either add or cancel depending on their relative phases.

We will now give a brief introduction to the evaluation of Equation (A.1-12). We will then give a table of cross-section formulas.

As an introduction to physical optics we will consider the cross-section of a sphere. For the sphere in Figure A-4 the area function is

$$A = \begin{cases} 0 & (\rho \leq -a) \\ \pi(a^2 - \rho^2) & (-a \leq \rho \leq 0) \\ \pi a^2 & (0 \leq \rho) \end{cases} \quad (\text{A.1-13})$$

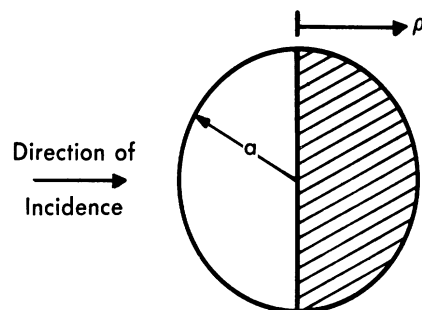


FIG. A-4

From Equation (A.1-13) we find:

$$\frac{dA}{d\rho} = \begin{cases} 0 & (\rho \leq -a) \\ -2\pi\rho & (-a \leq \rho \leq 0) \\ 0 & (0 \leq \rho) \end{cases} \quad (\text{A.1-14})$$

The variation of A and $dA/d\rho$ with ρ is shown in Figure A-5.

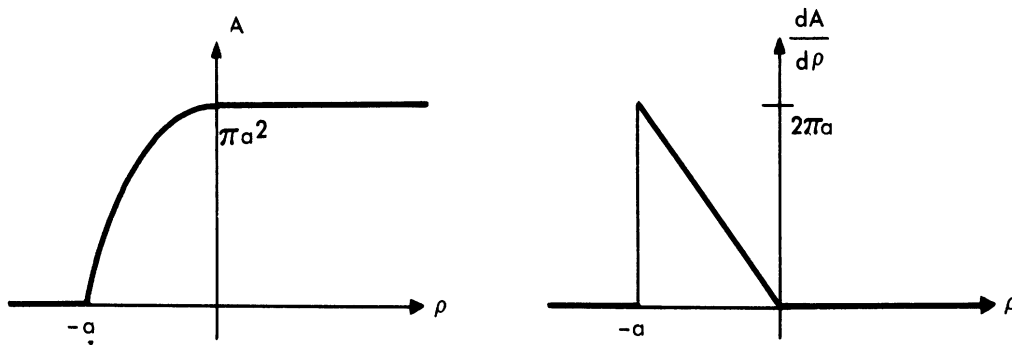


FIG. A-5

For short wavelengths k is large and $e^{2ik\rho}$ oscillates very rapidly (that is its real and imaginary parts oscillate very rapidly). As a result, whenever $dA/d\rho$ varies slowly the contributions for values of ρ differing by $\lambda/4$ will nearly cancel. Only the regions where $dA/d\rho$ changes rapidly will contribute appreciably to the integral. From Figure A-5 it is clear that the main contribution comes from $\rho = -a$. For this particular problem the integral can be evaluated exactly; so, let us see whether the above ideas jibe with the exact evaluation. We have

$$g = \int_{-a}^0 e^{2ik\rho} (-2\pi\rho) d\rho = \frac{\pi ia}{k} e^{-2ika} + \frac{\pi}{2k^2} (e^{-2ika} - 1) \quad (\text{A.1-15})$$

The terms having an e^{-2ika} factor can be interpreted as the contribution from $\rho = a$, while the term not having such a phase factor can be interpreted as the contribution from $\rho = 0$. With this interpretation we see that the contributions from the intermediate region have cancelled each other out. For large k the term, $\frac{\pi ia}{k} e^{-2ika}$ dominates the others. This term is due to the jump in $dA/d\rho$ at $\rho = -a$. The other two terms are due to the discontinuity in $\frac{d^2A}{d\rho^2}$ at $\rho = -a$ and at $\rho = 0$. According to the

interpretation used here we should find that another area function for which $dA/d\rho$ has a jump of $2\pi a$ at $\rho = -a$ but is otherwise continuous (varying but little in a distance of a wavelength) should give the same result (for large k). For example suppose that (Fig. A-6)

$$A = \begin{cases} 0 & (\rho < -a) \\ \frac{2\pi a}{\beta} [1 - e^{-\beta(\rho+a)}] & (\rho \geq -a) \end{cases}, \quad \text{and} \quad \frac{dA}{d\rho} = \begin{cases} 0 & (\rho < -a) \\ 2\pi a e^{-\beta(\rho+a)} & (\rho \geq -a) \end{cases}. \quad (\text{A. 1-16})$$

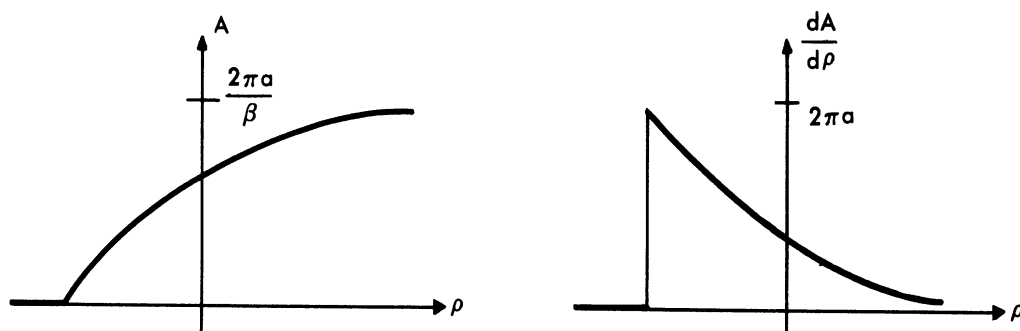


FIG. A-6

We can again evaluate g exactly with the result

$$g = \int_{-a}^{\infty} e^{2ik\rho} 2\pi a e^{-\beta(\rho+a)} d\rho = \frac{\pi i a}{k + \frac{\beta i}{2}} e^{-2ika} \quad (\text{A. 1-17})$$

For large k Equations (A. 1-15) and (A. 1-17) are in agreement so that the interpretation which we have been using seems to be accurate.

There is another way of looking at the physical optics integral which can be very illuminating. If, for the sphere problem, we let

$$f(\rho) = \int_{-a}^{\rho} e^{2ikz} (-2\pi z) dz, \quad \text{then} \quad g = f(0).$$

Now $f(\rho)$ is a complex number and as ρ varies from $-a$ to 0 , $f(\rho)$

traces out a curve in the complex plane. This curve is called a vibration curve. The vibration curve is the limiting form of a vibration polygon obtained by replacing the integral in Equation (A.1-12) by an approximating sum $\sum_n e^{2ikz_n} \left(\frac{dA}{dz}\right)_n \Delta z_n$. The individual terms in this series can be

looked on as little vectors in the complex plane which add up as shown in Figure A-7. The magnitude of each vector is $\left(\frac{dA}{dz}\right)_n \Delta z_n$, and the vector

points in a direction making an angle $2kz_n$ with the real axis. If we take a constant value of Δz_n then the angle which the resultant vectors make with the real axis will increase steadily. If $\frac{dA}{dz}$ is constant then the vectors

will go around a circle of radius $\frac{1}{2k} \left|\frac{dA}{dz}\right|$. If $\frac{dA}{dz}$ varies slowly then the vibration curve will spiral about a relatively fixed point with a slowly changing radius. However each time $\frac{dA}{dz}$ has a discontinuity the point about which the vibration curve is spiraling will jump proportionately. For the sphere, the vibration curve will appear roughly as in Figure A-8. It can be seen that the spiral ends up at approximately the original center of curvature which is $\frac{\pi ia}{k} e^{-2ika}$. As a second example of a vibration curve, let us take an area function for which $\frac{dA}{dz}$ has two jump discontinuities as

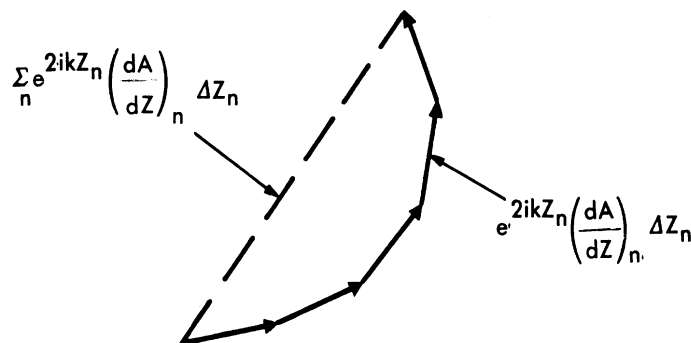


FIG. A-7

shown in Figure A-9. In this case the vibration curve will take the form shown in Figure A-10. This can be analyzed as follows: at $\rho = 0$ the center of the vibration spiral is shifted out to the point A (Fig. A-11) and the spiral follows the large circle.

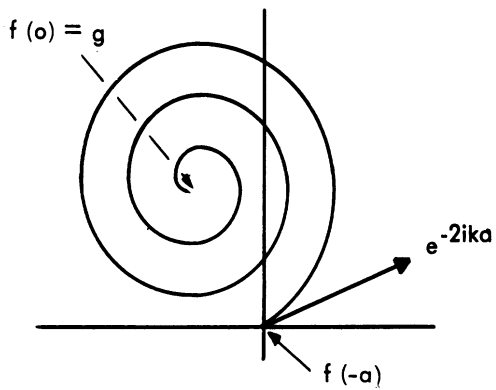


FIG. A-8

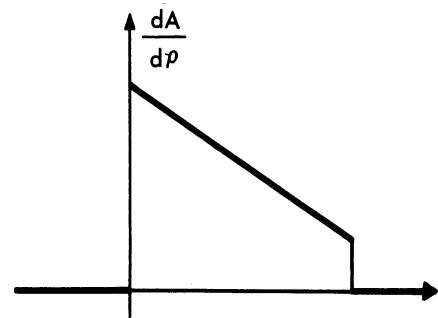


FIG. A-9

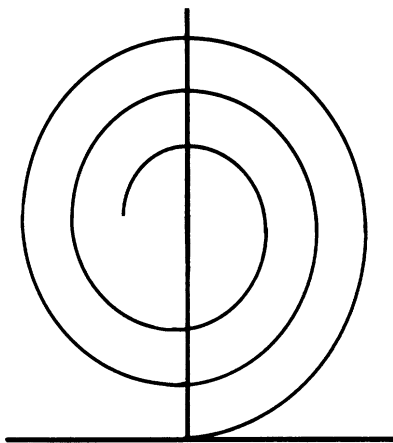


FIG. A-10

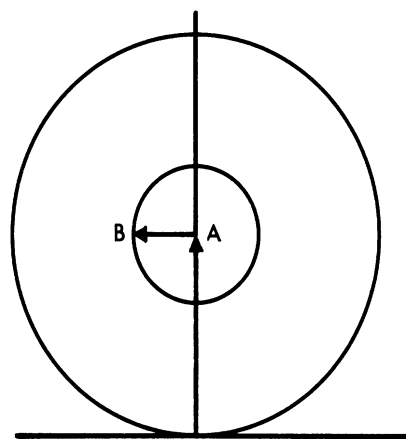


FIG. A-11

The radius of the circle slowly decreases till the spiral is following the small circle. At the second discontinuity the center is again shifted, this time to the point B. The center of the spiral ends up at the same place as the spiral itself. Thus by tracing the motion of the center of the spiral we can find the value of the integral. In more complicated cases this can be quite a useful aid to our thinking.

If $\frac{dA}{d\rho}$ behaves in the same manner for two bodies then the physical optics cross-section for the two bodies will be nearly equal. We have seen that bodies like the sphere which have finite radii of curvature will have a $\frac{dA}{d\rho}$ which has a jump where the incident field first hits the body and then goes smoothly to zero. At the point at which the incident wave first hits such a smooth body we can approximate the body by a paraboloid having the same principle radii of curvature. Once we have found the cross-section for such a paraboloid we will have an approximate cross-section for all such smooth bodies. We take the equation of the paraboloid (Fig. A-12) to be

$$\rho = \frac{x^2}{2R_1} + \frac{y^2}{2R_2} \quad (\text{A.1-18})$$

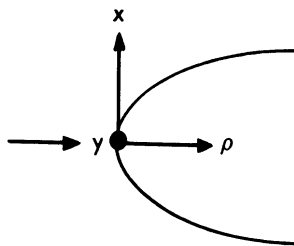


FIG. A-12

where R_1 and R_2 are the principle radii of curvature at the point $(0, 0, 0)$ where the incident wave first hits the paraboloid. The area function is

$A = 2\pi\rho\sqrt{R_1 R_2}$ ($\rho \geq 0$). Thus $\frac{dA}{d\rho} = 2\pi\sqrt{R_1 R_2}$ ($\rho \geq 0$). This does not go to zero for large ρ but we can modify the body very slightly so that $\frac{dA}{d\rho} = 2\pi\sqrt{R_1 R_2} e^{-\beta\rho}$ ($\rho \geq 0$) where β is very small. We then have

$$g = \int_0^{\infty} e^{2ik\rho} 2\pi\sqrt{R_1 R_2} e^{-\beta\rho} d\rho \xrightarrow{\beta \rightarrow 0} \frac{\pi i \sqrt{R_1 R_2}}{k} \quad (\text{A. 1-19})$$

Substitution of Equation (A. 1-19) into Equation (A. 1-12) shows that the approximate cross-section of a smooth body is

$$\sigma = \pi R_1 R_2 \quad (\text{A. 1-20})$$

where R_1 and R_2 are the principle radii of curvature at the specular reflection point. This formula was obtained by assuming k large so that the return was essentially from the specular reflection point. Hence the same result could be obtained alternatively by using geometric-optics. As a result this formula for σ is often called the geometric-optics formula for σ .

Equation (A. 1-20) is one of the most useful cross-section formulas due to its extreme simplicity. It is convenient for applications to have a few formulas giving R_1 and R_2 .

If the equation of the surface is given in the form $z = f(x, y)$ then

$$R_1 R_2 = \frac{(1 + f_x^2 + f_y^2)^2}{f_{xx} f_{yy} - f_{xy}^2} \quad (\text{A. 1-21})$$

If the equation of the surface is given in the form $F(x, y, z) = 0$, then

$$R_1 R_2 = \frac{(F_x^2 + F_y^2 + F_z^2)^2}{\Delta} \quad (\text{A. 1-22})$$

$$\Delta = - \begin{vmatrix} F_{xx} & F_{xy} & F_{xz} & F_x \\ F_{xy} & F_{yy} & F_{yz} & F_y \\ F_{xz} & F_{yz} & F_{zz} & F_z \\ F_x & F_y & F_z & 0 \end{vmatrix}$$

If the equation of the surface is given parametrically as $x = x(u, v)$, $y = y(u, v)$, $z = z(u, v)$ then

$$R_1 R_2 = \frac{(EG - F^2)^2}{LN - M^2} \quad (\text{A. 1-23})$$

$$E = x_u^2 + y_u^2 + z_u^2 \quad F = x_u x_v + y_u y_v + z_u z_v \quad G = x_v^2 + y_v^2 + z_v^2$$

$$L = \begin{vmatrix} x_{uu} & x_u & x_v \\ y_{uu} & y_u & y_v \\ z_{uu} & z_u & z_v \end{vmatrix} \quad M = \begin{vmatrix} x_{uv} & x_u & x_v \\ y_{uv} & y_u & y_v \\ z_{uv} & z_u & z_v \end{vmatrix} \quad N = \begin{vmatrix} x_{vv} & x_u & x_v \\ y_{vv} & y_u & y_v \\ z_{vv} & z_u & z_v \end{vmatrix}$$

For a body of revolution given by the equation $\rho = \rho(z)$ (Fig. A-13) we have

$$R_1 R_2 = \left| \frac{\rho}{\rho'' \sin^4 \alpha} \right| \quad (\text{A. 1-24})$$

where α is the angle between the direction of incidence and the axis of the body. ρ and ρ'' must, of course, be evaluated at the specular reflection point.

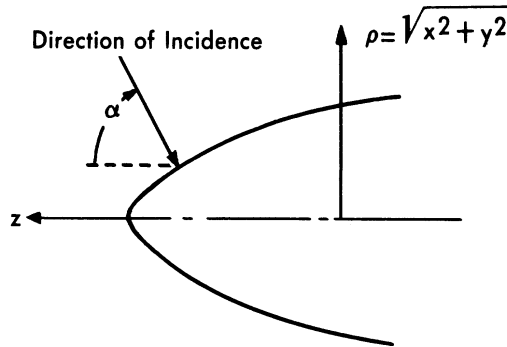


FIG. A-13

A. 1.7 Widths of Peaks

In many of the formulas given in the list of cross-section formulas (Section A. 3) there is one expression for "normal" incidence and a second expression for "non-normal" incidence. This situation was illustrated in Equation (A. 1-5). In these cases the cross-section for short wavelengths is much larger at normal incidence than at non-normal incidence. When the cross-section can be neglected, except at nearly normal incidence, we might use, instead of the non-normal incidence formula, a formula giving the width of the peak.

As an example, consider the elliptic cylinder, Equations (A. 3-9 and A. 3-10). If we require that the sum of the two non-normal components be half as large as the normal incidence cross-section, then we find that θ must satisfy the equation

$$\frac{2\lambda a^2 b^2 \sin^2 \theta}{8\pi \cos^2 \theta [a^2 \cos^2 \phi + b^2 \sin^2 \phi]^{3/2}} = \frac{2\pi L a^2 b^2}{2\lambda [a^2 \cos^2 \phi + b^2 \sin^2 \phi]^{3/2}} \quad (A. 1-25)$$

We use $\theta_{\frac{1}{2}}$ to indicate a solution to Equation (A. 1-25). For small λ we have (for the elliptic cylinder):

$$\theta_{\frac{1}{2}} = \frac{\pi}{2} \pm \frac{\lambda}{2\pi L} \quad (\text{A. 1-26})$$

Equation (A. 1-26) also holds for the tapered wedge aside from the fact that a different coordinate system was used there (see Fig. A-35). In terms of the tapered wedge coordinate system

$$\sin \theta_{\frac{1}{2}} = \frac{\lambda}{2\pi L \sin \phi} \quad (\text{A. 1-27})$$

By the same technique the half-power angles for the elliptic and circular cones are found to be

$$\theta_{\frac{1}{2}} = \tan^{-1} \left(\frac{-\eta}{\tan \alpha \sqrt{\sin^2 \phi + \eta^2 \cos^2 \phi}} \right) \pm \frac{3\lambda \sqrt{L_1 + L_2} \eta}{4\sqrt{2} \pi \left(L_2^{3/2} - L_1^{3/2} \right) \sqrt{\eta^2 + \tan^2 \alpha (\sin^2 \phi + \eta^2 \cos^2 \phi)}} \quad (\text{A. 1-28})$$

and
$$\theta_{\frac{1}{2}} = \frac{\pi}{2} + \alpha \pm \frac{3\lambda \sqrt{L_1 + L_2} \cos \alpha}{4\sqrt{2} \pi \left(L_2^{3/2} - L_1^{3/2} \right)}$$

respectively. For the torus the half-power angle is found to be

$$\theta_{\frac{1}{2}} = \frac{\lambda}{2\pi^2 b} \quad (\text{A. 1-29})$$

A. 1.8 Shadowing

When one body is in the shadow of another body it might be supposed that it would scatter as if it had a hole cut out with the shape of the shadow. This is not so. If the sphere of radius b in Figure A-14 were to scatter as if it had a hole the shape of the shadow cast on it by the sphere of radius a then we could use the truncated ogive formulas, Equations (A. 3-25 and A. 3-28) to calculate its contribution. The angle α in Equation (A. 3-25) would be given by $\alpha = \frac{\pi}{2} - \sin^{-1} \frac{a}{b}$ so that $\tan^2 \alpha = \frac{b^2 - a^2}{a^2}$. The contribution which the second sphere (of radius b) would

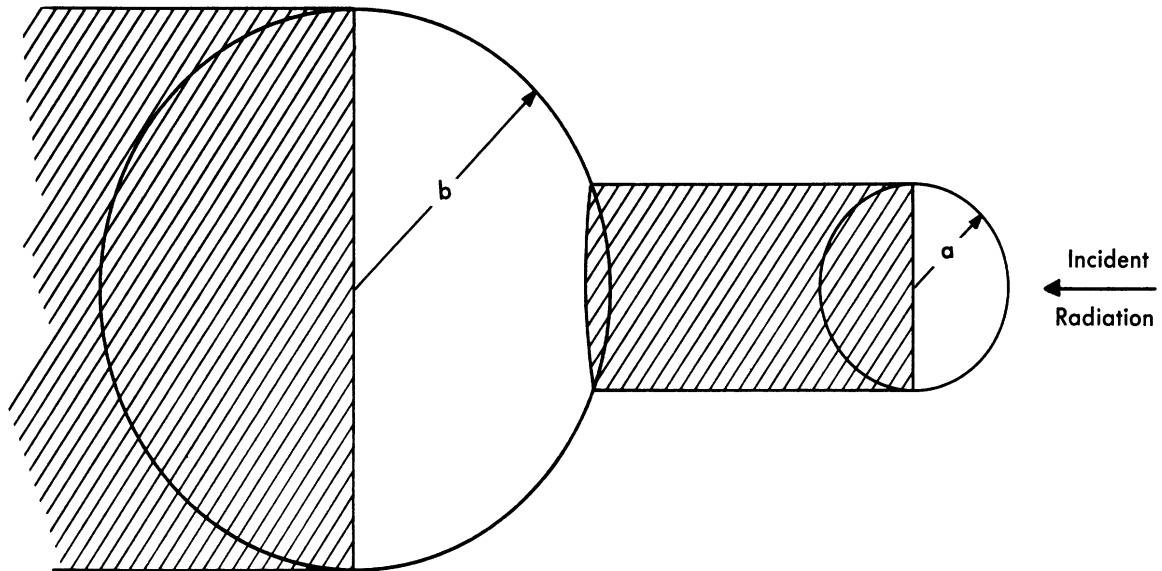


FIG. A-14

make according to this approach is $\pi a^2 \tan^2 \alpha + \pi a^2 = \pi b^2$. Actually the true contribution will be very much smaller. The reason for the discrepancy is that the shadow which has been drawn as very sharp in Figure A-14, is quite diffuse. The lack of sharpness in the shadow curve prevents a sudden jump in the radius of the vibration curve (see Fig. A-7 and A-8) of the type which is obtained for a truncated ogive viewed nose-on. The result is that the contribution of the sphere of radius b in Figure A-14 can be neglected. On the other hand if the incident radiation could hit the sphere of radius b at normal incidence as in Figure A-15, then the sphere of radius b would give a contribution of πb^2 to the cross-section. The final conclusion is that the cross-section of a partially shadowed component is unchanged unless the part of the body which contributes to the cross-section, that is the part of the body which the incident radiation hits at normal incidence, is shadowed. However, if the specularly reflecting part of the body is shadowed then the body no longer contributes within the accuracy of the present theory.

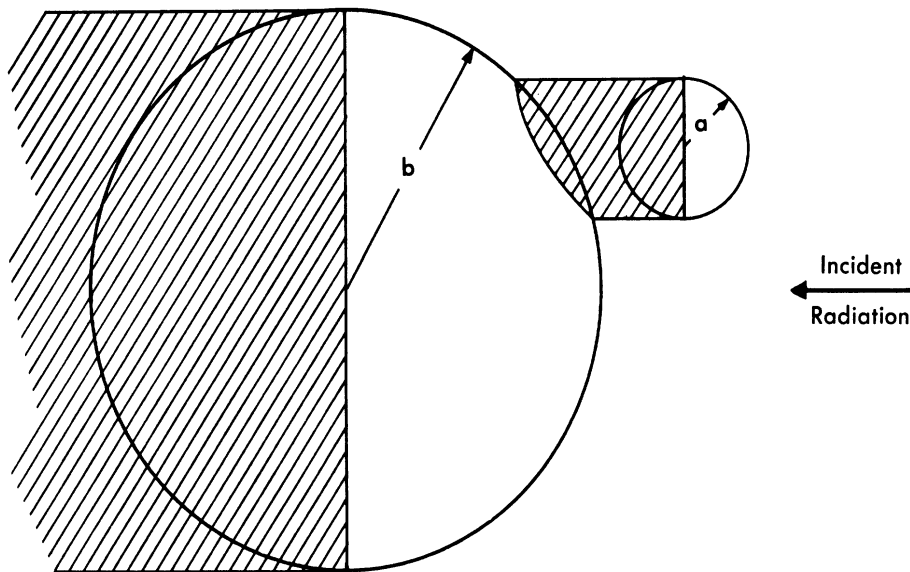


FIG. A-15

Another result of the lack of distinctness of the shadow boundary is that the contribution to the physical optics integral coming from the shadow curve can almost always be neglected. This is important in obtaining the cross-section of an ogive for aspects near nose-on (Ref. A4, pp. 28, 72, 73, 74).

A. 1. 9 Change of Coordinate System

A. 1. 9. 1 General Transformation

The various coordinates used in describing the bodies in the list of cross-section formulas will seldom coincide with the coordinate system used to describe the over-all aircraft. The unit radius vector to the transmitter receiver in the aircraft coordinate system will be taken in the remainder of this appendix to be $\hat{r} = \cos \phi^* \sin \theta^* \hat{i} + \sin \phi^* \sin \theta^* \hat{j} + \cos \theta^* \hat{k}$. In the coordinate system used to describe the particular component in question the unit radius vector will be taken to be $\hat{r}' = \cos \phi \sin \theta \hat{i}' + \sin \phi \sin \theta \hat{j}' + \cos \theta \hat{k}'$. The polar angles θ^* and ϕ^* in the aircraft system can be

expressed in terms of the polar angles θ and ϕ in the component system as follows:

$$\cos \theta^* = a_{31} \sin \theta \cos \phi + a_{32} \sin \theta \sin \phi + a_{33} \cos \theta \tag{A.1-30}$$

$$\tan \phi^* = \frac{a_{21} \sin \theta \cos \phi + a_{22} \sin \theta \sin \phi + a_{23} \cos \theta}{a_{11} \sin \theta \cos \phi + a_{12} \sin \theta \sin \phi + a_{13} \cos \theta}$$

where $a_{11} = \hat{i} \cdot \hat{i}'$, $a_{21} = \hat{j} \cdot \hat{i}'$, $a_{12} = \hat{i} \cdot \hat{j}'$, etc. \hat{i} , \hat{j} , and \hat{k} are unit vectors along the x, y, and z axes in the aircraft system, and \hat{i}' , \hat{j}' , and \hat{k}' are the unit vectors for the component coordinate system. Equation (A.1-30) may simplify considerably for some cases of interest. Some special cases will now be tabulated.

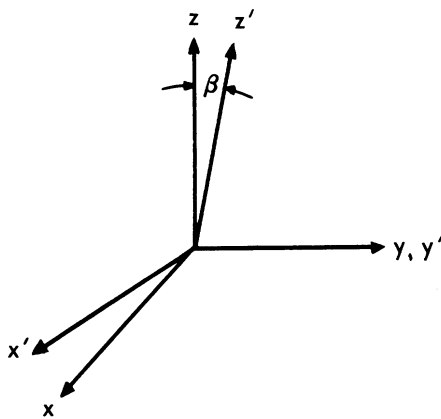


FIG. A-16

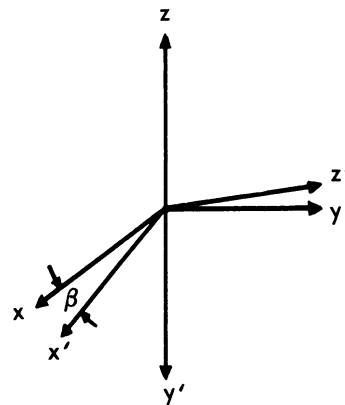


FIG. A-17

$$\sin \theta^* = \sqrt{\cos^2 \beta \sin^2 \theta - \frac{1}{2} \sin 2\beta \sin 2\theta \cos \phi + \sin^2 \beta (1 - \sin^2 \theta \cos^2 \phi)}$$

$$\cos \theta^* = \cos \beta \cos \theta + \sin \beta \sin \theta \cos \phi$$

(A.1-31)

$$\sin \phi^* = \frac{\sin \phi}{\sqrt{\cos^2 \beta \cos^2 \phi + \sin^2 \phi - \sin 2\beta \cot \theta \cos \phi + \sin^2 \beta \cot^2 \theta}}$$

$$\cos \phi^* = \frac{\cos \beta \cos \phi - \sin \beta \cot \theta}{\sqrt{\cos^2 \beta \cos^2 \phi + \sin^2 \phi - \sin 2\beta \cot \theta \cos \phi + \sin^2 \beta \cot^2 \theta}}$$

The formulas giving sin and cos of θ and ϕ in terms of θ^* and ϕ^* are the same as Equation (A.1-31) except that β is replaced by $-\beta$.

$$\sin \theta^* = \sqrt{1 - \sin^2 \theta \sin^2 \phi}$$

$$\cos \theta^* = -\sin \theta \sin \phi$$

$$\sin \phi^* = \frac{\cos \beta \cos \theta + \sin \beta \sin \theta \cos \phi}{\sqrt{1 - \sin^2 \theta \sin^2 \phi}}$$

$$\cos \phi^* = \frac{\cos \beta \sin \theta \cos \phi - \sin \beta \cos \theta}{\sqrt{1 - \sin^2 \theta \sin^2 \phi}} \quad (\text{A.1-32})$$

$$\cos \theta = \sin \theta^* \sin(\phi^* - \beta)$$

$$\sin \theta = \sqrt{1 - \sin^2 \theta^* \sin^2(\phi^* - \beta)}$$

$$\sin \phi = -\frac{\cos \theta^*}{\sqrt{1 - \sin^2 \theta^* \sin^2(\phi^* - \beta)}}$$

$$\cos \phi = \frac{\sin \theta^* \cos(\phi^* - \beta)}{\sqrt{1 - \sin^2 \theta^* \sin^2(\phi^* - \beta)}} \quad (\text{A.1-33})$$

A.1.9.2 Coordinate Transformation as Used in the Application of the Truncated Elliptic Cone to Wing and Elevator Surfaces

When the formula for the truncated elliptic cone is applied to wing surfaces there is a complicated coordinate transformation required to go from the coordinate system used to describe the over-all aircraft to the coordinate system used to describe the cone. The purpose of this section is to get the formulas in a simple form in the aircraft coordinate system.

In the aircraft coordinate system the direction to the transmitter-receiver is given by the polar angles θ^* and ϕ^* (Fig. A-18). Since the radar will usually be beneath the aircraft, θ^* will usually be greater than 90° .

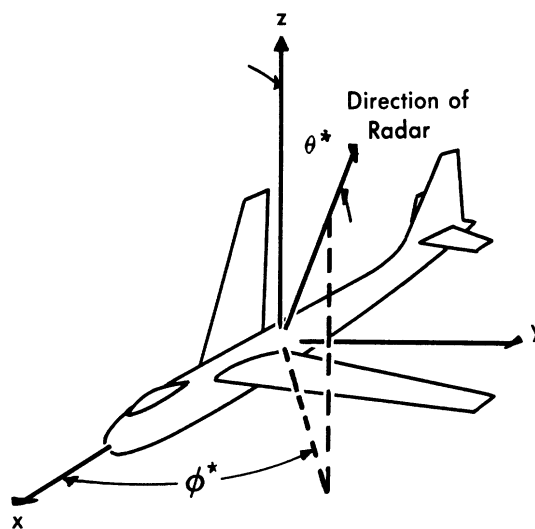


FIG. A-18

The orientation of the cone to be used in simulating the wing of the aircraft can be determined from the three views of the aircraft. The angles; the sweepback angle, ψ , the angle of droop, δ , and the angle of attack, α ; are shown in Figure A-19. These angles determine the orientation of the cone. The sweepback angle, ψ , is taken to be the angle be-

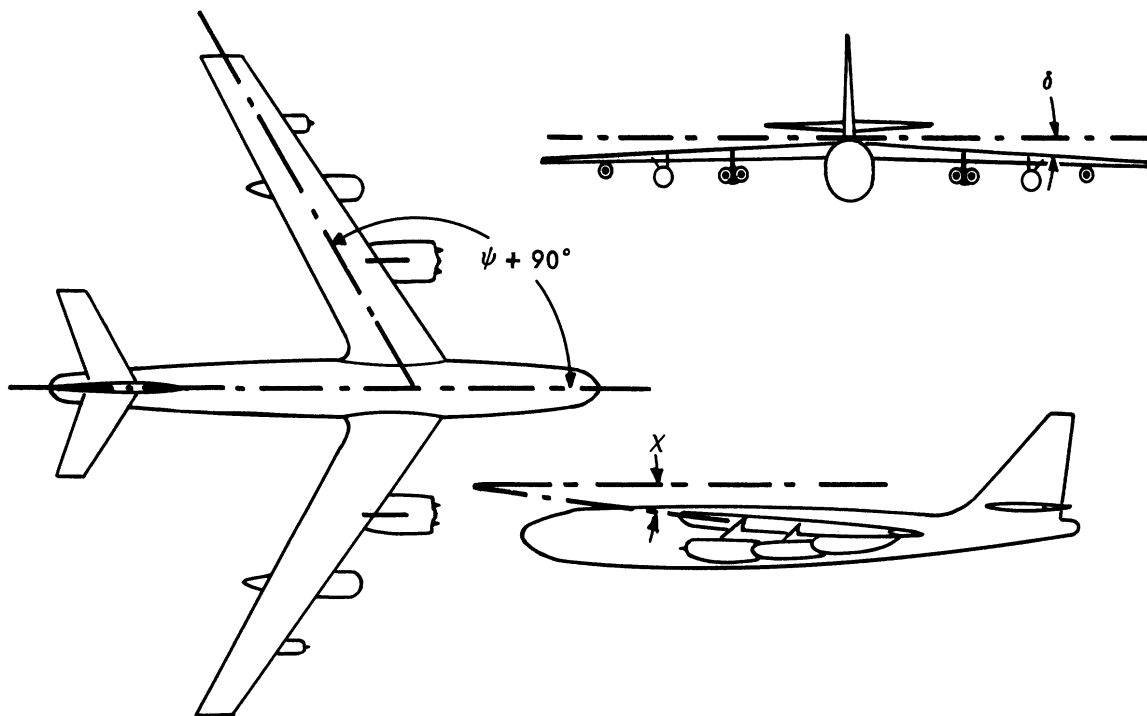


FIG. A-19

tween the projection of the axis of the cone on a horizontal plane (x-y plane in Figure A-18) and the axis of the aircraft. The angle of droop, δ , is taken to be the angle between the projection of the axis of the cone on y-z plane (Fig. A-18) and the y-axis. The angle of attack, χ , is taken to be the angle between the projection of the leading edge of the cone on the x-z plane and the x-axis (Fig. A-18). The leading edge of the cone is the intersection of the cone with the plane containing the axis of the cone and the major axis of one of the elliptical cross-sections of the cone.

It will be assumed throughout that δ , χ , and α (the half-cone angle, defined in Section A.3.2.1) are all small angles. We will obtain approximate expressions for the transformations between the two coordinate systems first.

The coordinates in the aircraft system will be called x, y, z, with unit vectors \hat{i} , \hat{j} , \hat{k} and polar angles θ^* and ϕ^* . The coordinates in the cone system will be called x', y', z' with unit vectors \hat{i}' , \hat{j}' , \hat{k}' and polar angles θ and ϕ . The transformation between coordinates is

$$\begin{aligned}\hat{i}' &= a_{11}\hat{i} + a_{21}\hat{j} + a_{31}\hat{k} \\ \hat{j}' &= a_{12}\hat{i} + a_{22}\hat{j} + a_{32}\hat{k} \\ \hat{k}' &= a_{13}\hat{i} + a_{23}\hat{j} + a_{33}\hat{k}\end{aligned}\tag{A.1-34}$$

Under the assumption that δ , χ , and α are all small quantities of the first order we can write Equation (A.1-34) in the form (see Eq. A.1-33):

$$\begin{aligned}\hat{i}' &= (\cos \psi + \eta_{11})\hat{i} + (\sin \psi + \eta_{21})\hat{j} + \epsilon_{31}\hat{k} \\ \hat{j}' &= \epsilon_{12}\hat{i} + \epsilon_{22}\hat{j} + (1 + \eta_{32})\hat{k} \\ \hat{k}' &= (\sin \psi + \eta_{13})\hat{i} + (-\cos \psi + \eta_{23})\hat{j} + \epsilon_{33}\hat{k}\end{aligned}\tag{A.1-35}$$

where the ϵ 's are small quantities of the first order, and the η 's are small quantities of the second order.

From the definition of δ we have

$$\begin{aligned}
 \cos \delta &= -\frac{\hat{j} \cdot \hat{k}'}{|\hat{k}' - (\hat{i} \cdot \hat{k}')\hat{i}|} = -\frac{a_{23}}{\sqrt{a_{23}^2 + a_{33}^2}} \\
 &= \frac{\cos \psi - \eta_{23}}{\sqrt{\cos^2 \psi - 2\eta_{23} \cos \psi + \eta_{23}^2 + \epsilon_{33}^2}} \\
 &= 1 - \frac{1}{2} \frac{\epsilon_{33}^2}{\cos^2 \psi} + \dots
 \end{aligned}
 \tag{A.1-36}$$

where the next term is of order four.

The value of ϵ_{33} is found from Equation (A.1-36) to be

$$\epsilon_{33} = \delta \cos \psi + \dots
 \tag{A.1-37}$$

to (not including) terms of third order.

The definition of ψ gives

$$\cos \psi = -\frac{a_{23}}{\sqrt{a_{13}^2 + a_{23}^2}} = \frac{\cos \psi - \eta_{23}}{\sqrt{1 + 2\eta_{13} \sin \psi - 2\eta_{23} \cos \psi}} + \dots$$

or

$$\eta_{13} \cos \psi = -\eta_{23} \sin \psi + \dots$$

The condition $a_{13}^2 + a_{23}^2 + a_{33}^2 = 1$ gives

$$2\eta_{13} \sin \psi - 2\eta_{23} \cos \psi + \epsilon_{33}^2 + \dots = 0
 \tag{A.1-39}$$

Combination of Equations (A.1-37), (A.1-38), and (A.1-39) gives

$$\hat{k}' = \sin \psi \cos(\delta \cos \psi) \hat{i}' - \cos \psi \cos(\delta \cos \psi) \hat{j}' + \sin(\delta \cos \psi) \hat{k}' \quad (\text{A.1-40})$$

up to terms of order three.

The definition of χ gives

$$\begin{aligned} \cos \chi &= \frac{a_{11} \cos \alpha + a_{13} \sin \alpha}{\sqrt{(a_{11} \cos \alpha + a_{13} \sin \alpha)^2 + (a_{31} \cos \alpha + a_{33} \sin \alpha)^2}} \\ &= \frac{1 + \alpha \tan \psi + \frac{\eta_{11}}{\cos \psi} - \frac{\alpha^2}{2}}{\sqrt{1 + 2\alpha \tan \psi + 2 \frac{\eta_{11}}{\cos \psi} - \alpha^2 + \alpha^2 \tan^2 \psi + \frac{\epsilon_{31}^2}{\cos^2 \psi}}} + \dots \\ &= 1 - \frac{1}{2} \frac{\epsilon_{31}^2}{\cos^2 \psi} + \dots \end{aligned} \quad (\text{A.1-41})$$

up to terms of order four. Thus, up to terms of order three, we have

$$\epsilon_{31} = \chi \cos \psi + \dots \quad (\text{A.1-42})$$

The values of η_{11} and η_{21} can be obtained by using the conditions $\hat{i}' \cdot \hat{k}' = 0$ and $\hat{i}' \cdot \hat{i}' = 1$ with the result

$$\begin{aligned} \hat{i}' &= \left[\cos \psi \cos(\chi \cos \psi) - \sin \psi \sin(\delta \cos \psi) \sin(\chi \cos \psi) \right] \hat{i}' \\ &+ \left[\sin \psi \cos(\chi \cos \psi) + \cos \psi \sin(\delta \cos \psi) \sin(\chi \cos \psi) \right] \hat{j}' + \sin(\chi \cos \psi) \hat{k}' \end{aligned} \quad (\text{A.1-43})$$

up to terms of order three.

The relation $\hat{j}' = \hat{k}' \times \hat{i}'$ yields

$$\begin{aligned} \hat{j}' = & \left[-\cos \psi \sin(\chi \cos \psi) - \sin \psi \sin(\delta \cos \psi) \right] \hat{i} \\ & + \left[\cos \psi \sin(\delta \cos \psi) - \sin \psi \sin(\chi \cos \psi) \right] \hat{j} + \cos(\chi \cos \psi) \cos(\delta \cos \psi) \hat{k} \end{aligned} \quad (\text{A. 1-44})$$

up to terms of order three.

From the transformation Equations (A. 1-40), (A. 1-43), and (A. 1-44) we find

$$\begin{aligned} \cos \theta &= a_{13} \sin \theta^* \cos \phi^* + a_{23} \sin \theta^* \sin \phi^* + a_{33} \cos \theta^* \\ &= \sin \theta^* \sin(\psi - \phi^*) + \delta \cos \theta^* \cos \psi \end{aligned} \quad (\text{A. 1-45})$$

up to terms of order two and

$$\begin{aligned} \tan \phi &= \frac{a_{12} \sin \theta^* \cos \phi^* + a_{22} \sin \theta^* \sin \phi^* + a_{32} \cos \theta^*}{a_{11} \sin \theta^* \cos \phi^* + a_{21} \sin \theta^* \sin \phi^* + a_{31} \cos \theta^*} \\ &= \frac{\cos \theta^*}{\sin \theta^* \cos(\psi - \phi^*)} \end{aligned} \quad (\text{A. 1-46})$$

or

$$\sin^2 \phi = \frac{\cos^2 \theta^*}{1 - \sin^2 \theta^* \sin^2(\psi - \phi^*)} ; \quad \cos^2 \phi = \frac{\sin^2 \theta^* \cos^2(\psi - \phi^*)}{1 - \sin^2 \theta^* \sin^2(\psi - \phi^*)}$$

up to terms of order one.

A. 2 DERIVATION OF RADAR CROSS-SECTIONS FOR SIMPLE SHAPES

A. 2. 1 Ellipsoid

The equation of an ellipsoid can be taken to be $F(x, y, z) = 1/2 [(x/a)^2 + (y/b)^2 + (z/c)^2 - 1] = 0$. The cross-section is then given by Equations (A. 1-20) and (A. 1-22) as

$$\sigma = \frac{\pi \left(\frac{x^2}{a^4} + \frac{y^2}{b^4} + \frac{z^2}{c^4} \right)^2}{\Delta} \quad (\text{A. 2-1})$$

$$\Delta = - \begin{vmatrix} \frac{1}{a^2} & 0 & 0 & x \\ 0 & \frac{1}{b^2} & 0 & y \\ 0 & 0 & \frac{1}{c^2} & z \\ \frac{x}{a^2} & \frac{y}{b^2} & \frac{z}{c^2} & 0 \end{vmatrix} = \frac{1}{a^2 b^2 c^2}$$

The x, y, z in Equation (A. 2-1) are the coordinates of the specular reflection point. In order to make the formula convenient to use we must express x, y, and z in terms of the polar angles, θ and ϕ (Fig. A-26), which specify the direction of incidence. At the specular reflection point, the normal to the surface points toward the transmitter-receiver so that we have

$$\hat{n} = \frac{\frac{x}{a^2} \hat{i} + \frac{y}{b^2} \hat{j} + \frac{z}{c^2} \hat{k}}{\sqrt{\frac{x^2}{a^4} + \frac{y^2}{b^4} + \frac{z^2}{c^4}}} = \sin \theta \cos \phi \hat{i} + \sin \theta \sin \phi \hat{j} + \cos \theta \hat{k} \quad (\text{A. 2-2})$$

From these two expressions for \hat{n} plus the equation of the ellipsoid we can solve for x , y , and z in terms of θ and ϕ . It can be verified that the result is

$$\begin{aligned} \frac{x^2}{a^4} &= \frac{\sin^2 \theta \cos^2 \phi}{a^2 \sin^2 \theta \cos^2 \phi + b^2 \sin^2 \theta \sin^2 \phi + c^2 \cos^2 \theta} \\ \frac{y^2}{b^4} &= \frac{\sin^2 \theta \sin^2 \phi}{a^2 \sin^2 \theta \cos^2 \phi + b^2 \sin^2 \theta \sin^2 \phi + c^2 \cos^2 \theta} \\ \frac{z^2}{c^4} &= \frac{\cos^2 \theta}{a^2 \sin^2 \theta \cos^2 \phi + b^2 \sin^2 \theta \sin^2 \phi + c^2 \cos^2 \theta} \end{aligned} \quad (\text{A.2-3})$$

Substitution of Equation (A.2-3) into Equation (A.2-1) gives us finally

$$\sigma = \frac{\pi a^2 b^2 c^2}{(a^2 \sin^2 \theta \cos^2 \phi + b^2 \sin^2 \theta \sin^2 \phi + c^2 \cos^2 \theta)^2} \quad (\text{A.2-4})$$

A2.2 Truncated Elliptic Cone

The equation of the cone is taken to be (Fig. A-27)

$$\begin{aligned} x^2 + \eta^2 y^2 &= z^2 \tan^2 \alpha \\ \eta &= \frac{a}{b} \end{aligned} \quad (\text{A.2-5})$$

Equation (A.2-5) can be written in the parametric form

$$\begin{aligned} x &= z \tan \alpha \cos \phi_1 \\ y &= \frac{1}{\eta} z \tan \alpha \sin \phi_1 \\ z &= z \end{aligned} \quad (\text{A.2-6})$$

A small displacement on the surface can be written as

$$\begin{aligned} \vec{dr} &= dx \hat{i} + dy \hat{j} + dz \hat{k} = (\tan \alpha \cos \phi_1 \hat{i} + \frac{1}{\eta} \tan \alpha \sin \phi_1 \hat{j} + \hat{k}) dz \\ &\quad + (-\sin \phi_1 \hat{i} + \frac{1}{\eta} \cos \phi_1 \hat{j}) z \tan \alpha d\phi_1 \end{aligned} \quad (\text{A. 2-7})$$

The surface area element is (from Equation A. 2-7)

$$\begin{aligned} \vec{ds} &= [(-\sin \phi_1 \hat{i} + \frac{1}{\eta} \cos \phi_1 \hat{j}) z \tan \alpha d\phi_1] \times [(\tan \alpha \cos \phi_1 \hat{i} + \frac{1}{\eta} \tan \alpha \sin \phi_1 \hat{j} + \hat{k}) dz] \\ &= z \tan \alpha (\frac{\cos \phi_1}{\eta} \hat{i} + \sin \phi_1 \hat{j} - \frac{\tan \alpha}{\eta} \hat{k}) d\phi_1 dz \end{aligned} \quad (\text{A. 2-8})$$

The projection of this on the direction of incidence is

$$\begin{aligned} dA &= z \tan \alpha d\phi_1 dz (\frac{\cos \phi_1}{\eta} \hat{i} + \sin \phi_1 \hat{j} - \frac{\tan \alpha}{\eta} \hat{k}) \cdot (\sin \theta \cos \phi \hat{i} + \sin \theta \sin \phi \hat{j} \\ &\quad + \cos \theta \hat{k}) \\ &= z \tan \alpha d\phi_1 dz (\frac{1}{\eta} \sin \theta \cos \phi \cos \phi_1 + \sin \theta \sin \phi \sin \phi_1 - \frac{1}{\eta} \cos \theta \tan \alpha) \end{aligned} \quad (\text{A. 2-9})$$

where the polar angles θ and ϕ are shown in Figure A-26. The phase factor on the surface is

$$\begin{aligned} e^{2ik\rho} &= e^{-2ik(\sin \theta \cos \phi \hat{i} + \sin \theta \sin \phi \hat{j} + \cos \theta \hat{k}) \cdot (x \hat{i} + y \hat{j} + z \hat{k})} \\ &= e^{-2ikz(\sin \theta \cos \phi \tan \alpha \cos \phi_1 + \frac{1}{\eta} \sin \theta \sin \phi \tan \alpha \sin \phi_1 + \cos \theta)} \end{aligned} \quad (\text{A. 2-10})$$

The physical optics integral is $g = \int e^{2ik\rho} dA$. There is a stationary phase point at (the other stationary phase point is not on the illuminated side of the cone)

$$\begin{aligned} \frac{\partial}{\partial \phi_1} (\sin \theta \cos \phi \tan \alpha \cos \phi_1 + \frac{1}{\eta} \sin \theta \sin \phi \tan \alpha \sin \phi_1 + \cos \theta) \\ &= \sin \theta \tan \alpha (-\cos \phi \sin \phi_1 + \frac{1}{\eta} \sin \phi \cos \phi_1) = 0 \\ \text{or } \sin \phi_1 &= \frac{\sin \phi}{\sqrt{\sin^2 \phi + \eta^2 \cos^2 \phi}}; \cos \phi_1 = \frac{\eta \cos \phi}{\sqrt{\sin^2 \phi + \eta^2 \cos^2 \phi}} \end{aligned} \quad (\text{A. 2-11})$$

Evaluation of the integration with respect to ϕ_1 by the method of stationary phase gives

$$g \approx \int_{L_1}^{L_2} \sqrt{\frac{\pi \eta z \tan \alpha}{k \sin \theta \sqrt{\sin^2 \phi + \eta^2 \cos^2 \phi}} \left(\frac{\sin \theta}{\sqrt{\sin^2 \phi + \eta^2 \cos^2 \phi}} - \frac{1}{\eta} \cos \theta \tan \alpha \right)} e^{-2ikz \left(\frac{1}{\eta} \sin \theta \tan \alpha \sqrt{\sin^2 \phi + \eta^2 \cos^2 \phi} + \cos \theta \right) - \frac{\pi i}{4}} dz \quad (\text{A. 2-12})$$

Unless the factor $\frac{1}{\eta} \sin \theta \tan \alpha \sqrt{\sin^2 \phi + \eta^2 \cos^2 \phi} + \cos \theta$ is nearly zero (normal incidence) we may integrate this by parts and neglect the new integral compared with the constant terms (this is a way of evaluating the two contributions which come from the points $z = L_1$ and $z = L_2$) to obtain

$$g \approx \left[\sqrt{\frac{\pi \eta z \tan \alpha}{k \sin \theta \sqrt{\sin^2 \phi + \eta^2 \cos^2 \phi}} \left(\frac{\sin \theta}{\sqrt{\sin^2 \phi + \eta^2 \cos^2 \phi}} - \frac{1}{\eta} \cos \theta \tan \alpha \right)} e^{-2ikz \left(\frac{1}{\eta} \sin \theta \tan \alpha \sqrt{\sin^2 \phi + \eta^2 \cos^2 \phi} + \cos \theta \right) - \frac{\pi i}{4}} \right]_{L_1}^{L_2} - 2ik \left(\frac{1}{\eta} \sin \theta \tan \alpha \sqrt{\sin^2 \phi + \eta^2 \cos^2 \phi} + \cos \theta \right) \Big|_{L_1}^{L_2} \quad (\text{A. 2-13})$$

Evaluation at the two limits gives the two contributions to the cross-section shown in Equation (A. 3-6). At normal incidence the phase factor is a constant and Equation (A. 2-12) integrates to give:

$$g \approx \frac{2(L_2^{3/2} - L_1^{3/2})}{3} \sqrt{\frac{\pi \eta \tan \alpha}{k \sin \theta \sqrt{\sin^2 \phi + \eta^2 \cos^2 \phi}} \left(\frac{\sin \theta}{\sqrt{\sin^2 \phi + \eta^2 \cos^2 \phi}} - \frac{1}{\eta} \cos \theta \tan \alpha \right)} \quad (\text{A. 2-14})$$

From (A. 2-14) the cross-section at normal incidence is found to be Equation (A. 3-4).

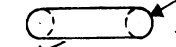
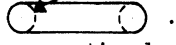
A. 2. 3 Torus

For off normal incidence the cross-section is obtained through the use of Equations (A. 1-20) and (A. 1-24). The equation of the torus (Fig. A-28) for use in Equation (A. 1-24) is

$$(\rho - b)^2 + z^2 = a^2 \quad (\text{A. 2-15})$$

From Equation (A. 2-15) we find $\rho'' = -\frac{a^2}{(\rho - b)^3}$. Substitution in Equation (A. 1-24) now yields

$$\sigma = \frac{\pi \rho (\rho - b)^3}{a^2 \sin^4 \theta} \quad (\text{A. 2-16})$$

Now there are two contributions to the cross-section. One when the incident field hits the outside of the torus , and one when the incident field hits the inside of the torus, . In the two cases we have $\rho = b + a \sin \theta$ and $\rho = b - a \sin \theta$ respectively. Substitution in Equation (A. 2-16) gives the two contributions listed in Equation (A. 3-22). The second contribution exists only if the inside of the torus is not shielded by the outside, or equivalently only when $a/(2b) < |\cos \theta| < 1$.

A. 2. 4 Truncated Ogive

For incidence along the z-axis it is clear that the contribution to the cross-section comes from the truncated end of this ogive. If we let

$$z = z_0 = \sqrt{(b - a)(b + a + 2[b \cos \alpha - a] \frac{1 + \cos \alpha}{\sin^2 \alpha})},$$

be the value of z at the truncation then near the truncation the equation of the ogive is approximately $\xi = a + (z_0 - z) \tan \alpha$. The physical optics integral is then approximately

$$g = - \int_{z_0}^{-\infty} e^{2ik(z_0 - z)} 2\pi [a + (z_0 - z) \tan \alpha] \tan \alpha dz$$

$$\approx \frac{\pi a \tan \alpha}{ik} \tag{A. 2-17}$$

Substitution of Equation (A. 2-17) into Equation (A. 1-12) gives Equation (A. 3-25).

Let $z_0 - z = z'$ (Fig. A-20). For $0 < \theta < \pi/2 - \alpha$ the major contribution to the cross-section will come from the neighborhood of $z' = 0$. As mentioned above near $z' = 0$ the equation of the ogive is approximately $\xi = a + z' \tan \alpha$. Due to the cylindrical symmetry we may assume without loss of generality that the transmitter-receiver moves only in the $x - z$ plane. The phase factor is

$$\begin{aligned} e^{2ik\xi} &= e^{2ik(z' \cos \theta - \xi \cos \phi_1 \sin \theta)} \\ &= e^{2ik(z' \cos \theta - [a + z' \tan \alpha] \cos \phi_1 \sin \theta)} \end{aligned} \tag{A. 2-18}$$

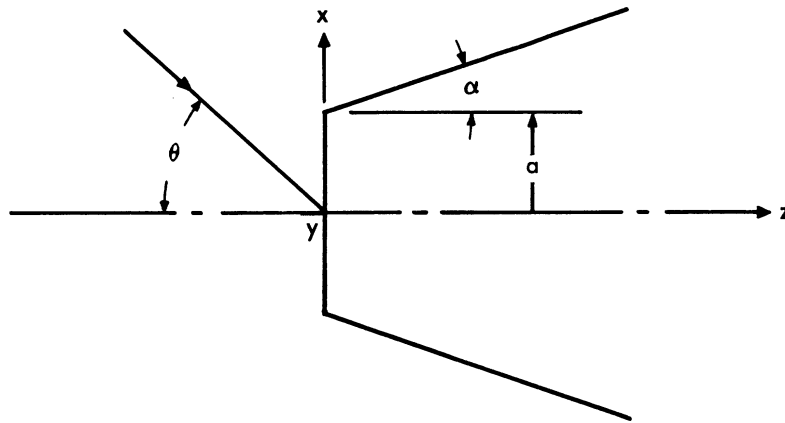


FIG. A-20

where ϕ_1 is the azimuthal angle determining the integration point. The unit normal to the surface is $\hat{n} = \hat{\xi} \cos \alpha + \hat{k} \sin \alpha$ so that the surface area element is

$$\vec{ds} = \left[\frac{dz'}{\cos \alpha} \right] \left[(a + z' \tan \alpha) d\phi_1 \right] (\hat{i} \cos \alpha + \hat{k} \sin \alpha) \quad (\text{A. 2-19})$$

The direction to the receiver is given by the unit vector $\hat{i} \sin \theta + \hat{k} \cos \theta$ (ϕ is taken to be zero) or $(\hat{i} \cos \phi_1 + \hat{j} \sin \phi_1) \sin \theta + \hat{k} \cos \theta$. Thus the projection of the surface area element in the direction of incidence is

$$dA = \cos \theta (a + z' \tan \alpha) (\tan \alpha + \tan \theta \cos \phi_1) dz' d\phi_1 \quad (\text{A. 2-20})$$

When the integral $g = \int e^{2ikz'} dA$ is integrated with respect to ϕ by stationary phase the result is

$$g \approx \cos \theta \int e^{2ikz' \cos \theta} (a + z' \tan \alpha) \sqrt{\frac{\lambda}{2(a + z' \tan \alpha) \sin \theta}} \times \left\{ (\tan \alpha + \tan \theta) e^{-2ik \sin \theta (a + z' \tan \alpha) + \frac{\pi i}{4}} + (\tan \alpha - \tan \theta) e^{2ik \sin \theta (a + z' \tan \alpha) - \frac{\pi i}{4}} U(\alpha - \theta) \right\} dz' \quad (\text{A. 2-21})$$

where $U(x)$ is the Heaviside unit function which is equal to one when x is positive and zero when x is negative. Since the only contribution comes from the region of small z' we can set $z' = 0$ except in the phase factor. Then, as long as $0 < \theta \leq \pi/2 - \alpha$, the value of the integral is

$$g \approx \frac{a \cos \theta (\tan \alpha + \tan \theta)}{2ik(\cos \theta - \sin \theta \tan \alpha)} \sqrt{\frac{\lambda}{2a \sin \theta}} e^{-2ika \sin \theta + \frac{\pi i}{4}} + \frac{a \cos \theta (\tan \alpha - \tan \theta)}{2ik(\cos \theta + \sin \theta \tan \alpha)} \sqrt{\frac{\lambda}{2a \sin \theta}} e^{2ika \sin \theta - \frac{\pi i}{4}} U(\alpha - \theta) \quad (\text{A. 2-22})$$

Substitution of Equation (A. 2-22) into Equation (A. 1-12) gives Equation (A. 3-26). When $\theta = \pi/2 - \alpha$ the phase factor in (A. 2-18) must be determined more accurately taking into account the curvature of the ogive. The parameters ρ and h introduced in Equation (A. 3-23) are shown in Figure A-21.

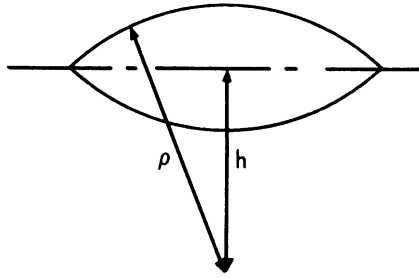


FIG. A-21

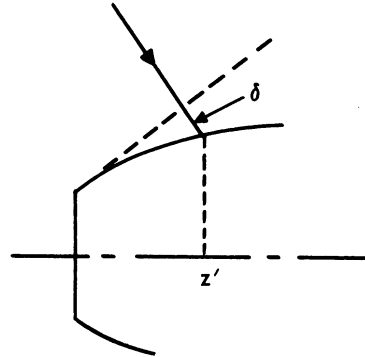


FIG. A-22

It can be seen that the curvature in which we are interested is determined by ρ . We get an extra phase factor $e^{2ik\delta}$ where δ is the distance shown in Figure A-22. For small z' , δ is approximately equal to $(z')^2 / (2\rho \cos^2 \alpha)$. When the extra phase factor is introduced into Equation (A. 2-22) and θ is set equal to $\pi/2 - \alpha$, the result is (for small z')

$$g \approx \frac{1}{\cos^{3/2} \alpha} \sqrt{\frac{\lambda a}{2}} \int_0^{\infty} e^{-\frac{ikz'^2}{\rho \cos^2 \alpha} - 2ika \cos \alpha + \frac{\pi i}{4}} dz' \quad (A. 2-23)$$

$$= \frac{\lambda \sqrt{a\rho}}{4\sqrt{\cos \alpha}} e^{-2ika \cos \alpha}$$

which gives the cross-section quoted in Equation (A. 3-30).

Another contribution must be added to the above to take account of the sharp edge. This additional contribution is calculated in Section A. 2. 10.

A. 2. 5 Rectangular Flat Plate

The physical optics integral is (see Figure A-30)

$$\begin{aligned}
 g &= \int_{-b}^b \int_{-a}^a e^{-2ik \sin \theta (x \cos \phi + y \sin \phi)} \cos \theta \, dx \, dy \\
 &= \frac{e^{2ika \sin \theta \cos \phi} - e^{-2ika \sin \theta \cos \phi}}{2ik \sin \theta \cos \phi} \frac{e^{2ikb \sin \theta \sin \phi} - e^{-2ikb \sin \theta \sin \phi}}{2ik \sin \theta \sin \phi} \cos \theta
 \end{aligned}
 \tag{A. 2-24}$$

from which follow Equations (A. 3-31) through (A. 3-34).

A. 2. 6 Flat Plate

At normal incidence Equation (A. 3-35) is an immediate consequence of Equation (A. 1-12). For non-normal incidence a study of the vibration curve indicates the validity of the remarks between Equation (A. 3-35) and Equation (A. 3-36). Equation (A. 3-36) can then be obtained from the circular disk formula. The circular disk formula is

$$\sigma = \frac{\pi a^2}{\tan^2 \theta} J_1^2 \left(\frac{4\pi a \sin \theta}{\lambda} \right), \tag{A. 2-25}$$

where $J_1(x)$ is the Bessel function of the first kind. When the asymptotic formula for the Bessel function is used it is found that the scattering is due to two components with the magnitude given in Equation (A. 3-36). For the elliptical disk the radius of curvature can be obtained from the formula

$$R = \left| \frac{\left[1 + \left(\frac{dy}{dx} \right)^2 \right]^{3/2}}{\frac{d^2y}{dx^2}} \right| \tag{A. 2-26}$$

and from Equation (A. 2-3) with c set equal to zero. The result is as shown in Equation (A. 3-38).

A. 2. 7 Ogive

Only the case $\theta = \pi/2 - \alpha$ need be considered here. The development goes exactly the same as it did in Section A. 2. 4 for the truncated ogive

except that now $z' \tan \alpha$ cannot be neglected with respect to a (since $a = 0$). The result is that Equation (A. 2-23) is replaced by

$$\begin{aligned}
 g &\approx \cos \theta \tan \alpha (\tan \alpha + \tan \theta) \int_0^{\infty} e^{\frac{\pi i}{4} - i \frac{kz'^2}{\rho \cos^2 \alpha}} z' dz' \\
 &= \cos \theta \tan \alpha (\tan \alpha + \tan \theta) e^{-\pi i/4} \frac{\rho \cos^2 \alpha}{2k} \quad (\text{A. 2-27})
 \end{aligned}$$

Substitution of Equation (A. 2-27) into Equation (A. 1-12) gives Equation (A. 3-40).

A. 2. 8 Tapered Wedge

The two-dimensional problem of scattering from a wedge has been solved exactly (Ref. A. 5). When a finite length of wedge (measured along the tip of the wedge) is used the cross-section can be obtained approximately by the current distribution method, Equation (A. 1-11). For a long length of wedge (compared to the wavelength) the current can be assumed to be the same as it is in the two-dimensional problem (provided that the direction of incidence is perpendicular to the edge of the wedge). Now, when the current distribution method is applied to the two-dimensional problem the integral over y (see Figure A-34) will be

$$\int_{-\infty}^{\infty} e^{ik\sqrt{r^2+y^2}} dy \approx \sqrt{r\lambda} e^{i(kr + \pi/4)}.$$

For the three-dimensional problem the integral over y will be

$$\int_0^L e^{ik\sqrt{r^2+y^2}} dy \approx L e^{ikr}.$$

This is the only difference between the two and three-dimensional problems so that the three-dimensional fields can be obtained from the two-dimensional fields by multiplying by $\frac{L e^{-\pi i/4}}{\sqrt{r\lambda}}$. Of course the same factor would apply to other bodies as well as the wedge.

The results from Reference A. 5 (which are for $\theta = 0$, see Figure A-34) are:

$$\begin{aligned}\sigma_{\perp} &= \frac{\pi L^2}{(\pi - \alpha)^2 \tan^2\left(\frac{\pi^2}{2(\pi - \alpha)}\right)} \\ \sigma_{11} &= \frac{\pi L^2}{(\pi - \alpha)^2} + \frac{\pi L^2}{(\pi - \alpha)^2 \tan^2\left(\frac{\pi^2}{2(\pi - \alpha)}\right)}\end{aligned}\tag{A. 2-28}$$

where σ_{\perp} is the cross-section for polarization perpendicular to the edge of the wedge, and σ_{11} is for polarization parallel to the edge of the wedge. Now for this problem physical optics gives for either polarization

$$\sigma = \frac{L^2 \tan^2 \alpha}{4\pi}\tag{A. 2-29}$$

For small α Equation (A. 2-29) agrees with the value of σ_{\perp} given by Equation (A. 2-28). For parallel polarization there is an additional contribution which we will call the "thin wire" contribution. We will consider first directions of incidence which lie in the x - z plane. Physical optics gives the second term in Equation (A. 3-41) and Equation (A. 3-42). The first term in these equations is the "thin wire" contribution which has been added on. When $\theta > \pi/2 - \alpha$ the tapered wedge looks like a cylinder; so, no special formula will be derived for such aspects.

It can be verified that for $\theta = \gamma = 0$ and $\alpha \approx 0$ the "thin wire" contribution can be obtained from Equation (A. 1-9) by taking the radius of the wire to be about 1/85 of a wavelength. We will assume that this holds true for other aspects also. For aspects not in the x-z plane, Equation (A. 1-9) gives the thin wire contribution. In the notation of Figure A-34, Equation (A. 1-9) takes the form

$$\sigma = \frac{\lambda^2(1 - \sin^2 \theta \sin^2 \phi) \cos^4 \gamma}{4\pi \sin^2 \theta \sin^2 \phi \left\{ \pi^2 + [\sqrt{3}\pi - \log_e(1 - \sin^2 \theta \sin^2 \phi)]^2 \right\}} \left(\frac{\pi}{\pi - \alpha} \right)^2\tag{A. 2-30}$$

The remaining terms in Equation (A. 3-43) are the physical optics terms.

A. 2. 9 Corner Reflectors

The corner contributions are given in Reference A. 6 so that only the dihedral contributions will be considered here. The notation is as given in Section A. 3. 10. The dihedral contributions are the result of double scattering and thus occur only when the direction of incidence is nearly parallel to one of the faces of the corner reflector and is such that the radar is looking into the dihedral. Thus $l \sim 0$ and $m > 0$, $n > 0$. To begin with we will consider only the case where l is exactly zero (normal incidence). As discussed in Reference A. 6, the reflection from the dihedral is equivalent to the diffraction through an equivalent aperture. The equivalent aperture is the projection of the part of the dihedral that reflects radiation back to the transmitter (projected in the direction of the transmitter) as shown for a square corner reflector in Figure A-23. The cross-section of the dihedral is $(4\pi A^2)/\lambda^2$ where A is the area of the equivalent aperture. For square, circular, and triangular corners this area is $2a^2m$, $(\pi/2)a^2m$, and a^2m respectively. The effective cross-section is, in general, smaller than the cross-section since the scattered field is not polarized parallel to the incident field. The component of the electric field perpendicular to the edge of the dihedral (the line of intersection of the faces of the dihedral) is reversed while the component parallel to the edge is not (Fig. A-24). The angle between the incident and scattered polarizations is 2γ so that the cross-section must be multiplied by $\cos^2 2\gamma$ to obtain the effective cross-section. The horizontal and vertical polarization vectors are $\hat{\rho}_H = -\sin\phi^* \hat{i} + \cos\phi^* \hat{j}$ and $\hat{\rho}_V = \cos\theta^* \cos\phi^* \hat{i} + \cos\theta^* \sin\phi^* \hat{j} - \sin\theta^* \hat{k}$ respectively. There is a difference of 90 degrees in γ for these two cases so that the effective cross-section is the same. If \hat{e}_i is the vector describing the edge of the dihedral we have $\cos\gamma_V = \hat{e}_i \cdot \hat{\rho}_V = e_{ix} \cos\theta^* \cos\phi^* + e_{iy} \cos\theta^* \sin\phi^* - e_{iz} \sin\theta^*$. But at normal incidence we also have the condition $\hat{e}_i \cdot \hat{v} = e_{ix} \sin\theta^* \cos\phi^* + e_{iy} \sin\theta^* \sin\phi^* + e_{iz} \cos\theta^* = 0$. Multiplying the first relation by $\sin\theta^*$, the second by $\cos\theta^*$, and subtracting we find $\cos\gamma_V = -(e_{iz})/\sin\theta^*$. This, together with the expressions for the cross-section given above, yields the formulas for σ_{\perp} (Eq. (A. 3-45), (A. 3-49), and (A. 3-50)).

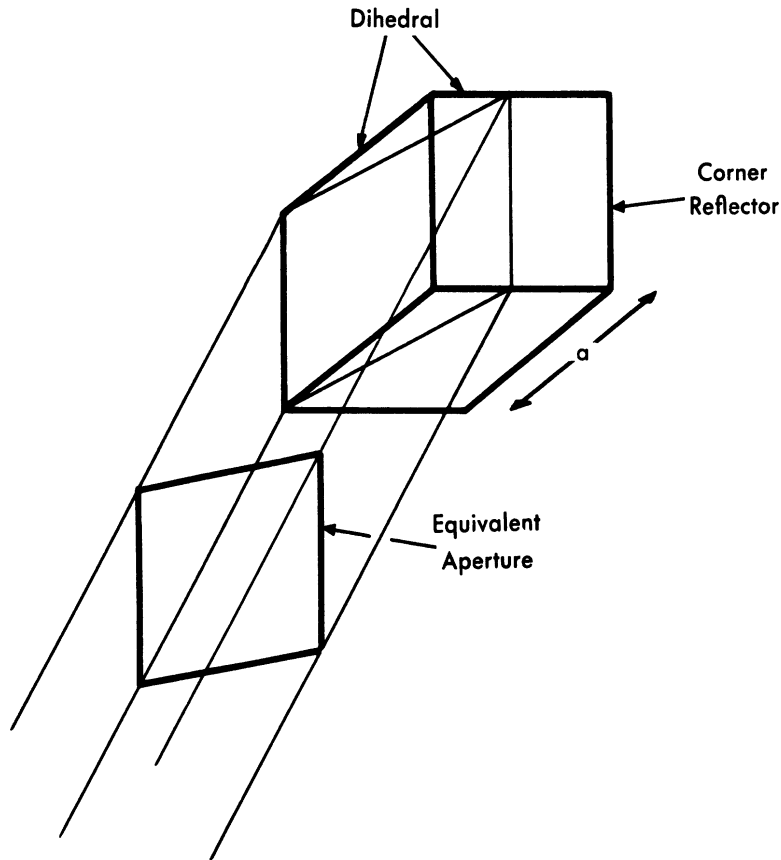


FIG. A-23

The azimuth at normal incidence is obtained from the expression $\hat{e}_i \cdot \hat{v} = 0$ by using the relation

$$A \sin \phi^* + B \cos \phi^* = \frac{A}{|A|} \sqrt{A^2 + B^2} \sin \left(\phi^* + \tan^{-1} \frac{B}{A} \right).$$

This gives

$$\sin \theta^* \frac{e_{iy}}{|e_{iy}|} \sqrt{e_{ix}^2 + e_{iy}^2} \sin \left(\phi^* + \tan^{-1} \frac{e_{ix}}{e_{iy}} \right) + e_{iz} \cos \theta^* = 0 \quad (\text{A. 2-31})$$

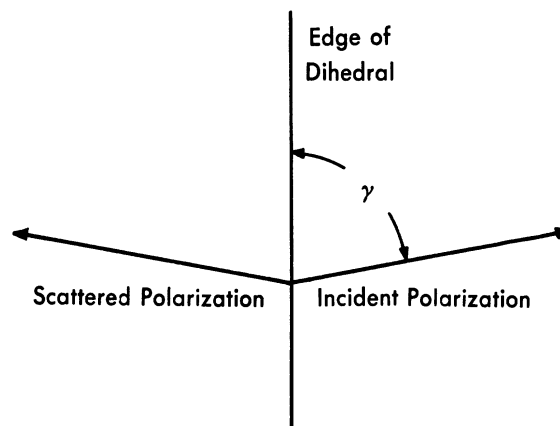


FIG. A-24

Equations (A. 3-46), (A. 3-49), and (A. 3-50) for ϕ_{\perp} follow directly from Equation (A. 2-31).

For deviations of l from zero the cross-section of the dihedral drops off like that of a flat plate having the shape of the (normal incidence) equivalent aperture. From the results on flat plates given in Equations (A. 3-31) through (A. 3-38), it is found that the cross-section is reduced to a fraction β of its normal incidence value for

$$\begin{aligned}
 l &= \pm \frac{\lambda}{2\pi\sqrt{2\beta} a} && \text{(square)} \\
 l &= \pm \frac{\lambda}{\pi^2\sqrt{\beta} a} && \text{(circular)} \\
 l &= \pm \frac{\lambda}{2\pi\sqrt{\beta} a} && \text{(triangular)}
 \end{aligned}
 \tag{A. 2-32}$$

When ℓ is not zero we have

$$\ell = \sin \theta^* \frac{e_{iy}}{|e_{iy}|} \sqrt{e_{ix}^2 + e_{iy}^2} \sin \left(\phi^* + \tan^{-1} \frac{e_{ix}}{e_{iy}} \right) + e_{iz} \cos \theta^* \quad (\text{A. 2-33})$$

instead of Equation (A. 2-31). Using the expansion $\sin^{-1}(A + \epsilon) = \sin^{-1} A + \epsilon / \sqrt{1 - A^2} + \dots$ we obtain Equations (A. 3-47), (A. 3-49), and (A. 3-50) under the assumptions that $\lambda/a \ll \sin \theta$.

A. 2.10 Sharp Edges

There is a contribution to the scattering from sharp edges when the incident polarization is parallel to the edge. This contribution is similar to the scattering from a thin wire whose radius is about 1/85 of a wavelength. The scattered field from a small straight piece of the thin wire is like the field of a dipole so that it has the form

$$\vec{E}_s = K d\ell \frac{\hat{r} \times (\hat{r} \times \hat{d})}{r} e^{ikr} \quad (\text{A. 2-34})$$

where K is a constant to be determined, $d\ell$ is the length of the piece, \hat{r} is the unit vector to the field point, r is the distance to the field point, and \hat{d} is a unit vector along the piece of wire. At normal incidence with the polarization parallel to \hat{d} the cross-section is

$$\sigma = 4 \pi r^2 \left| \frac{\vec{E}_s}{E_i} \right|^2 = \frac{(d\ell)^2}{\pi} \quad (\text{A. 2-35})$$

If $\hat{\rho}$ is the polarization vector then K is proportional to $\hat{\rho} \cdot \hat{d}$. For the case to which Equation (A. 2-35) applies we have $\hat{\rho} \cdot \hat{d} = |\hat{r} \times (\hat{r} \times \hat{d})| = 1$. Substitution of Equation (A. 2-34) into Equation (A. 2-35) gives

$$\frac{(d\ell)^2}{\pi} = 4 \pi r^2 \frac{|K|^2 (d\ell)^2}{(\hat{\rho} \cdot \hat{d})^2 r^2 |\vec{E}_i|^2} \quad (\text{A. 2-36})$$

Substitution back finally gives (taking into account the phase lag in making the round trip from the radar to the wire and back)

CONFIDENTIAL

UNIVERSITY OF MICHIGAN

2260-1-T

$$\vec{E}_s = \frac{\hat{\rho} \cdot \hat{d}}{2\pi} |\vec{E}_i| d\ell \frac{\hat{r} \times (\hat{r} \times \hat{d})}{r} e^{2ikr} \quad (\text{A. 2-37})$$

Thus corresponding to the physical optics formula for the cross-section (Eq. A. 1-12) we have, in the case of a thin wire,

$$\sigma = \frac{1}{\pi} |\vec{g}|^2 ; \quad \sigma_e = \frac{1}{\pi} |\hat{\rho} \cdot \vec{g}|^2$$

$$\vec{g} = \int (\hat{\rho} \cdot \hat{d}) \hat{r} \times (\hat{r} \times \hat{d}) e^{2ik\zeta} d\ell \quad (\text{A. 2-38})$$

Due to the relation $\hat{\rho} \cdot \hat{r} = 0$ we can also write

$$\sigma_e = \frac{1}{\pi} \left| \int (\hat{\rho} \cdot \hat{d})^2 e^{2ik\zeta} d\ell \right|^2 \quad (\text{A. 2-39})$$

The integration in both Equation (A. 2-38) and Equation (A. 2-39) is taken along the wire. The edge of a truncated ogive gives a thin wire contribution where the thin wire is a loop in the x-y plane as shown in Figure A-25. The thin wire contribution is given in general by Equation (A. 2-39). To evaluate this for a loop consider that on the wire we have $x = a \cos \phi$, $y = a \sin \phi$, and $d\ell = \sqrt{dx^2 + dy^2} = a d\phi$. We will assume that the direction incidence is in the x-z plane and is given by $\hat{V} = \hat{i} \sin \theta + \hat{k} \cos \theta$. The direction of the dipole is $\hat{d} = -\sin \phi \hat{i} + \cos \phi \hat{j}$. We have $\zeta = (\hat{x}\hat{i} + \hat{y}\hat{j}) \cdot \hat{V} = a \sin \theta \cos \phi$. The polarization vector is $\hat{\rho} = -\cos \theta \sin \gamma \hat{i} + \cos \gamma \hat{j} + \sin \theta \sin \gamma \hat{k}$ where γ is the angle between the polarization vector and the y-axis. Substitution into Equation (A. 2-39) gives finally

$$\sigma_e = \frac{1}{\pi} \left| a \int_0^{2\pi} e^{2ika \sin \theta \cos \phi} (\cos^2 \theta \sin^2 \phi \sin^2 \gamma + 2 \cos \theta \sin \phi \cos \phi \sin \gamma \cos \gamma + \cos^2 \phi \cos^2 \gamma) d\phi \right|^2$$

$$= \pi a^2 \left| (\cos^2 \theta \sin^2 \gamma + \cos^2 \gamma) J_0(2ka \sin \theta) + [(\cos^2 \theta \sin^2 \gamma - \cos^2 \gamma) J_2(2ka \sin \theta)] \right|^2 \quad (\text{A. 2-40a})$$

¹ The ζ here corresponds to the ρ of Equation (A. 1-12).

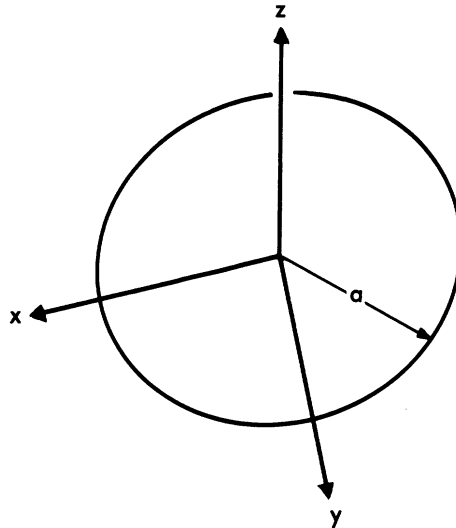


FIG. A-25

For $\theta = 0$, Equation (A. 2-40a) gives $\sigma_e = \pi a^2$. For θ enough greater than zero that $2ka \sin\theta \gg 1$ we can use the asymptotic expansions for the Bessel functions:

$$J_0(z) \sim \sqrt{\frac{2}{\pi z}} \left[\cos(z - \pi/4) + \frac{1}{8z} \sin(z - \pi/4) - \frac{9}{128z^2} \cos(z - \pi/4) + \dots \right]$$

$$J_2(z) \sim \sqrt{\frac{2}{\pi z}} \left[-\cos(z - \pi/4) + \frac{15}{8z} \sin(z - \pi/4) + \frac{105}{128z^2} \cos(z - \pi/4) + \dots \right]$$

(A. 2-40b)

Using Equation (A. 2-40b) and the average values of $\sin^2(2ka \sin\theta - \pi/4)$, $\sin(2ka \sin\theta - \pi/4) \cos(2ka \sin\theta - \pi/4)$, and $\cos^2(2ka \sin\theta - \pi/4)$ (which are $1/2$, 0 , and $1/2$ respectively) in Equation (A. 2. 40a) we obtain

$$\text{Average } \sigma_e \sim \frac{a \lambda}{\pi \sin\theta} \left\{ \cos^4 \gamma + \frac{8 \cos^4 \theta \sin^4 \gamma - 8 \cos^2 \theta \sin^2 \gamma \cos 2\gamma - \cos^4 \gamma}{32 (ka \sin \theta)^2} \right\}$$

(A. 2-40c)

Except when $\cos \gamma$ is nearly zero the first term in braces is sufficient and the cross-section becomes $\beta \pi a^2$ for

$$\theta \sim \frac{\lambda \cos^4 \gamma}{\pi^2 a \beta} .$$

For $\cos \gamma = 0$ the cross-section becomes $\beta \pi a^2$ when

$$\theta \sim \frac{\lambda}{(2 \pi)^{4/3} a \beta^{1/3}} .$$

The sum of these two expressions is what was used in Section A. 3.

A.3 LIST OF CROSS-SECTION FORMULAS

In this section we will list some cross-section formulas. The derivation of these formulas will be found either in Section A.2 or in the references.

A.3.1 Ellipsoid

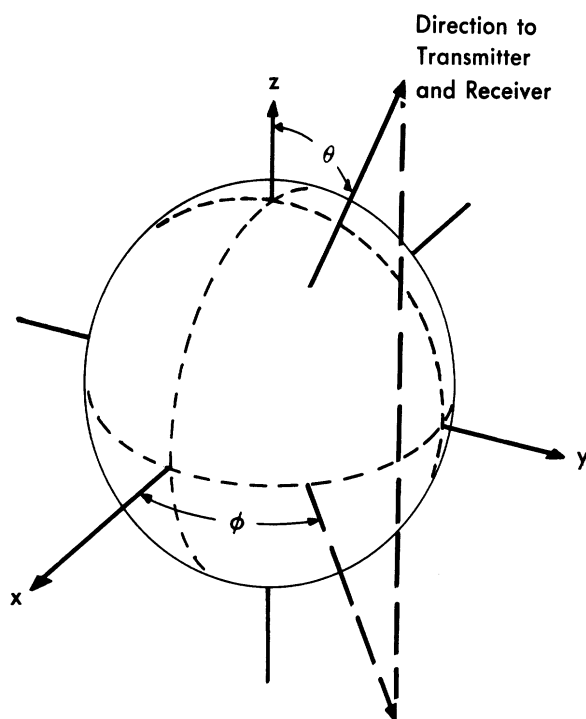


FIG. A-26

Let the equation of the ellipsoid be $(x/a)^2 + (y/b)^2 + (z/c)^2 = 1$. Then, if θ and ϕ are the polar angles for the direction of incidence (Fig. A-26), the cross-section is given by

$$\sigma = \frac{\pi a^2 b^2 c^2}{(a^2 \sin^2 \theta \cos^2 \phi + b^2 \sin^2 \theta \sin^2 \phi + c^2 \cos^2 \theta)^2} \quad (\text{A.3-1})$$

For $a = b$, Equation (A.3-1) reduces to

$$\sigma = \frac{\pi b^4 c^2}{(b^2 \sin^2 \theta + c^2 \cos^2 \theta)^2} \quad (\text{A.3-2})$$

and for $a = b = c$ the expression becomes simply

$$\sigma = \pi c^2 \quad . \quad (A.3-3)$$

A.3.2 Truncated Elliptic Cone

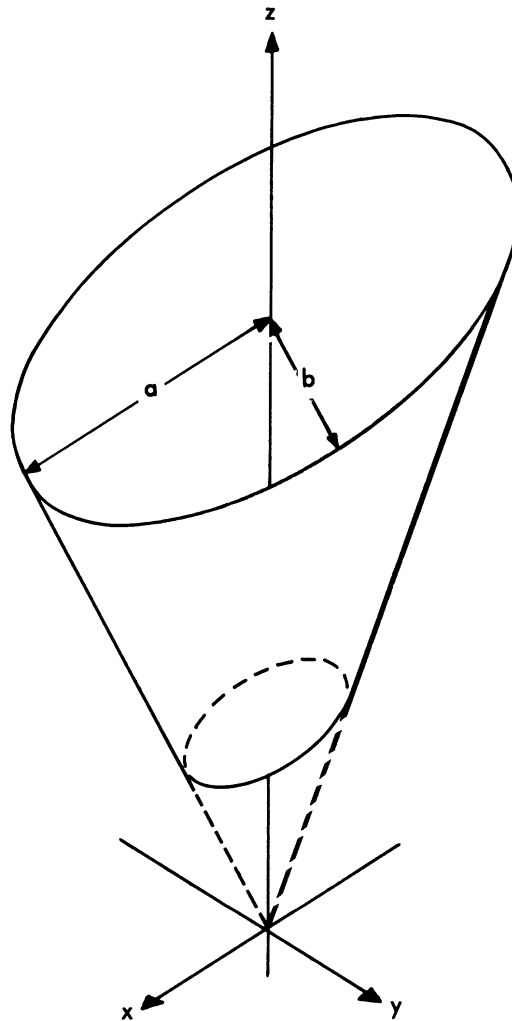


FIG. A-27

The cone is assumed to be truncated by the planes $z = L_1$ and $z = L_2$ ($L_2 > L_1$). The half-angle of the cone in the xz -plane is taken to be α , that is $\tan \alpha = a/L_2$. The ratio of a to b is taken to be $a/b = \eta$. The direction

to the transmitter-receiver is specified by the polar angles θ and ϕ (Fig. A-26). The formulas are meant to apply only for $\sin\theta > \sin\alpha$. At normal incidence the cross-section is

$$\begin{aligned}\sigma_{\perp} &= \frac{8\pi\eta \left(L_2^{3/2} - L_1^{3/2}\right)^2 \tan\alpha}{9\lambda\sin\theta\sqrt{\sin^2\phi + \eta^2\cos^2\phi}} \left(\frac{\sin\theta}{\sqrt{\sin^2\phi + \eta^2\cos^2\phi}} - \frac{1}{\eta} \cos\theta\tan\alpha \right)^2 \\ &= \frac{8\pi \left(L_2^{3/2} - L_1^{3/2}\right)^2 \tan^4\alpha}{9\lambda\eta^2 |\cos^3\theta|}\end{aligned}\quad (\text{A. 3-4})$$

where normal incidence is defined to be the direction given by

$$\tan\theta = - \frac{\eta}{\tan\alpha\sqrt{\sin^2\phi + \eta^2\cos^2\phi}} \quad (\text{A. 3-5})$$

For non-normal incidence there are two independent scatterers (the ends of the cone). If one of the ends of the cone is smoothly rounded then at non-normal incidence its contribution would have to be computed by means of a formula for the rounded end (for example the ellipsoid formula). The two contributions are given by

$$\sigma = \frac{\lambda z \eta^3 \tan\alpha}{8\pi\sin\theta\sqrt{\sin^2\phi + \eta^2\cos^2\phi}} \left(\frac{\frac{\sin\theta}{\sqrt{\sin^2\phi + \eta^2\cos^2\phi}} - \frac{1}{\eta} \cos\theta\tan\alpha}{\sin\theta\tan\alpha\sqrt{\sin^2\phi + \eta^2\cos^2\phi} + \eta\cos\theta} \right)^2 \quad (\text{A. 3-6})$$

where z has the value L_1 or L_2 depending on whether the contribution is from the small end or the large end of the cone.

For the truncated circular cone $\eta = 1$, Equations (A. 3-4) and (A. 3-6) reduce to

$$\begin{aligned}\sigma &= \frac{8\pi}{9\lambda} \left(L_2^{3/2} - L_1^{3/2}\right)^2 \tan\alpha \left(1 - \frac{\tan\alpha}{\tan\theta}\right)^2 \sin\theta \\ &= \frac{8\pi}{9\lambda} \left(L_2^{3/2} - L_1^{3/2}\right)^2 \frac{\sin\alpha}{\cos^4\alpha}\end{aligned}\quad (\text{A. 3-7})$$

$$\sigma = \frac{\lambda z \tan \alpha}{8\pi \sin \theta} \tan^2(\theta - \alpha) \quad . \quad (\text{A. 3-8})$$

The formulas for an elliptic cylinder can also be obtained from Equations (A. 3-5) and (A. 3-6) as a limiting case. To accomplish this let $\tan \alpha = a/L_2$, $L_1 = L_2 - L$, $L_2 \rightarrow \infty$. The results are for normal incidence

$$\sigma_{\perp} = \frac{2\pi L^2 a^2 b^2}{\lambda (a^2 \cos^2 \phi + b^2 \sin^2 \phi)^{3/2}} \quad (\text{A. 3-9})$$

and for non-normal incidence we have two components each equal to

$$\sigma = \frac{\lambda a^2 b^2 \sin \theta}{8\pi \cos^2 \theta (a^2 \cos^2 \phi + b^2 \sin^2 \phi)^{3/2}} \quad . \quad (\text{A. 3-10})$$

For a circular cylinder of radius a , Equations (A. 3-9) and (A. 3-10) reduce to

$$\sigma_{\perp} = \frac{2\pi L^2 a}{\lambda} \quad (\text{A. 3-11})$$

$$\sigma = \frac{\lambda a \sin \theta}{8\pi \cos^2 \theta} \quad (\text{A. 3-12})$$

respectively.

A. 3.2.1 Application of the Truncated Elliptic Cone to Wing and Elevator Surfaces

To express the results of the previous section in terms of the aircraft coordinates when the cones are used to replace the wing and elevator surfaces use the transformation formulas developed in Section A1.9.2.

The cross-section of the elliptic cone is small except near normal incidence which is given by

$$\tan \theta = - \frac{\eta}{\tan \alpha \sqrt{\sin^2 \phi + \eta^2 \cos^2 \phi}} \quad . \quad (\text{A. 3-13})$$

Since α is a small angle θ will be slightly greater than $\pi/2$, say $\theta = \pi/2 + \epsilon$. Thus $\cos\theta = \cos(\pi/2 + \epsilon) \sim -\epsilon$. Using this value of $\cos\theta$ in Equation (A.1-45) we find that $\phi^* \sim \psi$ so that $\sin(\psi - \phi^*) \sim \psi - \phi^*$. Finally we find from Equation (A.1-45) that

$$\phi^* = \psi + \frac{\epsilon + \delta \cos \theta^* \cos \psi}{\sin \theta^*} \quad (\text{A. 3-14})$$

up to terms of order two.

Since $\phi^* = \psi$ up to order one we can replace Equation (A.3-13) by

$$\sin^2 \phi = \cos^2 \theta^*; \quad \cos^2 \phi = \sin^2 \theta^* \quad (\text{A. 3-15})$$

up to order one. Furthermore on substituting $\theta = \pi/2 + \epsilon$ into Equation (A.3-13) we find on using Equation (A.3-15) that

$$\epsilon = \tan \alpha \sqrt{\frac{1}{\eta^2} \cos^2 \theta^* + \sin^2 \theta^*} \quad (\text{A. 3-16})$$

up to terms of order two. On using Equations (A.3-4), (A.3-13), and (A.3-15) we can calculate σ up to terms of order two with the final result that at normal incidence

$$\sigma_{\perp} = \frac{8\pi\eta \left(L_2^{3/2} - L_1^{3/2} \right)^2 \tan \alpha}{9\lambda (\cos^2 \theta^* + \eta^2 \sin^2 \theta^*)^{3/2}}$$

$$\phi_{\perp}^* = \psi + \tan \alpha \sqrt{1 + \frac{1}{\eta^2} \cot^2 \theta^* + \delta \cot \theta^* \cos \psi} \quad (\text{A. 3-17})$$

By using the methods given in Section A.1.7 we find that for non-normal incidence

$$\sigma = \beta \sigma_{\perp}$$

$$\phi^* = \phi_{\perp}^* \pm \frac{3\lambda \sqrt{L_1 + L_2}}{8\pi \sqrt{\beta} \left(L_2^{3/2} - L_1^{3/2} \right) \sin \theta^*} \quad (\text{A. 3-18})$$

Generally the shape of the peak can be obtained by calculating σ_{\perp} , ϕ_{\perp}^* and σ , ϕ^* for $\beta = 1/2$ and $\beta = 1/10$.

For the case $\alpha = 0$, $L_2 - L_1 = L$, Equations (A.3-17) and (A.3-18) reduce to

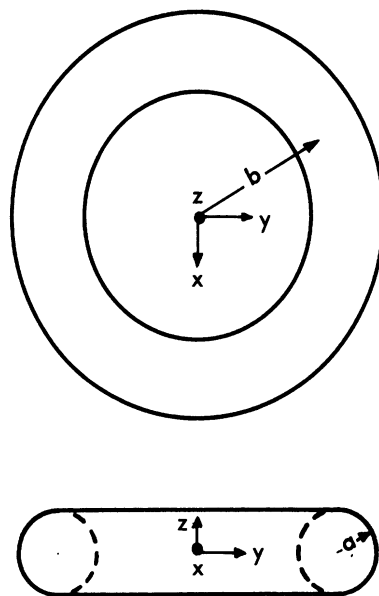
$$\sigma_{\perp} = \frac{2 \pi L^2 a^2 b^2}{\lambda (a^2 \sin^2 \theta^* + b^2 \cos^2 \theta^*)^{3/2}}$$

$$\phi_{\perp}^* = \psi + \delta \cot \theta^* \cos \psi$$

$$\sigma = \beta \sigma_{\perp}$$

$$\phi^* = \phi_{\perp}^* + \frac{\sqrt{2} \lambda}{4 \pi \sqrt{\beta} L \sin \theta^*} \quad \cdot \quad \text{(A.3-19)}$$

A.3.3 Torus



Two Views of the Torus

FIG. A-28

In Figure A-28, at normal incidence ($\theta = 0$), the cross-section is

$$\sigma = \frac{8\pi^3 a b^2}{\lambda} \quad . \quad (\text{A. 3-21})$$

Away from normal incidence and for directions of incidence in the range $a/(2b) < |\cos \theta| < 1$, there are two components which have the cross-sections

$$\sigma = \pi \left(\frac{ab}{\sin \theta} + a^2 \right)$$

and

$$\sigma = \pi \left(\frac{ab}{\sin \theta} - a^2 \right) \quad . \quad (\text{A. 3-22})$$

In the range $0 \leq |\cos \theta| < a/(2b)$ the second of the two contributions in Equation (A. 3-22) is no longer present.

A. 3.4 Truncated Ogive

In Figure A-29, one fourth of the figure is cut away to aid in dimensioning. "a" is the radius of the ogive at the point at which it is truncated. b is the radius of the ogive at its thickest part. α is the angle between the z-axis and the ogive tangent plane where the ogive is truncated. The parameters in terms of which the ogive is described in Reference A. 4 are

$$\rho = (b - a) \frac{1 + \cos \alpha}{\sin^2 \alpha} \quad \text{and} \quad h = (b \cos \alpha - a) \frac{1 + \cos \alpha}{\sin^2 \alpha} \quad . \quad (\text{A. 3-23})$$

In terms of these parameters the equation of the ogive is

$$(\xi + h)^2 + z^2 = \rho^2 \quad (\text{A. 3-24})$$

where $\xi = \sqrt{x^2 + y^2}$.

For incidence along the z-axis the cross-section as given by physical optics is

$$\sigma = \pi a^2 \tan^2 \alpha \quad . \quad (\text{A. 3-25})$$

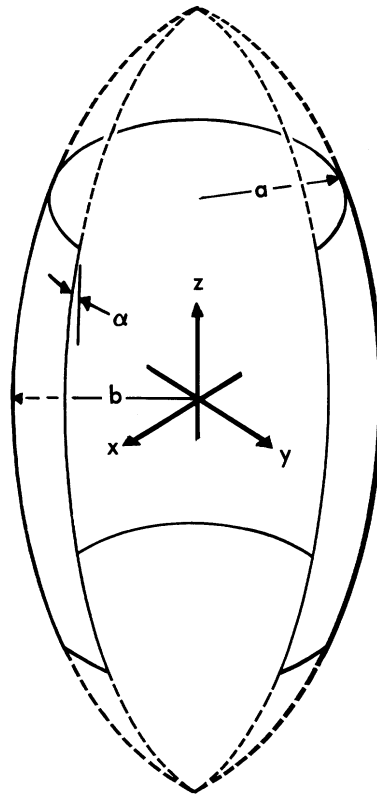


FIG. A-29

For $0 < \theta < \alpha$ and $\theta < \pi/2 - \alpha$ there are two contributions to the cross-section with the magnitudes

$$\sigma = \frac{\lambda a}{8 \pi \sin \theta} \tan^2 (\theta + \alpha) \quad (\text{A. 3-26})$$

and

$$\sigma = \frac{\lambda a}{8 \pi \sin \theta} \tan^2 (\theta - \alpha) .$$

For $\alpha \leq \theta < \pi/2 - \alpha$ (a range which exists only when $\alpha < 45^\circ$) the second of these two contributions is absent.

For $\pi/2 - \alpha < \theta \leq \pi/2$ the cross-section is

$$\sigma = \pi \rho^2 \left(1 - \frac{h}{\rho \sin \theta} \right) \quad (\text{A. 3-27})$$

where ρ and h are given by Equation (A. 3-23). For $\theta > \pi/2$ the symmetry of the body may be used.

The expressions given above for the cross-section of a truncated ogive are those given by physical optics. An additional thin wire loop contribution must be added. This contribution is large only for incidence along (or nearly along) the z-axis. For incidence exactly along the z-axis the additional contribution is

$$\sigma_{\perp} = \pi a^2. \quad (\text{A. 3-28})$$

The cross-section is reduced by a factor β for a deviation from the z-axis by an angle θ where

$$\theta = \frac{\lambda}{\pi^2 a} \frac{\cos^4 \gamma}{\beta} + \frac{\lambda}{(2\pi)^{4/3} a \beta^{1/3}} \quad (\text{A. 3-29})$$

where γ is an angle specifying the polarization and given as follows: γ is the angle between the polarization vector and the normal to the plane formed by the z-axis and the direction of incidence.

It should be observed that at $\theta = \pi/2 - \alpha$ the cross-section is

$$\sigma = \frac{\pi a \rho}{4 \cos \alpha}. \quad (\text{A. 3-30})$$

A. 3.5 Rectangular Flat Plate

In Figure A-30, at normal incidence ($\theta = 0$) the cross-section is

$$\sigma = \frac{64 \pi a^2 b^2}{\lambda^2}. \quad (\text{A. 3-31})$$

In the y-z plane ($\phi = \pi/2$ or $3\pi/2$) there are two components each contributing:

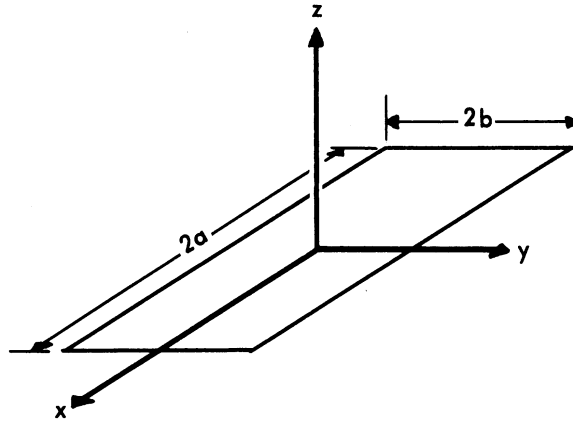


FIG. A-30

$$\sigma = \frac{a^2}{\pi \sin^2 \theta} \quad (A. 3-32)$$

In the x-z plane ($\phi = 0$ or π) there are two components each contributing

$$\sigma = \frac{b^2}{\pi \sin^2 \theta} \quad (A. 3-33)$$

For other aspects there are four components each contributing

$$\sigma = \frac{\lambda^2 \cos^2 \theta}{64 \pi^3 \sin^4 \theta \sin^2 \phi \cos^2 \phi} \quad (A. 3-34)$$

A. 3.6 Flat Plate

The plate is taken to be in the x-y plane (Fig. A-31) and to have an arbitrary shape except that there are no corners. At normal incidence ($\theta = 0$) the cross-section is

$$\sigma_{\perp} = \frac{4 \pi A^2}{\lambda^2} \quad (A. 3-35)$$

where A is the area of the plate. For non-normal incidence there is one component for each time the projection of the direction of incidence into the plane of the plate is perpendicular to the curve bounding the plate. If R is the radius of curvature of the bounding curve at the point where the

projected direction of incidence is perpendicular to the curve then the contribution to the cross-section is

$$\sigma = \frac{R \lambda}{8 \pi \sin \theta \tan^2 \theta}$$

(A. 3-36)

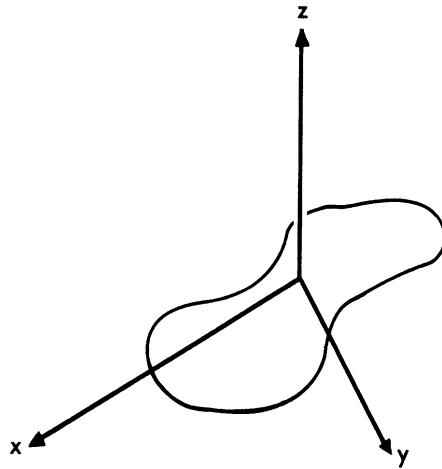


FIG. A-31

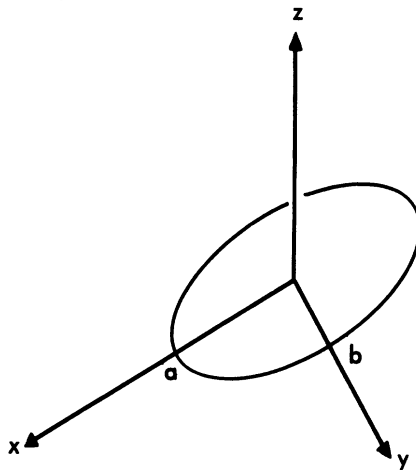


FIG. A-32

Applying the above results to an elliptical disk (Fig. A-32) we find, at normal incidence

$$\sigma = \frac{4 \pi^3 a^2 b^2}{\lambda^2} \quad . \quad (\text{A. 3-37})$$

For non-normal incidence the disk answer consists of two components each equal to

$$\sigma = \frac{\lambda a^2 b^2}{8 \pi \sin \theta \tan^2 \theta (a^2 \cos^2 \phi + b^2 \sin^2 \phi)^{3/2}} \quad . \quad (\text{A. 3-38})$$

A. 3.7 Ogive

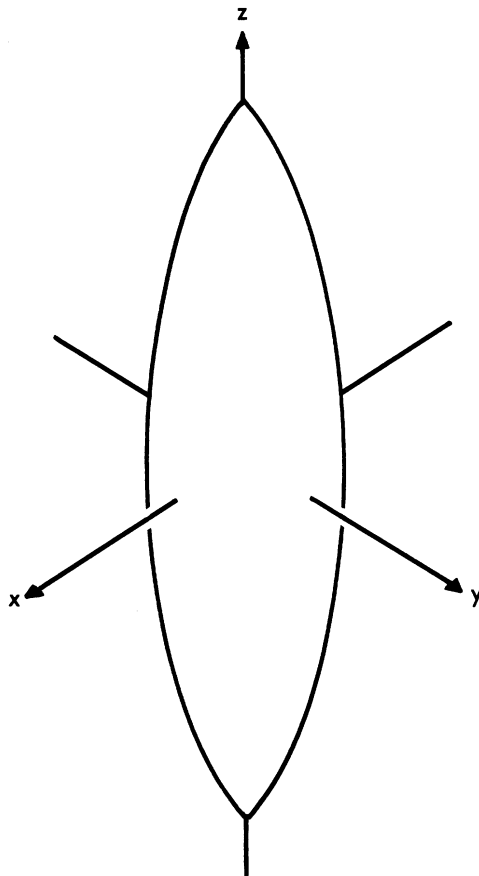


FIG. A-33

The parameters and equation of the ogive (Fig. A-33) are given in Section A.3.4. In this case $\alpha = 0$ and α is the half angle at the nose of the ogive. For $\pi/2 - \alpha < \theta \leq \pi/2$ the cross-section is still given by Equation (A.3-27). For $0 \leq \theta < \pi/2 - \alpha$ a comparison of the vibration curves shows that the cross-section of the ogive is the same as that of a cone of half-angle α , which is shown in Reference A.4 to be equal to

$$\sigma = \frac{\lambda^2 \tan^4 \alpha}{16 \pi \cos^6 \theta (1 - \tan^2 \alpha \tan^2 \theta)^3} \quad (\text{A. 3-39})$$

For $\theta = \pi/2 - \alpha$ the cross-section is

$$\sigma = \frac{\rho^2 \sin^2 \alpha}{4 \pi} = \frac{b^2}{4 \pi \tan^2 \alpha/2} \quad (\text{A. 3-40})$$

For $\theta > \pi/2$ the results can be obtained by symmetry.

A.3.8 Tapered Wedge

It is assumed that $\alpha < 45^\circ$. In the x-z plane when $0 \leq \theta < \alpha$ the cross-section is

$$\sigma = \frac{\pi L^2}{(\pi - \alpha)^2} \cos^4 \gamma + \frac{L^2 \sin^2 2\alpha}{4 \pi \cos^2(\alpha - \theta) \cos^2(\alpha + \theta)} \quad (\text{A. 3-41})$$

where γ (Fig. A-34) is the angle between the polarization vector and the plane determined by the direction of incidence and the edge of the wedge. For incidence in the x-z plane and $\alpha \leq \theta < \pi/2 - \alpha$ the cross-section is

$$\sigma = \frac{\pi L^2}{(\pi - \alpha)^2} \cos^4 \gamma + \frac{L^2}{4 \pi} \tan^2(\alpha + \theta) \quad (\text{A. 3-42})$$

For incidence not in the x-z plane and $0 \leq \tan \theta \cos \phi \leq \tan \alpha$, there are two components each contributing

$$\sigma = \frac{\lambda^2 (1 - \sin^2 \theta \sin^2 \phi) \cos^4 \gamma}{4 \pi \sin^2 \theta \sin^2 \phi \left\{ \pi^2 + [\sqrt{3} \pi - \log_e (1 - \sin^2 \theta \sin^2 \phi)]^2 \right\}} \left(\frac{\pi}{\pi - \alpha} \right)^2$$

$$\begin{aligned}
 & + \frac{\lambda^2}{64 \pi^3 \sin^2 \theta \sin^2 \phi} \left[\frac{\sin \alpha \cos \theta + \cos \alpha \sin \theta \cos \phi}{\cos \alpha \cos \theta - \sin \alpha \sin \theta \cos \phi} \right. \\
 & \left. + \frac{\sin \alpha \cos \theta - \cos \alpha \sin \theta \cos \phi}{\cos \alpha \cos \theta + \sin \alpha \sin \theta \cos \phi} \right]^2 \quad . \quad (\text{A. 3-43})
 \end{aligned}$$

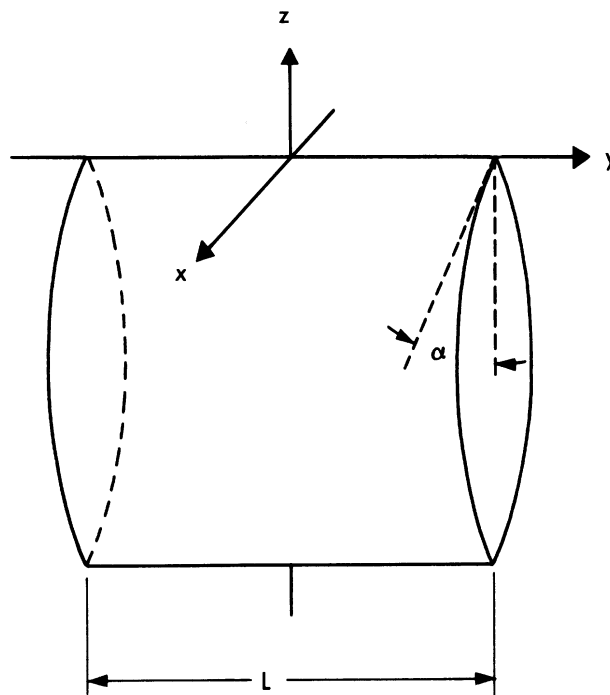


FIG. A-34

For $\tan \alpha \leq \tan \theta \cos \phi < 1/\tan \alpha$, the second term inside the large square brackets of Equation (A. 3-43) is missing. The sum of the two terms inside the square brackets may also be written in the form

$$\frac{\sin 2 \alpha (1 - \sin^2 \theta \sin^2 \phi)}{\cos^2 \alpha \cos^2 \theta - \sin^2 \theta \sin^2 \phi \sin^2 \alpha}$$

For $(1/\tan\alpha) < \tan\theta \cos\phi$ the tapered wedge looks like a cylinder.

A. 3.9 Application of the Tapered Wedge to Wing and Elevator Surfaces

The formulas for the wedge can be obtained by analogy from the formulas for a cylinder. In the present case, however, the contribution to the cross-section comes from the wing on the far side of the fuselage (as viewed from the radar) and the azimuth angle for normal incidence is approximately $\pi - \psi$ rather than ψ . The results are

$$\sigma_{\perp} = \frac{\pi L^2}{(\pi - \alpha)^2} \cos^4 \gamma + \frac{L^2}{4\pi} \left[\tan(\alpha + \theta) + \tan(\alpha - \theta) \right]^2$$

$$\theta = \frac{\pi}{2} + \chi \cos \psi - \theta^*$$

$$\phi_{\perp}^* = \pi - \psi + \delta \cos \theta^* \cos \psi$$

$$\sigma = \beta \sigma_{\perp}$$

$$\phi^* = \phi_{\perp}^* \pm \frac{\sqrt{2} \lambda}{4\pi\sqrt{\beta} L \sin \theta^*} \quad (A. 3-44)$$

Equation (A. 3-44) holds for $|\theta| < \alpha$. For $\begin{cases} \theta > \alpha \\ \theta < -\alpha \end{cases}$ the term $\begin{cases} \tan(\alpha - \theta) \\ \tan(\alpha + \theta) \end{cases}$ is omitted. For $|\theta| > (\pi/2) - \alpha$ these formulas should not be used (the surface then looks like a cylinder).

A. 3.10 Square Corner Reflector

A square corner reflector is made up of three mutually orthogonal squares as shown in Figure A-35. The orientation of the corner is determined by the vectors \hat{e}_1 , \hat{e}_2 , and \hat{e}_3 . Let the vector to the transmitter-receiver be denoted by $\hat{r} = \sin \theta^* \cos \phi^* \hat{i} + \sin \theta^* \sin \phi^* \hat{j} + \cos \theta^* \hat{k}$. Let l , m , n stand for $\hat{e}_1 \cdot \hat{r}$, $\hat{e}_2 \cdot \hat{r}$, and $\hat{e}_3 \cdot \hat{r}$ but rearranged so that $|l| \leq |m| \leq |n|$. There are three types of contributions which the corner reflector makes to the cross-section: flat-plate contributions, dihedral

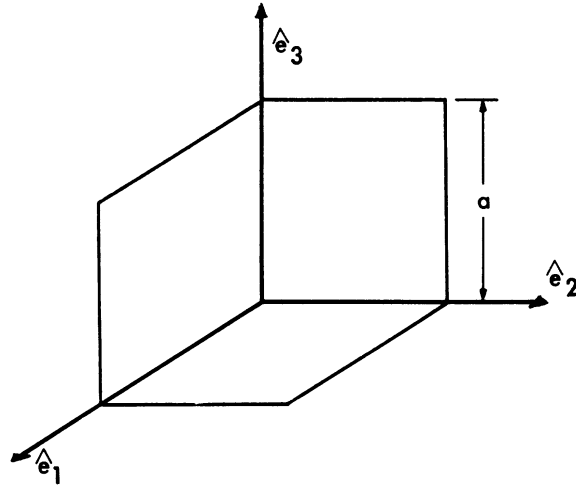


FIG. A-35

contributions, and corner contributions. The flat-plate contributions occur for the direction of incidence nearly normal to one of the faces of the corner (l and m nearly zero), and are given by Equations (A. 3-31) through (A. 3-34).

The dihedral contributions come when the direction of incidence is nearly parallel to one of the faces and is pointed into the dihedral formed by the other two faces (that is, $m > 0$, $n > 0$, $l \sim 0$). For normal incidence ($l = 0$) the cross-section of the dihedral is

$$\sigma_{\perp} = \frac{16\pi}{\lambda^2} m^2 a^4 \left(2 \frac{e_i^2}{\sin^2 \theta^*} - 1 \right)^2 \quad (\text{A. 3-45})$$

where \hat{e}_i is the vector perpendicular to \hat{r} when $l = 0$. The azimuth at which the cross-section is given by Equation (A. 3-45) is

$$\phi_{\perp}^* = -\tan^{-1} \frac{e_{ix}}{e_{iy}} - \sin^{-1} \left(\frac{e_{iy} e_{iz}}{|e_{iy}| \sqrt{1 - e_{iz}^2}} \tan \theta^* \right) \quad (\text{A. 3-46})$$

The azimuths at which the cross-section has been reduced to a fraction β of what it is at normal incidence are given by

$$\phi^* = \phi_{\perp}^* \pm \frac{\lambda}{2 \pi a \sqrt{2 \beta} \sqrt{\sin^2 \theta^* - e_{iz}^2}} \quad (\text{A. 3-47})$$

The corner contributions occur only when looking into the corner (ℓ, m, n all positive). The corner contribution is

$$\sigma = \begin{cases} \frac{64 \pi}{\lambda^2} \frac{\ell^2 m^2 a^4}{n^2} & (m \leq n/2) \\ \frac{4 \pi}{\lambda^2} \ell^2 \left(4 - \frac{n}{m}\right)^2 a^4 & (m \geq n/2) \end{cases} \quad (\text{A. 3-48})$$

A. 3. 11 Equilateral Triangular Corner Reflector

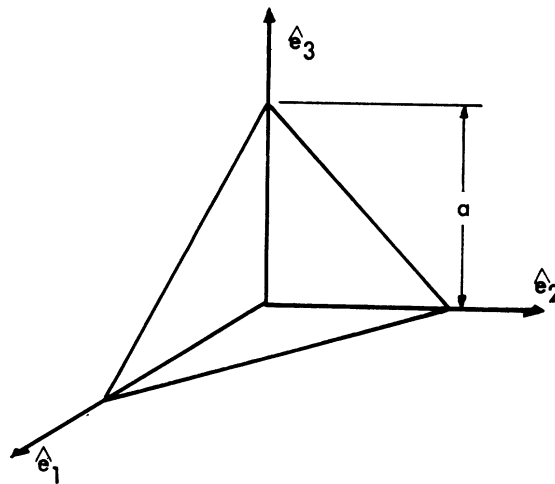


FIG. A-36

In Figure A-36 the notation used is the same as that for the square corner reflector. Equations (A. 3-45) through (A. 3-48) become

$$\sigma_{\perp} = \frac{4\pi}{\lambda^2} m^2 a^4 \left(2 \frac{e^{iz}}{\sin^2 \theta^*} - 1 \right)^2$$

$$\phi_{\perp}^* = -\tan^{-1} \frac{e^{ix}}{e^{iy}} - \sin^{-1} \left(\frac{e^{iy} e^{iz}}{|e^{iy}| \sqrt{1 - e^{iz} \tan \theta^*}} \right)$$

$$\phi^* = \phi_{\perp}^* + \frac{\lambda}{2\pi a \sqrt{\beta} \sqrt{\sin^2 \theta^* - e^{iz}}}$$

$$\sigma = \begin{cases} \frac{64\pi}{\lambda^2} \frac{l^2 m^2 a^4}{(l+m+n)^2} & (l+m \leq n) \\ \frac{4\pi}{\lambda^2} \left(l+m+n - \frac{2}{l+m+n} \right)^2 a^4 & (l+m \geq n) \end{cases}$$

(A. 3-49)

A. 3.12 Circular Corner Reflector

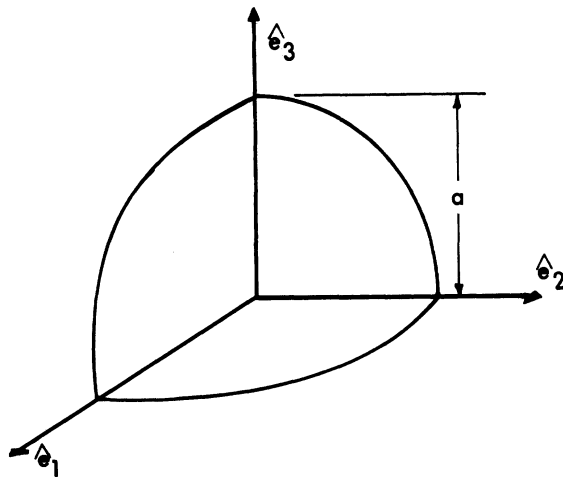


FIG. A-37

For the circular corner reflector (Fig. A-37), the notation is the same as that for the square corner reflector. Equations (A. 3-45) through (A. 3-47) become

$$\begin{aligned}\sigma_{\perp} &= \frac{\pi^3}{\lambda^2} m^2 a^4 \left(2 \frac{e_{iz}^2}{\sin^2 \theta^*} - 1 \right)^2 \\ \phi_{\perp}^* &= -\tan^{-1} \frac{e_{ix}}{e_{iy}} - \sin^{-1} \left(\frac{e_{iy} e_{iz}}{|e_{iy}| \sqrt{1 - e_{iz}^2} \tan \theta^*} \right) \\ \phi^* &= \phi_{\perp}^* \pm \frac{\lambda}{\pi^2 a \sqrt{\beta} \sqrt{\sin^2 \theta^* - e_{iz}^2}} \quad . \quad (A. 3-50)\end{aligned}$$

The formula corresponding to Equation (A. 3-48) is not known except in the special case $l = m = n = 1/\sqrt{3}$ where it is

$$\sigma = \frac{16 \pi a^4}{3 \lambda^2} \left[3 \tan^{-1} \left(\frac{1}{\sqrt{3}} \right) \right]^2 \quad . \quad (A. 3-51)$$

In lieu of the correct formula for other l , m , n , one can either scale up the last line of Equation (A. 3-49) by a factor of 4 or scale down Equation (A. 3-48) by a factor of 4/9.

A. 3.13 Rectangular Corner Reflector

For the rectangular corner reflector (Fig. A-38), only the corner (triple reflection) contributions will be considered here. Let l , m , n stand for $\hat{e}_1 \cdot \hat{r}$, $\hat{e}_2 \cdot \hat{r}$, $\hat{e}_3 \cdot \hat{r}$, and let a , b , c stand for a_1 , a_2 , a_3 with the ordering

$$\left| \frac{l}{a} \right| \leq \left| \frac{m}{b} \right| \leq \left| \frac{n}{c} \right| \quad .$$

The corner contribution is zero unless $l > 0$, $m > 0$, and $n > 0$. When l , m , and n are all positive the corner contribution is

$$\sigma = \begin{cases} \frac{4\pi l^2 b^2}{\lambda^2} \left(4c - \frac{n}{m}b\right)^2 & \left(\frac{m}{b} \geq \frac{n}{2c}\right) \\ \frac{64\pi l^2 m^2 c^4}{\lambda^2 n^2} & \left(\frac{m}{b} \leq \frac{n}{2c}\right) \end{cases} \quad (A.3-52)$$

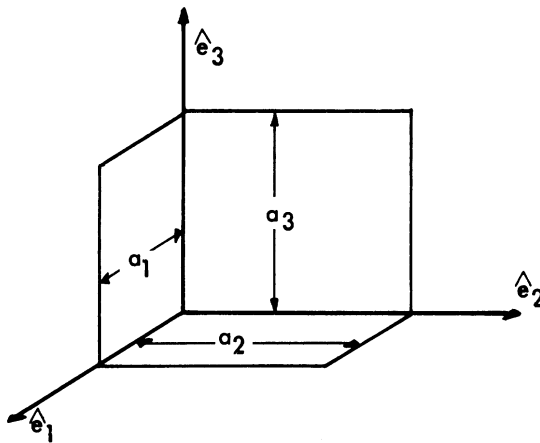


FIG. A-38

A. 3.14 General Triangular Corner Reflector

For triple reflections with the notation as in Section A. 3. 13, the cross-section is

$$\sigma = \begin{cases} \frac{64\pi^2 m^2 c^2}{\left(\frac{l}{a} + \frac{m}{b} + \frac{n}{c}\right)^2 \lambda^2}, & \left(\frac{l}{a} + \frac{m}{b} \leq \frac{n}{c}\right) \\ \frac{4\pi a^2 b^2 c^2}{\lambda^2} \left(\frac{l}{a} + \frac{m}{b} + \frac{n}{c} - 2 \frac{\left(\frac{l}{a}\right)^2 + \left(\frac{m}{b}\right)^2 + \left(\frac{n}{c}\right)^2}{\frac{l}{a} + \frac{m}{b} + \frac{n}{c}} \right), & \left(\frac{l}{a} + \frac{m}{b} \geq \frac{n}{c}\right) \end{cases} \quad (\text{A. 3-53})$$

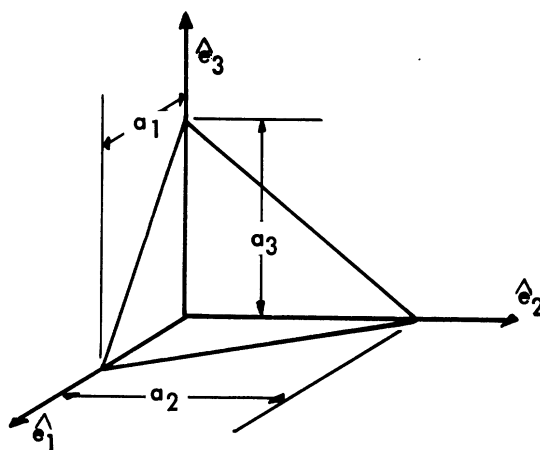


FIG. A-39

A. 3.15 Maximum Reflections From Corner Reflectors

The maximum triple reflection contribution for general rectangular (Fig. A-38), elliptical, and triangular (Fig. A-39) corner reflectors occurs for $\frac{l}{a} = \frac{m}{b} = \frac{n}{c} = \frac{1}{\sqrt{a^2 + b^2 + c^2}}$. The value of the cross-section at the maximum is

$$\sigma_{\max} = \begin{cases} \frac{36\pi a^2 b^2 c^2}{\lambda^2 (a^2 + b^2 + c^2)} & \text{(rectangular)} \\ \frac{16\pi a^2 b^2 c^2 k}{\lambda^2 (a^2 + b^2 + c^2)} & \text{(elliptical)} \\ \frac{4\pi a^2 b^2 c^2}{\lambda^2 (a^2 + b^2 + c^2)} & \text{(triangular)} \end{cases} \quad (\text{A. 3-54})$$

$$k = \left[\frac{3 \tan^2(\theta/2)}{1 + \tan^2(\theta/2)} \right]^2$$

APPENDIX B

REPLACEMENT OF B-47 AND B-52 PARTS BY SIMPLE SHAPES

B.1 INTRODUCTION

When the procedures of Appendix A are applied to specific problems, such as computations of the radar cross-sections of an aircraft, there is considerable arbitrariness in the breakdown of the aircraft into parts and in the choice of simple shapes whose radar cross-sections may be computed approximately to replace these parts.

To allow for this arbitrariness in procedure and consequent uncertainty in the results, the task of computing the cross-section of each aircraft was worked on independently by a few people. Each made his own breakdown of the aircraft into parts and his own choice of simple shapes. For each aircraft, the numerical computations for one breakdown were done by slide-rule and hand computation (Method I). For the alternate breakdown the computations were done primarily on IBM machines and the Michigan Digital Automatic Computer (MIDAC) (Methods II and III).

Sections B.2 and B.3 give the breakdown of the B-47 and the B-52 aircraft into parts and indicate the simple shapes chosen. The appropriate formulas given in Appendix A were applied with allowance for shadowing effects. These effects were computed approximately or only estimated depending on the computational difficulty and the sensitivity of the results to shadowing.

B.2 THE B-47 AIRCRAFT

Three views of the aircraft are shown in Figure B-1, its structural breakdown is shown in Figure B-2, and an example of the breakdown used in Method II is shown in Figure B-3. A summary of the geometry employed is shown in Table B-1.

B.3 THE B-52 AIRCRAFT

The three views of this aircraft are shown in Figure B-4 and an example of the breakdown used in Method II is shown in Figure B-5. A summary of the geometry employed in the three approaches to the computations appears in Table B-2.

UNIVERSITY OF MICHIGAN

2260-1-T

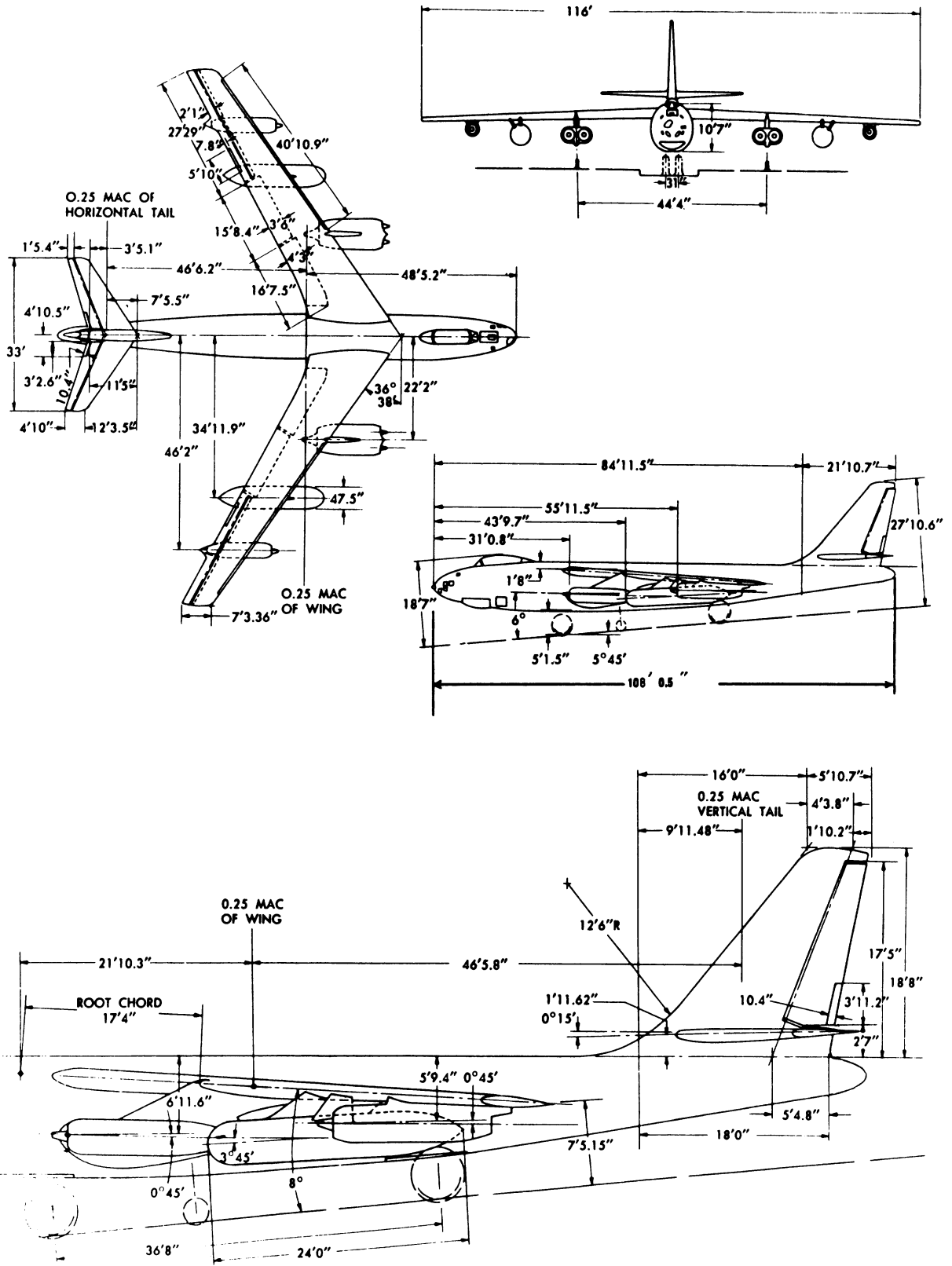


FIG. B-1 THREE VIEWS OF A B-47

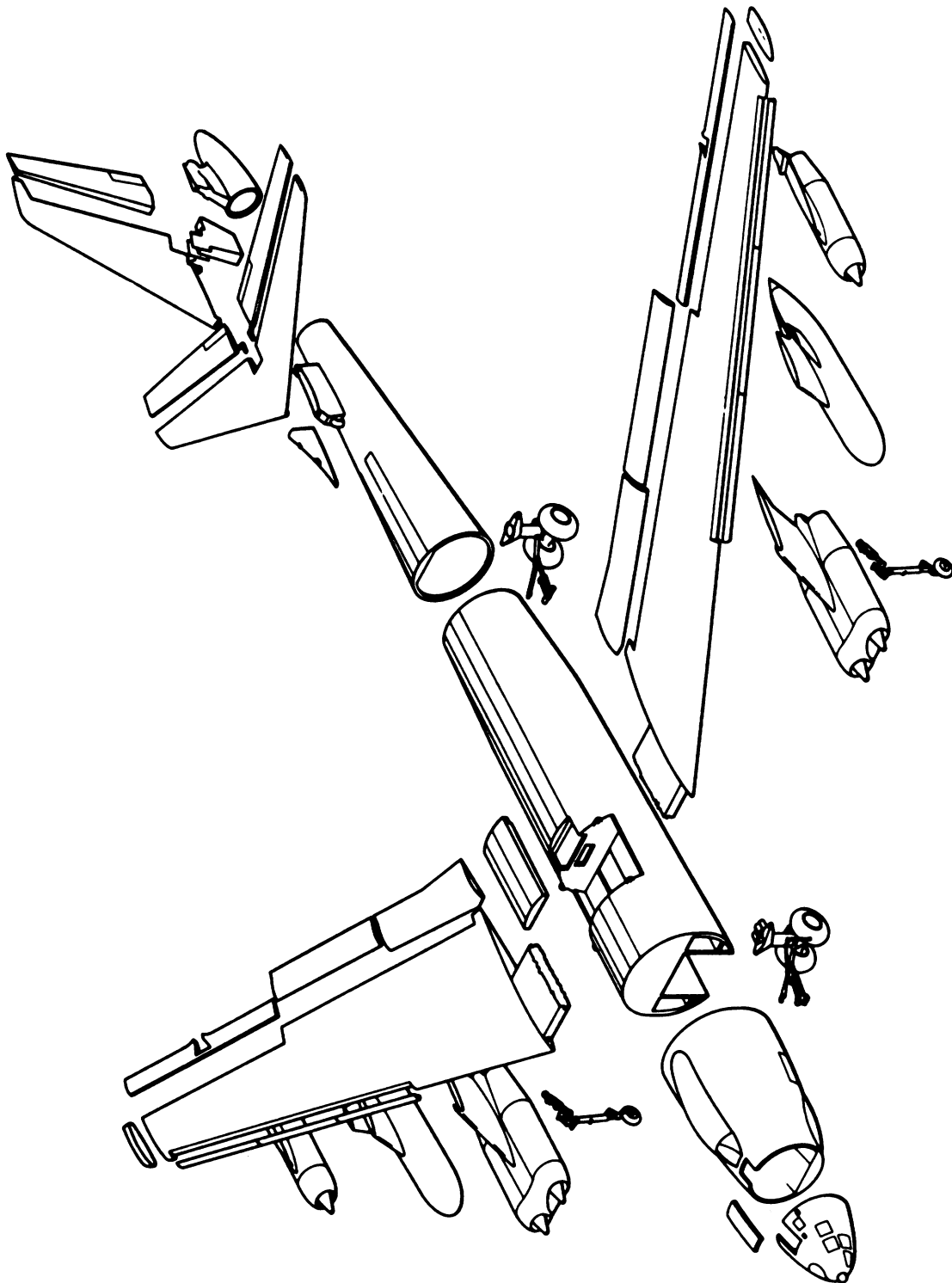


FIG. B - 2 STRUCTURAL BREAKDOWN OF THE B - 47

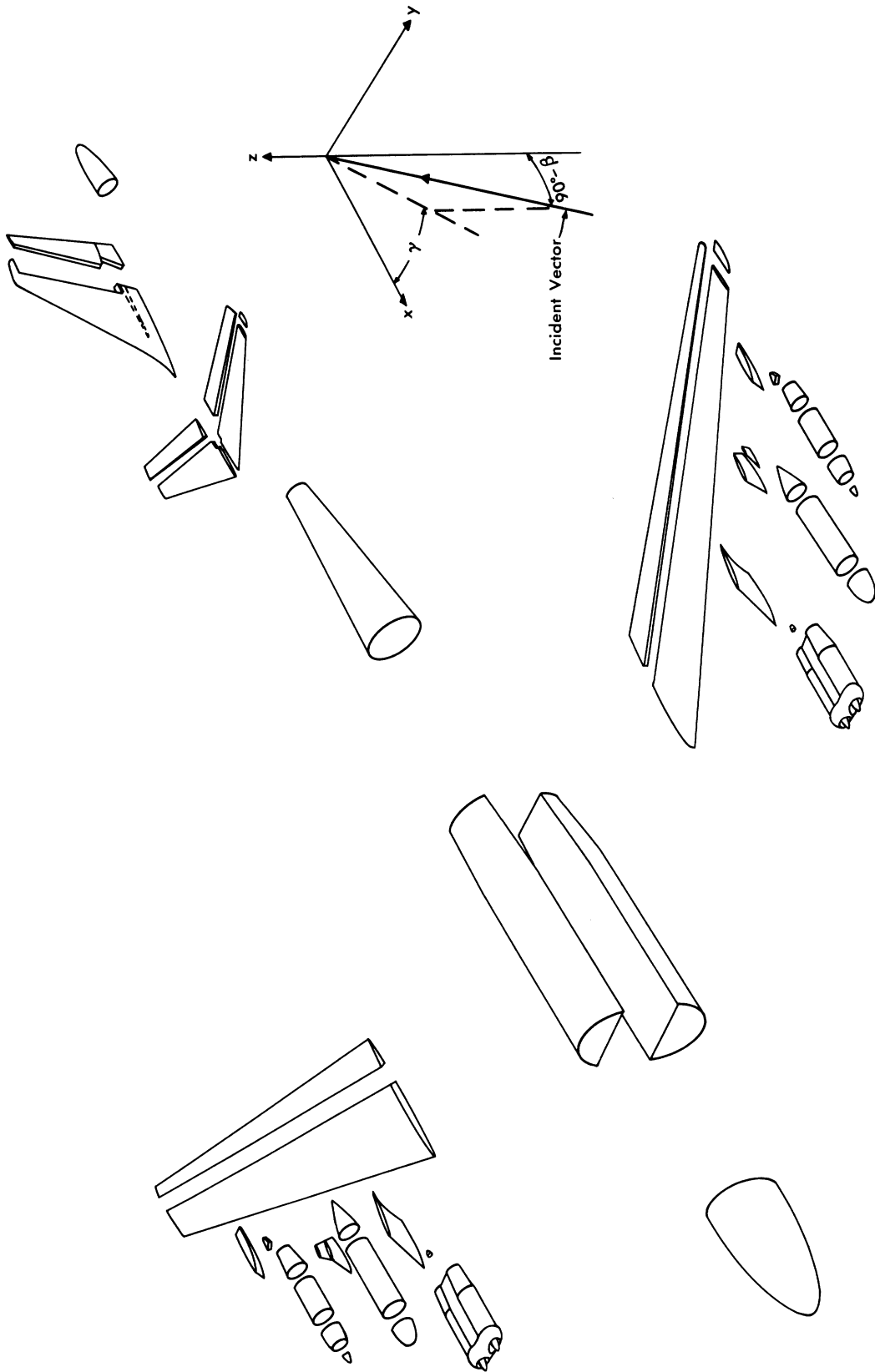


FIG. B - 3 ILLUSTRATIVE EXAMPLE OF THE BREAKDOWN USED FOR THE B - 47

UNIVERSITY OF MICHIGAN

2260-1-T

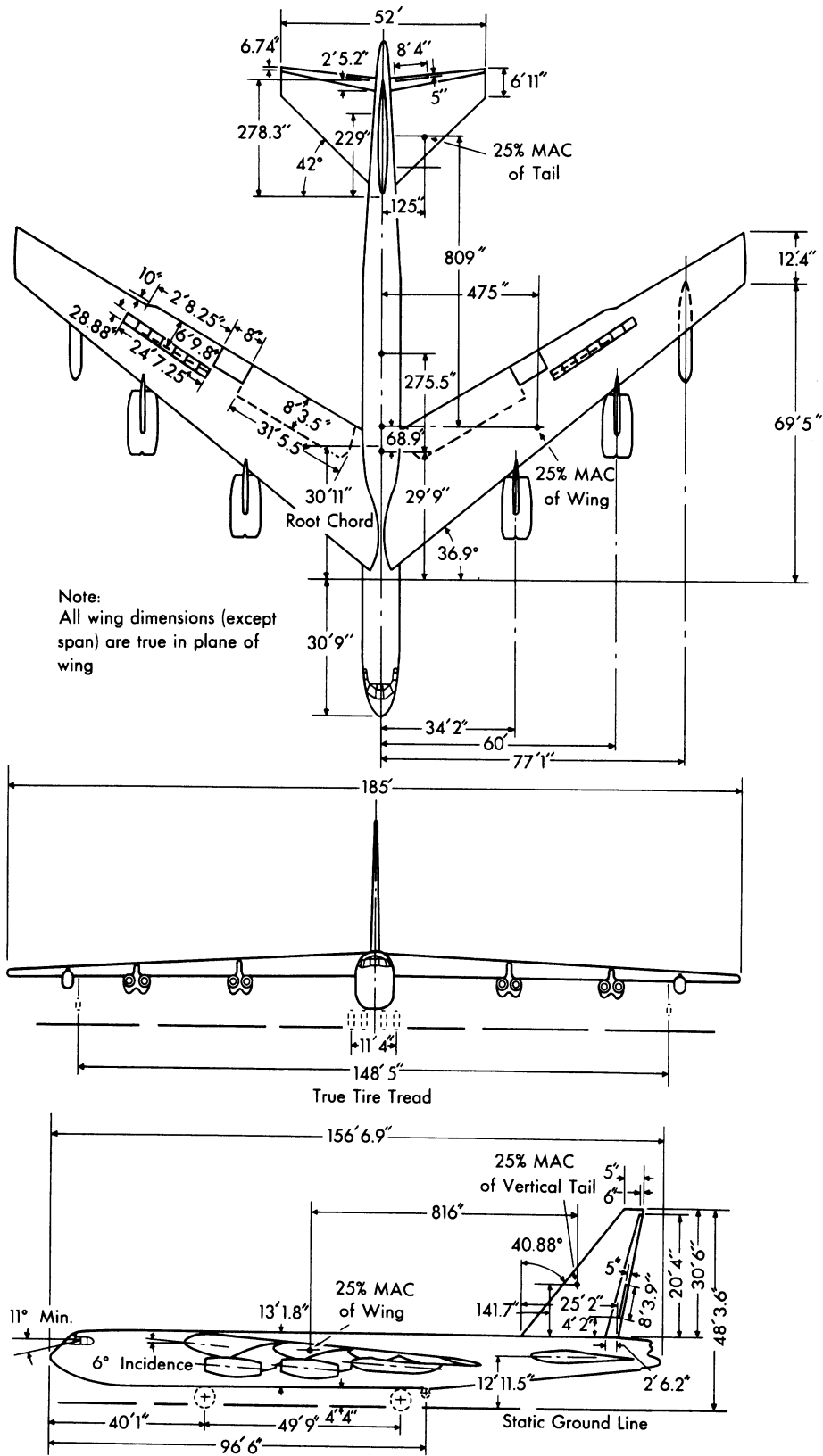


FIG. B-4 THREE VIEWS OF A B-52

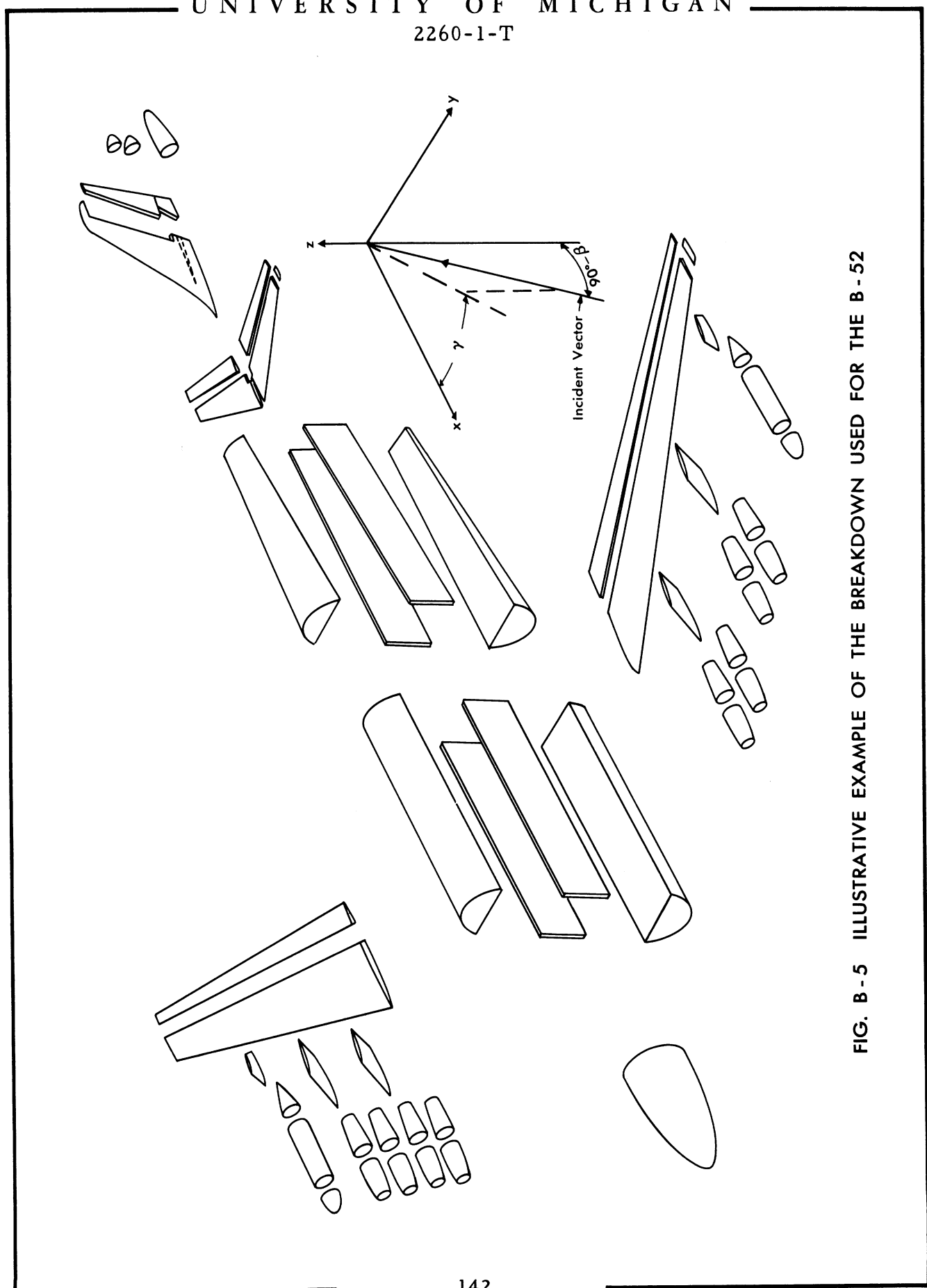


FIG. B-5 ILLUSTRATIVE EXAMPLE OF THE BREAKDOWN USED FOR THE B-52

CONFIDENTIAL

UNIVERSITY OF MICHIGAN

2260-1-T

TABLE B-1
B-47 GEOMETRICAL BREAKDOWN

SECTION OF PLANE	METHOD I	METHOD II
<u>Fuselage</u> nose forward aft portion rear view	prolate spheroid ellipsoid circular cone prolate spheroid	prolate spheroid circular cylinder circular cone prolate spheroid
<u>Wings</u> leading edges trailing edges tips	elliptic cones tapered wedge - - - - -	elliptic cones tapered wedge prolate spheroid
<u>Engines</u> nacelles-front nacelles-center nacelles-rear nose mounts	ogive + wire loop representing edge of front aperture - - - - - ogive - - - - - - - - - -	ogive + wire loop circular cylinder ogive circular cones flat plate
<u>Wing Tanks</u> front side rear	prolate spheroids circular cylinders ogives	prolate spheroids circular cylinders ogives
<u>Tail Section</u> vertical fin rudder stabilizer elevators	elliptic cone tapered wedge elliptic cones tapered wedge	elliptic cone tapered wedge elliptic cones tapered wedge

CONFIDENTIAL

UNIVERSITY OF MICHIGAN

2260-1-T

TABLE B-2

B-52 GEOMETRICAL BREAKDOWN

SECTION OF PLANE	METHOD I	METHOD II	METHOD III
<u>Fuselage</u>			
nose	ellipsoid	ellipsoid	ellipsoid
center	elliptic cylinder	elliptic cylinder	elliptic cylinder
aft	elliptic cone	- - - - -	elliptic cone
aft-upper and lower	- - - - -	half circular cones	- - - - -
aft-middle	- - - - -	flat plates	- - - - -
rear gun turrets	ellipsoids	prolate spheroids	ellipsoids
<u>Wings</u>			
leading edges	elliptic cones	elliptic cones	elliptic cones
trailing edges	tapered wedges	tapered wedges	thin wires
tips	- - - - -	prolate spheroids	ellipsoid
<u>Engines</u>			
nacelles	ogives (+ wire loops)	ogives (+ wire loops)	ogives
mounts	- - - - -	flat plates	flat plates
<u>Wing Tanks</u>			
forward	ellipsoids	ellipsoids	ellipsoids
center	- - - - -	- - - - -	elliptic cylinder
aft	elliptic cones	ogives	ellipsoids
<u>Tail Section</u>			
vertical fin	elliptic cone	elliptic cone	elliptic cone
rudder	tapered wedge	tapered wedge	elliptic cone (with thin wire from rear)
stabilizer	elliptic cone	elliptic cone	elliptic cone
elevator	tapered wedge	tapered wedge	elliptic cone (with thin wire from rear)

The various configurations were all appropriately truncated and shadowed.

~~CONFIDENTIAL~~
CONFIDENTIAL

UNIVERSITY OF MICHIGAN

2260-1-T

REFERENCES: APPENDICES

Number

- A1 J. H. Van Vleck, F. Bloch, and M. Hammermesh, "Theory of Radar Reflection from Wires or Thin Metallic Strips", Journal of Applied Physics, 18, pp. 274-294, 1947.
- A2 J. A. Stratton, Electromagnetic Theory, McGraw-Hill Book Co., 1941.
- A3 UMM-87, "Studies in Radar Cross-Sections III - Scattering by a Cone", by K. M. Siegel and H. A. Alperin, University of Michigan, Willow Run Research Center (1952).
UNCLASSIFIED
- A4 UMM-115, "Studies in Radar Cross-Sections VIII - Theoretical Cross-Sections as a Function of Separation Angle Between Transmitter and Receiver at Small Wavelengths", by K. M. Siegel, H. A. Alperin, R. R. Bonkowski, J. W. Crispin, A. L. Maffett, C. E. Schensted, and I. V. Schensted, University of Michigan, Willow Run Research Center (1953).
UNCLASSIFIED
- A5 W. W. Hansen and L. I. Schiff, "Theoretical Study of Electromagnetic Waves Scattered from Shaped Metal Surfaces", Quarterly Report No. 2, Microwave Laboratory, Stanford University, February 1948.
- A6 UMM-106, "Studies in Radar Cross-Sections VI - Cross-Sections of Corner Reflectors and Other Multiple Scatterers at Microwave Frequencies", by R. R. Bonkowski, C. R. Lubitz, and C. E. Schensted, University of Michigan, Willow Run Research Center (1953). SECRET (UNCLASSIFIED if Appendix is removed)

UNIVERSITY OF MICHIGAN

2260-1-T

DISTRIBUTION LIST
PROJECT 2260 REPORTS

Copy No.

- 1-2 Commander, Wright Air Development Center
ATTN: WCLRE-5, R. Rawhouser
Wright-Patterson Air Force Base, Ohio
- 3-12 Commander, Wright Air Development Center
ATTN: WCSG, Major F. Porter
Wright-Patterson Air Force Base, Ohio
- 13 Commander, Wright Air Development Center
ATTN: WCLRC-1, G. W. Schivley
Wright-Patterson Air Force Base, Ohio
- 14 Commander, Wright Air Development Center
ATTN: WCLGB, A. L. Brothers
Wright-Patterson Air Force Base, Ohio
- 15 Commander, Wright Air Development Center
ATTN: WCOSI
Wright-Patterson Air Force Base, Ohio
- 16 Commander, Wright Air Development Center
ATTN: WCSB, J. S. McCollom
Wright-Patterson Air Force Base, Ohio
- 17 Commander, Wright Air Development Center
ATTN: WCSM, P. R. Doty
Wright-Patterson Air Force Base, Ohio
- 18 Commander, Wright Air Development Center
ATTN: WCSM, J. A. Walker
Wright-Patterson Air Force Base, Ohio
- 19 Commander, Wright Air Development Center
ATTN: WCSM, J. R. Korosei
Wright-Patterson Air Force Base, Ohio

CONFIDENTIAL

UNIVERSITY OF MICHIGAN

2260-1-T

Distribution List, Project 2260 Reports

Copy No.

- 20 Commander, Wright Air Development Center
ATTN: WCSP, E. B. Bell
Wright-Patterson Air Force Base, Ohio
- 21 Commander, Air Materiel Command
ATTN: ATIAE, R. L. James
Wright-Patterson Air Force Base, Ohio
- 22 Commander, Wright Air Development Center
ATTN: WCLRO, Maj. G. J. Akerland
Aircraft Radiation Laboratory
Wright-Patterson Air Force Base, Ohio
- 23 Commander, Wright Air Development Center
ATTN: WCLRD, G. B. Fanning
Wright-Patterson Air Force Base, Ohio
- 24 Director of Research and Development Headquarters, USAF
ATTN: AF-DRD-EL
Washington 25, D. C.
- 25 Commander, Air Research and Development Command
ATTN: RDDDE, Major D. L. Deal
P. O. Box 1395, Baltimore 3, Maryland
- 26 Commander, Rome Air Development Center
ATTN: Research Library, RCRES-4C
Griffiss Air Force Base, Rome, N. Y.
- 27 Commander, Air Force Cambridge Research Center
ATTN: Dr. R. C. Spencer
224 Albany Street, Cambridge 39, Massachusetts
- 28 Commander, Air Force Cambridge Research Center
ATTN: Ralph Hiatt
224 Albany Street, Cambridge 39, Massachusetts
- 29 Commander, Air Force Cambridge Research Center
ATTN: Electronics Research Library
224 Albany Street, Cambridge 39, Massachusetts

UNIVERSITY OF MICHIGAN

2260-1-T

Distribution List, Project 2260 Reports

Copy No.

- 30 Commander, Air Force Cambridge Research Center
ATTN: Dr. F. S. Holt
224 Albany Street, Cambridge 39, Massachusetts
- 31 Commander, Air Force Cambridge Research Center
ATTN: Nelson A. Logan, Antenna Laboratory
224 Albany Street, Cambridge 39, Massachusetts
- 32 Commander, Air Force Cambridge Research Center
ATTN: C. J. Sletten
224 Albany Street, Cambridge 39, Massachusetts
- 33 Commander, Air Force Cambridge Research Center
ATTN: R. Barrett
224 Albany Street, Cambridge 39, Massachusetts
- 34 Commander, Air Force Missile Test Center
ATTN: A. R. Beach
Patrick Air Force Base, Cocoa, Florida
- 35 Commander, Holloman Air Development Center
ATTN: Operation and Project Center
Alamogordo, New Mexico
- 36 Research and Development Board,
Library Branch Information Offices
ATTN: W. N. Plant
RM. E1065, The Pentagon
Washington 25, D. C.
- 37 Chief, Technical Library Office
Office, Asst. Secretary Defense (Research and Development)
Room 3E1065, The Pentagon
Washington 25, D. C.
- 38 Commander, Air Force Armament Center
ATTN: A. J. Wilde
Eglin Air Force Base, Florida

UNIVERSITY OF MICHIGAN

2260-1-T

Distribution List, Project 2260 Reports

Copy No.

- 39 Commander, Air Proving Ground Command
 ATTN: Class. Tech. Data Br. D/01
 Eglin Air Force Base, Florida

- 40 Commander, Strategic Air Command
 ATTN: Operations Analysis Office
 Offutt Air Force Base, Nebraska

- 41 Commander, Headquarters Central Air Defense Force
 P. O. Box 528
 Kansas City, Missouri

- 42 Director, Air University
 Req. CR-3998
 Maxwell Air Force Base, Alabama

- 43 Commander, Rome Air Development Center
 ATTN: Morris Handlesman
 Griffiss Air Force Base
 Rome, N. Y.

- 44 Commander, Rome Air Development Center
 ATTN: Joseph Vogelmann
 Griffiss Air Force Base
 Rome, N. Y.

- 45 Director, Naval Research Laboratories
 ATTN: Martin Katzin, Code 5270
 Washington 25, D. C.

- 46 Director, Naval Research Laboratories
 ATTN: John E. Meade, Code 5340
 Washington 25, D. C.

- 47 Director, Naval Research Laboratories
 ATTN: W. S. Ament
 Washington 25, D. C.

UNIVERSITY OF MICHIGAN

2260-1-T

Distribution List, Project 2260 Reports

Copy No.

- 48 Chief, Bureau of Ships, Department of the Navy
ATTN: Code 816
Washington 25, D. C.
- 49 Chief, Bureau of Aeronautics, Department of the Navy
ATTN: Electronics Division
Washington 25, D. C.
- 50 Bureau of Aeronautics, Central District
ATTN: Electronics Division
Wright-Patterson Air Force Base, Ohio
- 51 Chief, Bureau of Ordnance, Department of the Navy
ATTN: Code AD-3
Washington 25, D. C.
- 52 Chief of Naval Operations, Department of the Navy
ATTN: OP-42-B2
Washington 25, D. C.
- 53 Commanding Officer and Director
U. S. Navy Electronics Laboratory
San Diego, 52, California
- 54 Commander, U. S. Naval Air Development Center
ATTN: Electronics Laboratory
Johnsville, Pennsylvania
- 55 Commander, U. S. Naval Ordnance Laboratory
Silver Spring 19, Maryland
- 56 Commander, U. S. Naval Ordnance Test Station, Inyokern
China Lake, California
- 57 Commander, U. S. Naval Proving Ground
ATTN: Dr. E. K. Ritter
Department OK
Dahlgren, Virginia

UNIVERSITY OF MICHIGAN

2260-1-T

Distribution List, Project 2260 Reports

Copy No.

- 58 Chief Signal Officer, Department of the Army
ATTN: Engineering Technical Division
Washington 25, D. C.
- 59 Department of the Army, Office of Chief of Ordnance
ATTN: ORDTU, Capt. W. O. Fuller
Washington 25, D. C.
- 60 Director, Evans Signal Laboratory
ATTN: James T. Evers, Chief
Radar Development Branch, Belmar, N. J.
- 61 Director, Evans Signal Laboratory, ATTN: I Stokes,
Chief, Radar Branch, Belmar, N. J.
- 62 Director, Evans Signal Laboratory
ATTN: O. C. Woodyard, Belmar, N. J.
- 63 Commander, Signal Engineering Laboratory
ATTN: Sig-EL-RDR, Fort Monmouth, N. J.
- 64 Director, Evans Signal Laboratory
ATTN: R. Wagner, Belmar, N. J.
- 65 Document Room, Project Lincoln
Massachusetts Institute of Technology
ATTN: Ethel R. Brans
P. O. Box 390, Cambridge 39, Massachusetts
- 66 Dr. Dan Dustin, Massachusetts Institute of Technology
Lincoln Laboratory, P. O. Box 73
Lexington 73, Massachusetts
- 67 I. Shapiro, Massachusetts Institute of Technology
Lincoln Laboratory, P. O. Box 73
Lexington 73, Massachusetts

UNIVERSITY OF MICHIGAN

2260-1-T

Distribution List, Project 2260 Reports

Copy No.

- 68 Dr. J. T. DeBettincourt, Massachusetts Institute of Technology
Lincoln Laboratory, P. O. Box 73
Lexington 73, Massachusetts
- 69 Ohio State University Research Foundation
ATTN: Dr. R. Fouty
310 Administration Building, Ohio State University
Columbus 10, Ohio
- 70 Radiation, Inc.
ATTN: J. B. Duryee
Melbourne, Florida
- 71 The University of Texas, Electrical Engineering Research
Laboratory, ATTN: Dr. A. W. Straiton
Box 8026, University Station
Austin 12, Texas
- 72 Franklin Institute Laboratories, 20th St. Benjamin Franklin
Parkway, ATTN: Dr. S. Charp
Philadelphia 3, Pennsylvania
- 73 Boeing Airplane Company
ATTN: R. H. Jewett
Seattle 14, Washington
- 74 D. Adcock, Research and Development Laboratories
Hughes Aircraft Company
Culver City, California
- 75 Dr. L. L. Bailin, Research and Development Laboratories
Hughes Aircraft Company
Culver City, California
- 76 Dr. N. Begovich, Research and Development Laboratories
Hughes Aircraft Company
Culver City, California

UNIVERSITY OF MICHIGAN

2260-1-T

Distribution List, Project 2260 Reports

Copy No.

- 77 R. S. Wehmer, Research and Development Laboratories
Hughes Aircraft Company
Culver City, California
- 78 Dr. John L. Hult, Rand Corporation
1500 4th Street, Santa Monica, California
- 79 Dr. Sidney Bertram, Electronics Division
Rand Corporation
1500 4th Street, Santa Monica, California
- 80 Dr. M. J. Ehrlich, Microwave Radiation Co., Inc.
3312 Pacific Avenue, Venice, California
- 81 Dr. R. D. O'Neal, Convair
Ft. Worth 1, Texas
- 82 Prof. F. V. Schultz, University of Tennessee
Knoxville 16, Tennessee
- 83 Prof. Samuel Silver, Electrical Engineering Department
University of California, Berkeley 4, California
- 84 D. Slager, Department 75
Bendix Radio, Towson, Maryland
- 85 B. D. Steinberg, Project Engineer
Philco Radio Corporation, Philadelphia 34, Pennsylvania
- 86 Dr. V. Twersky, Electronics Defense Laboratory
P. O. Box 205, Mountain View, California
- 87 Dr. Allen B. Currie, Bell Telephone Laboratory
Whippany, N. J.
- 88 Dr. S. Ramo, Ramo-Wooldridge Corporation
8820 Bellanca Ave., Los Angeles 45, California
- 89 ^{A. D. Whealon,}
~~Dr. B. Wieland,~~ Ramo-Wooldridge Corporation
8820 Bellanca Ave., Los Angeles 45, California

UNIVERSITY OF MICHIGAN
2260-1-T

Distribution List, Project 2260 Reports

Copy No.

- 90 Dr. Robert A. Wolf, Cornell Aero Research Laboratory
Buffalo, N. Y.
- 91 Georgia Institute of Technology
State Engineering Experimental Station
Atlanta, Georgia
- 92 Standard Rolling Mills, Inc.
ATTN: Vincent Lane
196 Diamond Street, Brooklyn 22, N. Y.
- 93 The Johns Hopkins University, Radiation Laboratory
ATTN: Dr. D. D. King
1315 St. Paul Street, Baltimore, Maryland
- 94 The Johns Hopkins University, Radiation Laboratory
ATTN: E. M. Glaser
1315 St. Paul Street, Baltimore, Maryland
- 95 Massachusetts Institute of Technology
Research Laboratory of Electronics
ATTN: Dr. L. J. Chu
Cambridge, Massachusetts
- 96 Lockheed Missile System Division, Dept. 74-32
7701 Woodley Ave., Van Nuys, California
- 97 J. R. Giantvalley, Ryan Aeronautical Company
Lindbergh Field, San Diego 12, California
- 98 Orison Wade, Engineering Department
Convair, San Diego, California
- 99 G. R. Lindsay, Operational Research Group
Defense Research Board, Ottawa, Ontario, Canada
- 100 Prof. G. A. Woonton, Eaton Electronics Laboratory
McGill University, Montreal, Quebec, Canada
- 101 Dr. L. S. Scheingold, Sylvania Engineering Laboratories
70 Forsyth Street, Boston, Massachusetts